Dynamics of Intracellular Nano-Transport by Kinesins

by

Woochul Nam

A dissertation submitted in partial fulfillment
of the requirements for the degree of
Doctor of Philosophy
(Mechanical Engineering)
in The University of Michigan
2015

Doctoral Committee:

Professor Bogdan I. Epureanu, Chair
Research Associate Professor Oliver D. Kripfgans
Assistant Professor Allen P. Liu
Professor Noel C. Perkins

To my family

ACKNOWLEDGEMENTS

First, I wish to express my utmost gratitude to my advisors and chair of my doctoral committee, Professor Bogdan I. Epureanu, for his inspiring and encouraging guidance during the past years. I also want to thank Professor Oliver D. Kripfgans, Professor Allen P. Liu, and Noel C. Perkins for their valuable comments and suggestions, and serving on my doctoral committee. I sincerely admit that it may not be possible to attain without their supervision and supports.

I am also grateful to my colleagues of Applied Nonlinear Dynamics of Multi-Scale Systems Laboratory, including Akira Saito, Andrew Madden, Darren Holland, Joosup Lim, Chulwoo Jung, Kiran D'Souza, Andrew Sloboda, Anish Joshi, Jason Rodgers, Sungkwon Hong, Kiyoung Oh, Seunghoon Baek, Eleni Gourgou, Ehsan Mizakhalili, Amin Ghadami, Jauching Lu, Mainak Mitra, Weihan Tang, and Olguta Marinescu, for their insights and suggestions. It has been a very nice time and a good memory for me.

I am thankful for the financial support over the course of my PhD studies. The Mechanical Engineering Department at University of Michigan provided me with a First Year Department Fellowship. I have also received support from NSF grants CMMI-0800202 and Predoctoral Fellowship provided by Rackham Graduate School at University of Michigan.

I would like to express my appreciation for my entire family, in particular my parents and in-laws for their love and supports. I am also thankful to my son Ian for being so adorable and healthy. Finally, I appreciate my lovely wife, Yanghwa, for marrying me and for her unwavering support. Her encouragement enabled me to complete this work.

TABLE OF CONTENTS

LIST OF FIGURES

Figure

LIST OF TABLES

Table

LIST OF APPENDICES

Appendix

ABSTRACT

Dynamics of Intracellular Nano-Transport by Kinesins Woochul Nam Chair: Bogdan I. Epureanu Transport in neurons is realized by motor proteins (kinesins) which walk along intracellular tracks. In this dissertation, a new physics-based mathematical model of kinesin is developed to capture the long range transport. Healthy mechanical transport is necessary for neurons to maintain their normal functions. Degradation of this transport is believed to result in neurodegenerative diseases such as Alzheimer's disease. One possible cause for the degradation is the presence of molecules bound on the intracellular tracks which can interfere with the motion of kinesin. Hence, a qualitative and quantitative study about the effects of obstacles on the intracellular transport is performed using the new model.

To address the limitations of previous models which are established from *in vitro* experiments, the newly developed model considers various motions of kinesins in cells; walking on the track, unbinding from the track, thermally fluctuating motion (when they are not bound on the track), and binding again to the track. The effects of viscoelasticity of the fluid where the transport takes place are incorporated into the model with the generalized Langevin equation to consider the effect of polymers in intracellular fluids. The collective transport (where several kinesins transport a cargo together) is considered with the new model also. The characteristics of this collective transport are captured with the metrics proposed in this study. Also, the binding of obstacles such as tau proteins on the track are considered by using the chemical kinetics between tau proteins and the tracks. The

interference between kinesins and tau proteins is quantified by comparing the model predictions with the experimental results.

The effects of obstacles on the transport are investigated with Monte Carlo simulations. Kinesins unbind from the track when they encounter clusters of tau proteins. However, kinesins can bind to other locations of the track in a very short time, especially the kinesins which are attached to small cargoes. Due to this behavior, the decrease in the average velocity is not considerable until the tracks are crowded with large numbers of obstacles. Despite the small change in the average velocity, kinesin motion is modified by the obstacles. The transport of the cargo is delayed in front (upstream) of clusters of tau proteins, and the transport is likely to be fast behind (downstream) the clusters.

This change in the kinesin motion caused by obstacles can be exploited in several ways. First, it is difficult to detect the number of tracks and the amount of tau clusters on a track in the cell. However, the condition of the track can be estimated by observing the behavior of kinesins using fluorescently labeled cargoes; Second, the dependency of the regional delays on the concentration of tau proteins is much stronger than the change in the average velocity due to the presence of obstacles. For example, when the velocity decreases by 5 $\%$ in the presence of 2 μM tau proteins, the regional delays increase 2.8 fold. Finally, observing the regional delays requires only a relatively low precision (i.e., 1 μm) which is much longer than the step size of kinesins (8 nm). Therefore, the predicted behavior of kinesins near obstacles and the proposed method to characterize that behavior open the door to an easier means to estimate the state of health of the transport system in neuron.

CHAPTER I

Introduction

Cells need various intracellular movements to perform their tasks. In the presence of spatial concentration gradients, diffusion can be used to transport particles. However, if processes in cells demand relatively large forces or motions with high velocity, more powerful methods are required. To satisfy these demands, cells use molecular motors which use energy generated in cellular organelle such as mitochondria. Molecular motors have important roles in various processes such as muscle contraction, cell division, intracellular transport, operation of flagella and cilia, and DNA metabolism [3–6]. The cytoskeletal motors (e.g., kinesin and dynein) move along microtubules (MTs) to transport various vesicles, organelles and cytoskeletal polymers [7–9] toward the cell membrane or nucleus. Transport along MTs is essential for cells to sustain their normal function, especially in the brain. In a neuron, cytoskeletal motors transport various cargoes to and from synapses via MTs in axons. Thus, neural functions are abnormal if the axonal transport system deficient.

This dissertation focuses on transport by kinesin-1 (referred to simply as kinesin) among the superfamily of kinesin [8–10]. The structure of kinesin is shown in [11, 12]. Kinesins have two identical heads which are 7 nm long, and they are connected to individual neck linkers (NLs) which are composed of 14-amino acids (AAs) [11, 12]. The length

of the NLs is about 3 nm, and they are coiled together at the neck [13, 14]. The cargo linker has one end connected to the neck, and has a long alpha helical coiled-coil structure with a length of about 100 nm. The other end of the cargo linker has a domain which binds to cargoes. Kinesins walk with their two heads in a hand over hand fashion [15, 16]. The step size is about 16 nm. Thus, their cargoes proceed 8 nm per step [16–21]. At every step, chemical energy obtained from the hydrolysis of one adenosin triphosphate (ATP) molecule is used [17, 22, 23]. Due to advances in motility assays, laser trapping systems, and optical technology, the motion of a single molecule can be observed experimentally *in vitro* [16, 18, 24–27]. The maximum velocity of this molecular motor is approximately 800 nm/s, and the velocity varies with the external load and ATP concentration [25,27–29]. Single kinesins stall when the resisting load is about 7 pN [25, 28, 29]. The run length of kinesins (which is the walking distance of kinesins before they detach from the MT) is about 1 μm [25, 30]. It is observed that the run length decreases as the loads increase [25].

Several models have been proposed to predict the transport performed by kinesins. The walking motion of a kinesin molecule was described by considering the mechanochemical cycle of kinesins [31–40]. To calculate the period of the kinesin step, these models assume that the mechanochemical cycle consists of several states. Then, the effect of the load on the transition between these states is taken into account to capture the effect of the load on the walking velocity. Also, the detachment of kinesins from the MTs and its dependency on the load were considered by using measured run lengths [25, 37, 38]. In these models, the increase in the probability of detachment from the MT was considered using the Boltzmann's relation which can predict the changes in this probability as a function of the energy generated by the force [41]. Klumpp et al. [42] derived equations for the velocity and run length of kinesins which considers detachment and attachment of kinesins to the MTs as well as the walking motion. However, their equations are only applicable when

the interference between kinesins is negligible. The effects of the interaction between kinesins were modeled with the mean-field method when the volume of the kinesin traffic is considerable [43–45]. Despite their abilities to predict the spatial distribution of kinesins, existing models over simplify the physics of the motion of kinesin near other kinesins. In addition, the transport by kinesins was observed to be abnormal when neurons generate excessive tau proteins [46, 46–50], and previous models are not able to capture the effects of tau proteins on the intracellular transport.

Thus, the goal of this dissertation is to develop a model which is able to capture the complex intracellular transport by considering several factors. Each of these factors are described in a chapter, as follows:

- The transient dynamics of kinesins has to be captured when they are walking on the track because the force acting on kinesins continuously varies over time (Chapter II).

- The effect of high viscoelasticity of cellular fluid on the motion of the cargo needs to be considered because changes in the motion of the cargo affects the mechanochemical cycle of kinesins (Chapter III).

- The binding and unbinding of kinesins to MTs has to be considered to predict the collective transport performed by several kinesins (Chapter IV).

- New stochastic metrics are required to characterize the dynamics of collective transport realized by coupled kinesins (Chapter V).

- The interference between kinesins or between a kinesin and other motor proteins can be important when a large number of motor proteins share the same MT. Experimental observations have shown that kinesins tend to walk along the axial direction

of MTs in the absence of obstacles. A model for the motion along the tangential direction is required to study the ability of kinesins to bypass obstacles, other kinesins or other motor proteins (Chapter VI).

- The effects of tau proteins bound on the MTs on the motion of kinesin have to be investigated. A model which can capture the stochastic binding of tau proteins on the outer surface of MTs is needed also (Chapter VII).

New characteristics of the transport are predicted by using the new model. More specifically, in chapter II, the new mechanistic model for walking motion of kinesins is introduced. The fundamental idea on the effect of the force on the chemical reaction and the kinesin structure of the model are based on the previous mechanistic model proposed in our group [40, 51]. In addition to the previous model, chemical kinetics is improved to capture the instant of transitions between mechanochemical states of kinesins. This augmentation is necessary to calculate the unbinding probability of kinesin from the track because the unbinding probabilities are different at each state. Also, the stochastic backward steps are included in the new model because kinesins have frequent backward steps for considerable resisting loads larger than 5 pN [27, 29]. Then, the new parameter values are obtained to consider the effect of backward steps on the average walking velocity of kinesins.

In chapter III, the effects of fluids on kinesins are considered. In vitro motion of cargoes moved by kinesins is different from the observed intracellular transport [52, 53]. Although several biological hypotheses have been proposed to explain this difference [54], their respective models are not fully verified. The effect of cellular fluid can be an explanation for the different motions. The viscoelasticity of the cellular fluid is considerably higher compared to the fluids used for *in vitro* experiments because various polymers and

proteins are present inside the cellular fluid. The kinesin and its cargo have to navigate through complex structures formed by these particles. To study that motion, a large cargo (i.e., radius of 1 μm) is used. The effects of the complex structures are captured by a modified model of viscoelasticity of the cytoplasm. Because kinesins are very small compared to the large cargo, the effect of the fluid on the walking motion of kinesin itself (i.e., diffusion of its heads) can be assumed to be negligible. The effects of highly viscous fluids on the transport by a single kinesin are predicted. Also, the effect of viscoelasticity of the fluid is considered by using subdiffusion. The generalized Langevin equation on fractional Brownian motion is incorporated into the model also.

In chapter IV, the binding and unbinding of kinesin to a MT are captured to predict the collective transport by several kinesins. While a single kinesin molecule is able to walk about 1 μm along a MT in the absence of external loads [25, 30, 55, 56], kinesins perform much longer range transport in cells [7–9]. The binding and unbinding of kinesins to MTs are important mechanisms involved in this long transport. The unbinding probabilities corresponding to each mechanochemical state of kinesin are considered. The statistical characterization of the instants and locations of binding are captured by computing the probability of unbound kinesin being at given locations. It is predicted that the number of kinesins attached on the cargo changes the velocity and run length of the cargo (which is the distance of cargoes before all kinesins of the cargoes detach from the MT). In addition, the studies on the effect of force on the unbinding probabilities of each state of kinesins reveal that the kinesins behave at times like anchors (i.e., almost do not move but remain bound on the MT) when large resisting forces act on them.

In chapter V, metrics developed in this thesis to characterize the coordinated transport of several kinesins are introduced. Since the chemical reactions fueling molecular motors are stochastic processes, the movements of coupled kinesins are not perfectly syn-

chronized. Thus, the method used in a previous study [51] is modified to measure the level of (stochastic) synchronization of coupled kinesins. To predict the difference in the work each kinesin performs, the forces acting on each kinesin are compared. If a kinesin molecule is very close to the cargo, the cargo linker which connects the kinesin and the cargo becomes slack. Then, the kinesin is not able to support any load from the cargo. Thus, the probability that the cargo linker becomes slack is also obtained. These metrics can be extended to characterize collective work done by other proteins such as dyneins which walk along MT.

In chapter VI, the two dimensional motion of kinesins (along axial and tangential directions of MTs) is studied to predict the transport when obstacles are located on the MTs. Most previous studies consider the motion of kinesin when almost every binding site is accessible. However, this assumption is not applicable to intracellular transport by kinesins because other molecular motors or other types of proteins can also attach to binding sites of MTs [43, 50, 57–61]. The motion of a kinesin head is realized by a conformational change in the structure of the kinesin molecule and by the diffusion of the head [40, 62–65]. A novel model is developed to account for the diffusion of the kinesin head in the absence of obstacles prior to examining the effects of obstacles. To determine the direction of the next step a kinesin takes when encountering an obstacle, this model considers the extension in the NLs [66] and the dynamic behavior of the coiled-coil structure of the neck [67]. It is revealed that the unfolding of the neck and the binding of the head with tilted posture are required to obtain probabilities of side walk of kinesin comparable to those measured in previous experiments [68]. Then, the interactions between kinesins and several molecular motors (i.e., static motors, motors walking to the plus-end of MTs, and motors walking to the minus-end of MTs) are characterized by using the model.

In chapter VII, the degradation of transport by tau proteins is investigated. If neurons

generate excessive tau proteins, these proteins are clustered on the surface of MTs [58, 69]. These clusters of tau can disturb the motion of the motor proteins. A new model is developed to characterize the effect of tau proteins and density of MTs in the axons on the transport performed by kinesins. Several types of motions of kinesins and their cargoes (i.e., walking on the MTs, unbinding from the MTs, Brownian motion in the axon, binding to the MTs) are considered because the cargoes transported by single kinesins have been observed to have these various motions when transported along axons or dendrites [45]. Also, the binding of tau proteins on the MT surface and the formation of tau clusters are considered by assuming that the affinity between free tau proteins in the fluid and a binding site of a MT depends on the number of tau molecules which are already bound at that site. Then, transport velocities are obtained for various densities of MTs and concentrations of tau. Also, new metrics are developed to characterize the regional delay (or traffic jam) near tau clusters (predicted from the model).

CHAPTER II

Mechanistic model of kinesin

2.1 Summary

In this chapter, a mechanistic model for the walking motion of kinesin is introduced. The model considers the chemical reaction and the mechanical dynamics together with the chemical cycle. The effects of force on the chemical reaction and on the backward steps are also incorporated into the model. Then, the values of model parameters which enable the model to predict the experimentally measured velocity are obtained.

2.2 Mechnochemical cycle of kinesin

A kinesin molecule is assumed to be composed of two heads, two NLs, and one neck. Each head is connected to the neck by a NL, and the cargo is linked to the neck via a cargo linker as shown in Fig. 2.1. Kinesin walks toward the plus-end of a MT by a repeated mechanochemical cycle, as depicted in Fig. 2.2.

2.3 Dynamics of kinesin and its cargo

Kinesins are considered with rigid or elastic components. Heads and necks of kinesins and their cargo are assumed to be rigid spheres. NLs are assumed to be a linearly elastic element. The cargo linkers are also assumed to have tether behavior. They resist tensile

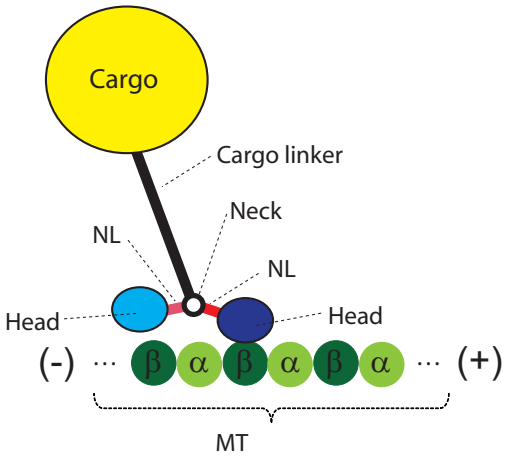

Figure 2.1: Kinesin and MT. The MT is composed of two tubulins (i.e., α and β tubulins). The heads of kinesin only bind to β tubulin. The plus and minus signs denote the polarity of the MT.

forces, but do not carry compressive loads. Thus, the dynamics is not linear. The forces between the neck and the cargo are determined by three cases of interaction between the cargo and the kinesin molecule. Fig. 2.3 shows those cases.

When one or more kinesins transport a cargo, the force F_c acting on the cargo is obtained by adding every force $F_{\text{kin},i}$ generated by each kinesin i and the external load F_L as

$$F_c = -F_L + \sum_{i=1}^{N} F_{\text{kin},i}. \tag{2.1}$$

The sign of F_L is plus when it is toward the minus-end of the MT. F_L is expressed with minus because the positive direction is considered toward the minus-end of MT. Since the Reynolds number regarding the motion of the cargo is very small, the position of the cargo x_c can be determined using Stokes' law as

$$x_c(t) = x_c(0) + \frac{1}{6\pi r_c \eta} \int_0^t F_c(\tau) d\tau. \tag{2.2}$$

where r_c is the radius of the cargo, and η denotes the viscosity of the fluid. Note that this

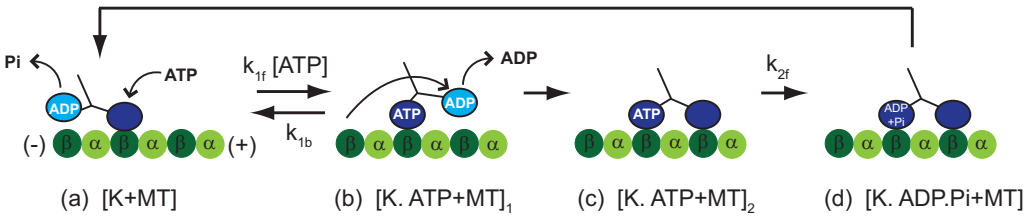

Figure 2.2: The mechanochemical cycle of kinesin. (a), (b) ATP binding to the leading head results in a conformational change in the molecule. The trailing head moves to the next binding site by relaxing the stresses caused by the conformational change and by Brownian motion. (b), (c) The free head strongly binds to the new binding site by dissociating adenosine diphosphate (ADP). (d) ATP is hydrolyzed into ADP and phosphate. Then, the trailing head become weakly bound after releasing phosphate. The cycle repeats starting with (a).

equation is only valid for a kinesin moving in purely viscous fluids. Thus it is modified to describe the transport in viscoelastic fluids in Section 2.2.

Because the cargo linker is a long and slender coiled-coil structure, the ability of the cargo linker to support forces is assumed to be negligible when its two end points are close to each other. Thus, forces are not transferred through the cargo linker when the distance between the cargo and the neck is smaller than 100 nm. Note that this is the distance between the ends of the cargo linker. The same distance, measured along the MT is smaller due to geometric effects (2 or 3 dimension). The value of the distance between the end points along the MT where loads start to be transferred is smaller than 100 nm and is denoted by L_c. When the radius of the cargo is 50 nm, the value of L_c can be calculated as 94 nm using the geometric relation suggested by Fehr et al. [26]. Thus, the force transferred to the neck of the i^{th} kinesin via its cargo linker is obtained as

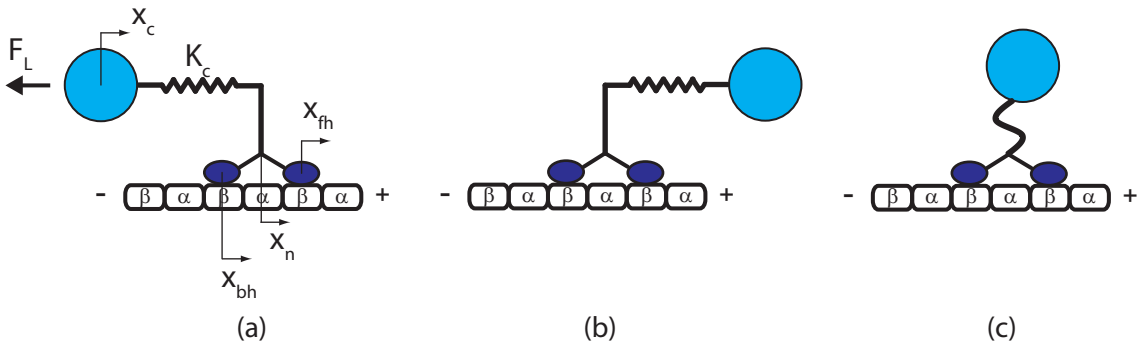

Figure 2.3: Interactions between the cargo and a kinesin. (a) The kinesin pulls the cargo. (b) The cargo pulls the kinesin. (c) The cargo linker is slack.

$$F_{\text{kin},i} = \begin{cases} K_c(x_{n,i} - x_c - L_c) & \text{if } x_{n,i} \geq x_c + L_c, \\ K_c(x_{n,i} - x_c + L_c) & \text{if } x_{n,i} \leq x_c - L_c, \\ 0 & \text{otherwise}, \end{cases} \tag{2.3}$$

where K_c is the stiffness of the cargo linker. $x_{n,i}$ is the position of the neck of the i^{th} kinesin.

While a kinesin head waits for ATP to bind, it is assumed that the whole force on the neck is transferred to the forward head and the other head does not have any load. Experiments support this assumption [70, 71]. After the diffusion of the free head to the next binding site, both heads are strongly bound to the MT. Thus, the force on the neck is transferred through both NLs. The force transferred by the NLs to the neck is calculated

as

$$F_{n,i} = \begin{cases} K_n(x_{\mathrm{fh},i} - x_{n,i}) \\ \quad \text{if the kinesin is in state } [\mathrm{K} + \mathrm{MT}], \\ \\ 2K_n\left(\frac{x_{\mathrm{fh},i}+x_{\mathrm{bh},i}}{2} - x_{n,i}\right) \\ \quad \text{if the kinesin is in state } [\mathrm{K.ATP} + \mathrm{MT}]_2, \end{cases} \tag{2.4}$$

where K_n is the stiffness of a NL. $x_{\mathrm{fh},i}$ and $x_{\mathrm{bh},i}$ are the positions of the forward and backward head. Both $F_{\mathrm{kin},i}$ and $F_{n,i}$ are applied at the neck. The size of the neck is assumed negligible. Thus, these two forces have to balance. The positions of the cargo and the necks of all kinesins are obtained at every time step as the values which satisfy this force equilibrium as well as Eqs. Eq. (2.1) and Eq. (2.2).

2.4 Chemical reaction of kinesin

Each head experiences the attachment of ATP and its hydrolysis at every step. This chemical reaction is described by a Michaelis-Menten kinetics as

$$E + S(K + \mathrm{ATP}) \underset{k_{1b}}{\overset{k_{1f}}{\rightleftharpoons}} E \cdot S(K \cdot \mathrm{ATP}) \overset{k_{2f}}{\to} E + P(K + \mathrm{ADP} + \mathrm{Pi}), \tag{2.5}$$

where E, S, P and K denote enzyme, substrate, product, and kinesin, respectively. This chemical kinetics determines the instants when steps of kinesins take place.

The transition rate regarding the dissociation of an ATP molecule from the forward head is assumed to depend on the stresses on the kinesin head as

$$k_{1b} = k_{1b,0} \exp \frac{\frac{1}{2}\kappa(\frac{F_{\mathrm{kin}}}{\kappa} - \Phi_c)^2}{k_B T}, \tag{2.6}$$

where Φ_c and κ are constants of the model. This equation captures the fact that the rate constant k_{1b} is minimum ($k_{1b} = k_{1b,0}$) when the protein is in equilibrium (i.e., when $F_{\mathrm{kin}} = \kappa\Phi_c$).

The motion of kinesin involves two time scales. The time needed for one cycle of the chemical process to complete is referred to as the dwell time. The diffusion time is the required time for a head which just become free to step to the next binding site by Brownian motion and by relaxing the stresses due to the conformational change. This diffusion time is much shorter than the dwell time *in vitro* [27]. For a higher viscous fluid, the diffusion time increases, but the increase is not large enough to make the diffusion time comparable to the dwell time. Since the size of a kinesin neck and that of a head are very small compared to polymers and other particles in a cell, it is plausible to assume that the diffusion time is very short even in highly viscous environments (e.g., *in vivo*). Furthermore, the cargo also experiences increased drag forces in fluids with increased viscosity. That causes the chemical reaction to slow down. For nano-size particles, the viscosity that the particles experience increases exponentially over their sizes [72, 73]. As the cargo is larger than the kinesin heads and neck, the effect of the high viscosity on the chemical reaction is stronger than its effect on the diffusion time. The supplementary material of Gennerich and Schild [74] provides further evidence of this assumption using the experimental data of Kural et al. [52]. Thus, we can assume that diffusion occurs approximately instantaneously.

The dwell time is calculated by using the rate of chemical reaction or by capturing the transition between chemical states of kinesin.

2.4.1 Average rate of chemical reaction

By using single molecule Michaelis-Menten equations [75], the average rate of these two reactions can be calculated as

$$\frac{d\rho}{dt} = \pm \frac{2k_{2f}[\mathrm{ATP}]}{K_M + [\mathrm{ATP}]}, \tag{2.7}$$

where $K_M = \frac{k_{1b}+k_{2f}}{k_{1f}}$. The variable ρ is a state variable whose time rate of change captures the average velocity of the chemical process.The value of ρ becomes 1 (or -1) when the chemical reaction is complete. Then, ρ starts to decrease (or increase) to reach -1 (or 1). The values of 1 and -1 are not physical but just reference values to capture the instants when a cycle of the chemical reaction completes. A more detailed explanation is given in [40].

2.4.2 Stochastic rate of chemical reaction

To capture the stochastically changing dwell time of kinesin, the probability distribution of the dwell time can be calculated as

$$f(t) = \frac{k_{1f}k_{2f}[\mathrm{ATP}]}{2A}[e^{(A+B)t} - e^{(B-A)t}], \tag{2.8}$$

where $A = \sqrt{(k_{1f}[ATP] + k_{1b} + k_{2f})^2/4 - k_{1f}k_{2f}[\mathrm{ATP}]}$ and $B = -(k_{1f}[\mathrm{ATP}] + k_{1b} + k_{2f})/2$. The cumulative distribution is then obtained by integrating Eq. (2.8) to obtain

$$c(t) = \frac{k_{1f}k_{2f}[\mathrm{ATP}]}{2A} \times \Big[\frac{e^{(A+B)t}}{A+B} - \frac{e^{(B-A)t}}{B-A} - \frac{2A}{A^2-B^2}\Big]. \tag{2.9}$$

The instantaneous chemical reaction rate is determined by the function $c(t)$ and a uniformly distributed random variable, w. Our stochastic model requires one random variable for each step of the kinesin. One can obtain the instantaneous dwell time, T_c, by satisfying the following relation,

$$c(T_c) = w_j, \tag{2.10}$$

where j is the index for the step. When the load is constant, the dwell time of each step can simply be calculated from Eq. (2.10). In the collective transport, however, $c(t)$ keeps changing due to the varying load on each kinesin. The chemical state variable ρ enables the capture of this varying chemical rate. Using the instantaneous dwell time obtained

from Eq. (2.10), the instantaneous rate of the chemical state variable is calculated for every time step as

$$\frac{d\rho}{dt} = \pm\frac{2}{T_c}. \tag{2.11}$$

The factor of 2 is included because ρ varies between -1 and 1.

2.4.3 Stochastic state transition

Kinesins are assumed to have four different states per step as shown in Fig. 2.2. Because the interaction of kinesin molecule and the binding sites of MTs are different for each state of kinesin, the unbinding probabilities depend on the current state of the kinesin. Thus, the current state of the kinesin has to be determined before calculating the unbinding probability. The probabilities of states (i.e., [K+MT], $[\mathrm{K.ATP} + \mathrm{MT}]_1$, $[\mathrm{K.ATP} + \mathrm{MT}]_2$, and $[\mathrm{K.ADP.Pi} + \mathrm{MT}]$) are determined by the transition rates. Probabilities satisfy

$$\begin{aligned}
&\frac{d}{dt}P_{[\mathrm{K+MT}]} = -k_{1f}[\mathrm{ATP}]P_{[\mathrm{K+MT}]} + k_{1b}P_{[\mathrm{K.ATP+MT}]_1} \\
&\frac{d}{dt}P_{[\mathrm{K.ATP+MT}]_1} = k_{1f}[\mathrm{ATP}]P_{[\mathrm{K+MT}]} - k_{1b}P_{[\mathrm{K.ATP+MT}]_1} - k_{2f}P_{[\mathrm{K.ATP+MT}]_2}, \\
&\frac{d}{dt}P_{[\mathrm{K.ADP.Pi+MT}]} = k_{2f}P_{[\mathrm{K.ATP+MT}]_2}, \\
&P_{[\mathrm{K.ATP+MT}]_1} = P_{[\mathrm{K.ATP+MT}]_2}
\end{aligned} \tag{2.12}$$

where $P_{[\mathrm{K+MT}]}$, $P_{[\mathrm{K.ATP+MT}]_1}$, $P_{[\mathrm{K.ATP+MT}]_2}$ and $P_{[\mathrm{K.ADP.Pi+MT}]}$ denote the probabilities of chemical states of kinesin shown in Fig. 2.2. Parameters k_{1f}, k_{1b}, and k_{2f} are the transition rates between the states shown in Fig. 2.2 and Eq. (2.5). If the i^{th} cycle starts at t_i, the probability of the current state during the cycle is obtained by solving Eq. (2.12) with the initial conditions $P_{[\mathrm{K+MT}]}(t_i) = 1$, and $P_{[\mathrm{K.ATP+MT}]_1}(t_i) = P_{[\mathrm{K.ATP+MT}]_2}(t_i) = P_{[\mathrm{K.ADP.Pi+MT}]}(t_i) = 0$. Fig. 2.4 shows the probabilities of the bound states over time. The two curves in Fig. 2.4 (b) show the two probabilities, $P_{[\mathrm{K+MT}]}(t)$ and $P_{[\mathrm{K+MT}]}(t) + P_{[\mathrm{K.ATP+MT}]_2}(t)$.

To determine the instants of transitions, a uniformly distributed random number (r_0) between 0 and 1 is generated. When $P_{[\mathrm{K+MT}]}$ becomes r_0, the transition from [K+MT] to $[\mathrm{K.ATP} + \mathrm{MT}]_1$ occurs. Then, the next transition from $[\mathrm{K.ATP} + \mathrm{MT}]_2$ to $[\mathrm{K.ADP.Pi} + \mathrm{MT}]$ occurs when $\mathrm{P}_{[\mathrm{K+MT}]} + \mathrm{P}_{[\mathrm{K.ATP+MT}]_2}$ reaches r_0.

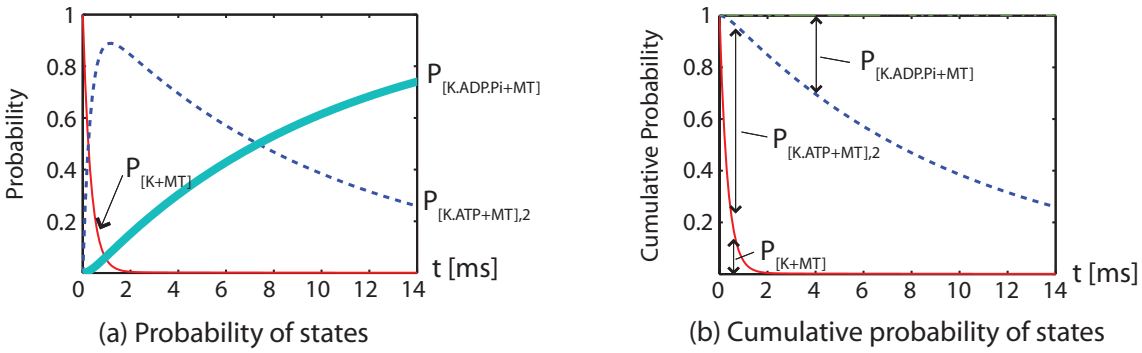

Figure 2.4: Probability of chemical states. (a) shows the changes of the states of kinesin over time in the absence of a load. The thin solid line is the probability of the state [K+MT], and the dotted line and the thick line denote the probability of the states $[\mathrm{K.ATP} + \mathrm{MT}]_2$ and $[\mathrm{K.ADP.Pi} + \mathrm{MT}]$. (b) shows the cumulative probabilities. They are used to determine the instant of the transition between states.

2.4.4 Backward step

If a large load acts on the cargo, kinesins walk toward the minus-end of the MT as well as toward the plus-end [27, 29]. For example, the backward probability is about 5% and 27% for resisting loads of 4 pN and 6 pN, respectively. The cycle of the backward motion is shown in Fig. 2.5. Both the forward and the backward motion are also captured in our model. The model parameters are obtained using experimental results obtained by Carter et al. [27]. They observed that the probability of backward steps increases exponentially with the external load.

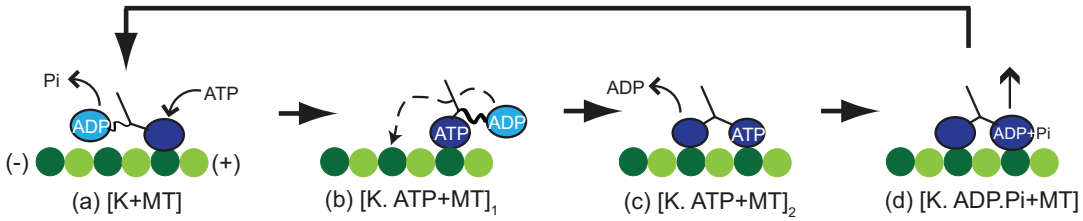

Figure 2.5: Backward step cycle is depicted. ATP binds to the leading head (a); next, the trailing head moves forward due to the conformational change (b); due to the large resisting load acting on the cargo linker, the free head diffuses back to its original site; then, the head attaches to the MT by releasing ADP (c), and ATP is hydrolyzed in the other head (d).

To model this process we use the following algorithm. When the ATP is bound to the head of a kinesin, the probability of backward steps corresponding to the force on the kinesin is calculated. Then, a uniformly distributed random number between 0 and 1 is generated. If the random number is larger than the probability of a backward step, then the free head of the kinesin diffuses to the forward binding site. Otherwise, the free head moves to the binding site behind the fixed head.

2.5 Parameter

Experimentally obtained *in vitro* steady state force-velocity curves [28] are used to determine $k_{1f}, k_{1b,0}, k_{2f}, \kappa$ and Φ_c. Tab. 2.5 shows the values of the parameters of the mechanistic model. The fit is achieved by the nonlinear least-squares fit toolbox in MATLAB. Note that the rate constants of the model in the absence of external loads are similar to the values obtained in the experiment of ATPase [76]. K_c is defined as the experimentally obtained value [77]. In this chapter, the NL is assumed to behave like a linear spring. Thus, the value of K_n is determined so that the linear spring has the same strain energy with the energy of the worm like chain model in [66].

Table 2.1: The values of parameters of the mechanistic model.

Parameter	Value	Unit
K_c	0.3	$\mathrm{pN/nm}$
K_n	3.8	$\mathrm{pN/nm}$
k_{1f}	2.385	$\mu\mathrm{M}^{-1}\mathrm{s}^{-1}$
$k_{1b,0}$	32.921	s^{-1}
k_{2f}	98.875	s^{-1}
Φ_c	1.2114	nm
κ	3.302	$\mathrm{pN/nm}$

Fig. 2.6 shows that the model is able to predict the velocity of kinesin very well by using the obtained parameters.

2.6 Conclusions

The model presented in this chapter is used to perform the studies discussed in the following chapters. Especially, the effects of force on the chemical reaction shown in Eq. (2.6) are used to consider the effects of viscoelasticity of the fluid where the transport takes place on the kinesin motion (in chapter III), and to predict collective transport (in chapters IV and V) where the forces acting on individual kinesins fluctuate over time because of the stochastic motion of kinesins. Also, the method of calculating the probability of each state shown in Eq. (2.12) is necessary to obtain the unbinding probability of kinesins from the MTs (in chapter IV) because the unbinding probabilities are different over the various states of kinesins. Both the effects of force on the chemical reaction and on the

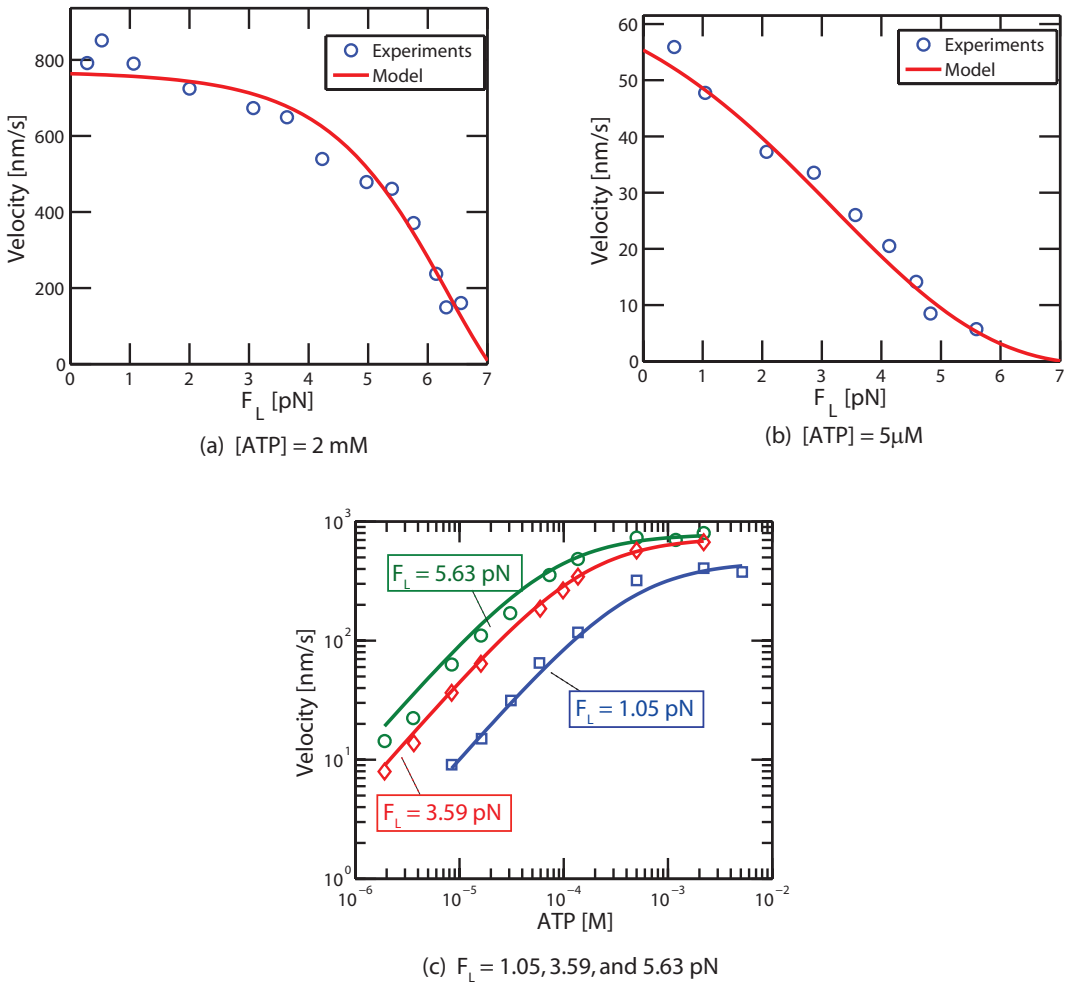

Figure 2.6: Experimentally observed velocity and velocity predicted from the model

unbinding probability are also used to predict the motion of kinesin in the presence of obstacles (in chapters VI and VII).

CHAPTER III

The effects of viscoelastic fluid on kinesin transport

3.1 Summary

In this chapter, the mechanistic model developed in chapter II is used to consider the effect of viscoelasticity of the cellular fluid on the kinesin-medicated transport. This viscoelasticity is caused by the polymers which exist in the fluid. Their interaction with the cargo is considered by modifying the generalized Langevin equation and incorporating it into the mechanistic model.

3.2 Background and motivation

The intracellular fluid is different from fluids used for *in vitro* experiments. It is much more viscous than water and also has elasticity. The large complex modulus of fluid is expected to be a significant factor affecting the motion of kinesin. Holzwarth et al. [78] calculated the required force for kinesin to pull a cargo in the cytoplasm. With the complex modulus data of a COS7 cell, they concluded that a very strong force (~ 75 pN) is needed to transport a bead of radius 0.1 μm. However, their results are based on the assumption that the motion of kinesin *in vivo* is the same as the motion *in vitro*. In addition, their method applies only to steady state motion. The velocity of kinesin in cellular fluids and in artificial viscoelastic fluids is observed by [79–81]. They also estimated the velocity

in cellular fluid by using the force-velocity curve of kinesin *in vitro* and the viscoelastic properties that correspond to a very low frequency motion. Their calculation showed a good match between numerical and experimental results. However, the frequency of kinesin stepping is about 100 Hz, which is much higher than the frequency they used. Also, their method is sensitive to the selection of the value chosen for the low frequency. Therefore, the goal of this chapter is to develop a model which is capable of describing both transient and steady state motions. The model also considers the viscoelasticity of fluid so that the effects of viscosity and elasticity on kinesin can be revealed. The transient dynamics is particularly important in a highly viscoelastic fluid because kinesin requires a relatively long time before reaching its equilibrium configuration (i.e. 8 nm advance of a cargo takes much longer than the time in low viscous fluid). Thus, previous models which do not consider the transient motion are insufficient for modeling the motion of kinesin in a viscoelastic fluid.

Theoretical studies provide models for the dynamics of a sphere moving in a viscoelastic fluid [82–86]. One of the fundamental assumptions of these studies is that the fluid behaves as if it contains small, linearly elastic spheres which account for the elasticity of the fluid. This assumption is feasible if the sphere of interest is very large compared to other particles in the fluid or the particles have spherical shapes. However, the size of a motor protein and its cargo is comparable to other particles in the cytoplasm and cells have particles whose shapes are not like a sphere. Furthermore, particles present *in vivo* are not purely elastic. They have viscosity as well as elasticity. Thus, their models cannot be simply extended to the motion of kinesin in a viscoelastic fluid. Hence, newly developed analysis tools from microrheology have to be used for this study. Subdiffusion, generalized Langevin equation (GLE), generalized Stokes Einstein relation (GSE), and fractional Brownian motion (FBM) are some of the main concepts which can be used to

better understand the effect of viscoelastic fluid on the motion of kinesin [87–91].

The GLE is used with some modifications in this work to predict the motion of a spherical cargo in the cytoplasm. This equation is an improved version of the Langevin equation which governs the motion of a particle in a purely viscous fluid (used for *in vitro* models). Thermal fluctuations of a cargo in a purely viscous fluid have a white noise distribution (normal diffusion) because there is no temporal correlation in the fluctuations. Thus, the resulting mean square displacement (MSD) of the cargo is proportional to t (time). However, the cytoplasm exhibits subdiffusion where the MSD due to thermal fluctuations is proportional to t^{α}, where α is a constant ($0 < \alpha < 1$). This MSD results in a complex modulus which has fractional slopes over frequency on a log scale [92]. In contrast, a system composed of linear elastic and viscous elements has integer slopes. This indicates that subdiffusion cannot be accurately modeled as a system composed of linear springs and dashpots. Therefore, the motion of a particle in cellular fluid has to be described using the GLE. Note that subdiffusion results from temporal correlations in thermal fluctuations. This means that the system dynamics depends not only on current states but also on past states. The GLE accounts for this behavior by using a convolution term of velocities and a memory function.

To study kinesin in a viscoelastic fluid, it is necessary to start by first measuring the complex modulus of the fluid. Since the properties of a fluid are measured by interactions between the particles in the fluid and a measurement probe, the size of the probe is an important parameter. The size of kinesin cargoes is of the order of 1 $\mu\mathrm{m}$, so microrheology has to be employed. In microrheology, there are two ways of measuring the complex modulus of a fluid [93]. The active method is to apply forces to a probe particle from the outside of the system by using an optical trap or a magnetic tweezer. The passive method uses thermal fluctuations as excitation mechanism. In this method, a particle that

already exists in the fluid is used as a probe to minimize the intervention into the original system. The MSD of the probe particle is observed over time using video tracking or laser tracking systems. The GSE provides a method to calculate the complex modulus from the measured MSD by using the GLE. The Fourier transform of the GLE establishes the relation between the complex modulus and the MSD in the frequency domain. Finally, the experimental MSD data is transformed to the frequency domain and substituted into the GLE [94]. This method is limited by the distance the particle is allowed to travel. In a highly dense fluid, the area in which a particle can travel by thermal fluctuations is very small compared to its size. It is also possible that the particle becomes trapped in networks of long polymers and cannot escape without external forces. It is reported that the MSD of a particle in a viscoelastic fluid flattens after a long time [89, 94–96]. This observation supports the idea that the particle becomes trapped by polymers. Thus, the features of a motion of a particle that travels over a long distance in a fluid cannot be found passively. Nevertheless, this passive method is used frequently because it is less invasive compared to the active method where the external force can have effects not only on the probe particle but also on other particles in the fluid.

Generally, the complex modulus of a viscoelastic fluid over frequency can correspond to a power law behavior, and the power can vary over the frequency of excitation. In this chapter, however, the complex modulus corresponding to a power law with a constant power is considered. For example, water mixed with 2 $\mathrm{mg/ml}$ of xanthan follows such a power law [79]. This assumption is reasonable for some cellular fluids also. For example, the cytoplasms of PC12 and NT2 cells have complex modulus whose powers are approximately constant over a wide range of frequencies [80, 97]. To simplify the memory function in the GLE, the complex modulus is assumed to have a single constant fraction number in this chapter. This assumption leads to a FBM which comes from a sin-

gle fractional Gaussian noise [87]. The FBM provides a simple memory function which is proportional to $t^{-\alpha}$ (where α characterizes the ratio between viscosity and elasticity). A fluid characterized by a small α has higher elasticity and lower viscosity than a fluid characterized by a large α.

Two stochastic factors are inherent in the motion of kinesin. One comes from the thermal fluctuations, and the other is related to the chemical reaction between ATP and the motor heads. The model used here is deterministic and provides predictions for the mean behavior of kinesin for both transient and steady state motions. A deterministic model is used because it has significantly higher computational efficiency than any other stochastic computational model.

3.3 Viscoelastic model

3.3.1 Approximate FBM

Viscoelastic effects in a subdiffusional environment are implemented using the FBM. Due to the small size of the kinesin molecule, direct effects of the fluid on it can be neglected. However, the viscoelastic effects on the cargo are important. They are described with the GLE. One obtains

$$m_c \frac{dv_c(t)}{dt} = -\zeta \int_0^t v_c(\tau) H(t-\tau) d\tau + F_{th}(t) + F(t), \tag{3.1}$$

where $H(t)$ is the memory function, $F_{th}(t)$ is the force caused by thermal fluctuations, ζ is a constant which represents the intensity of the viscoelastic forces, and m_c and v_c are the mass and velocity of the cargo. For a purely viscous fluid, ζ is the damping coefficient (and has a value of $6\pi r\eta$ for a sphere of radius r moving in the fluid).

$F_{th}(t)$ is related to the memory function by $< F_{th}(t)F_{th}(t') >= k_B T\zeta H(t-t'),$ where $< \cdot >$ represents the mean over time. This force is not included in our deterministic model because its mean value is zero.

The objective of the model is to predict the motion of the cargo when the force is given. However, the original GLE in Eq. (3.1) has an implicit form for the velocity. To solve this problem, the original GLE is converted into an explicit form for the displacement. Also, inertia is neglected because the Reynolds number of the cargo is very small ($10^{-6} - 10^{-3}$) when the size of the cargo is about $1\mu\mathrm{m}$. Thus, its inertia is very small compared to other forces. The thermal fluctuations of the cargo induced by collisions with other particles in the fluid are very fast compared to the time scale of the walking of kinesin. Thus, most of the thermal forces are assumed to cancel out rapidly, and their effects on the kinesin molecule are considered negligible. With these assumptions, one obtains

$$x_c(t) = x_c(0) + \frac{1}{\zeta}\int_0^t D(t-\tau)F_c(\tau)d\tau, \tag{3.2}$$

where $D(t) = \mathcal{L}^{-\infty}\left[\frac{\infty}{\int\mathcal{L}\{\mathcal{H}(\sqcup)\}}\right]$, with $\mathcal{L}$ and $\mathcal{L}^{-\infty}$ representing the Laplace transform and inverse Laplace transform, respectively.

Experiments on certain neuron cells have revealed that the complex modulus of the intracellular fluid approximately follows a FBM with a single fractional number $\alpha \approx 0.8$ (where α characterizes the ratio between viscosity and elasticity) [80]. Substituting in Eq. (3.2) the expression for the memory function of FBM with a single α, one obtains

$$x_c(t) = x_c(0) + \frac{1}{\zeta}\frac{1}{\Gamma(\alpha)\Gamma(3-\alpha)}\int_0^t M(t-\tau)F_c(\tau)d\tau, \tag{3.3}$$

where $M(\tau) = |\tau|^{\alpha-1}$ is the memory function of this modified GLE, and Γ is the gamma function [87]. Note that ζ is related to the magnitude of complex modulus of a viscoelastic fluid (see Eqs. 3.7 and 3.8).

The current position and force on the cargo can be calculated using Eqs. 2.1–2.4 and 3.3. Then, the numerical convolution in Eq. (3.3) is performed with the following techniques.

First, the different methods are used to calculate the integration from 0 to $t-\varepsilon$ and the integration from $t-\varepsilon$ to t. The trapezoidal rule is used to obtain the integration from 0 to $t-\varepsilon$. To avoid the integration around the singular point at $\tau = t$, the integration between $t-\varepsilon$ and t is changed to another simple form as

$$\begin{aligned}
&\int_{t-\varepsilon}^{t} M(t-\tau)F_c(\tau)d\tau = \int_{t-\varepsilon}^{t} (t-\tau)^{\alpha-1}F_c(\tau)d\tau \simeq \\
&\int_{t-\varepsilon}^{t} (t-\tau)^{\alpha-1}\Big[F_c(t) + \frac{F_c(t)-F_c(t-\varepsilon)}{\varepsilon}(\tau-t)\Big]d\tau = \\
&F_c(t)\frac{1}{\alpha}\varepsilon^{\alpha} + \frac{F_c(t)-F_c(t-\varepsilon)}{\varepsilon}\frac{1}{\alpha+1}(-\varepsilon^{\alpha+1}).
\end{aligned} \tag{3.4}$$

The complex summation can be used to calculate the integration near $\tau = t$. However, Eq. (3.4) is used because it reduces the calculation time, and this conversion is consistent with the trapezoidal integration which assumes that F_c changes linearly between two time steps.

Second, the convolution term in Eq. (3.3) has to be computed at every time step, and that increases the calculation time significantly. To address this issue, we developed a new method which approximates the memory function. Specifically, the rate of change of the memory function is proportional to $(t-\tau)^{\alpha-2}$, and this value is small in the region where τ is not close to t. So, the memory function can be assumed to be piece-wise linear in that region (Fig. 3.1). Then, the calculation of the convolution integral can be simplified as follows

$$\begin{aligned}
&\int_{0}^{t} M(t-\tau)F_c(\tau)d\tau = \int_{0}^{t} (t-\tau)^{\alpha-1}F_c(\tau)d\tau \approx \\
&\Big[\int_{0}^{u_1} (a_1\tau+b_1)F_c(\tau)d\tau + \int_{u_1}^{u_2} (a_2\tau+b_2)F_c(\tau)d\tau + ... \\
&+ \int_{u_{N-1}}^{u_N} (a_N\tau+b_N)F_c(\tau)d\tau\Big] + \int_{u_N}^{t} (t-\tau)^{\alpha-1}F_c(\tau)d\tau = \\
&\sum_{i=0}^{i=N}\Big[a_i\big(U(u_{i+1})-U(u_i)\big) + b_i\big(V(u_{i+1})-V(u_i)\big)\Big] + \int_{u_N}^{t} (t-\tau)^{\alpha-1}F_c(\tau)d\tau,
\end{aligned} \tag{3.5}$$

where u_i are time instances between 0 and t, while a_i and b_i are slopes and y-intercepts of each line, as shown in Fig. 3.1. The functions $U(u_i)$ and $V(u_i)$ are defined as $\int_0^{u_i} \tau F_c(\tau)d\tau$ and $\int_0^{u_i} F_c(\tau)d\tau$.

While all past data is needed to compute the convolution term at the current instant, the simplified computation of Eq. (3.5) requires discrete data only at few time instances u_i and the calculation of a single integral (only from u_N to t instead of one from 0 to t).

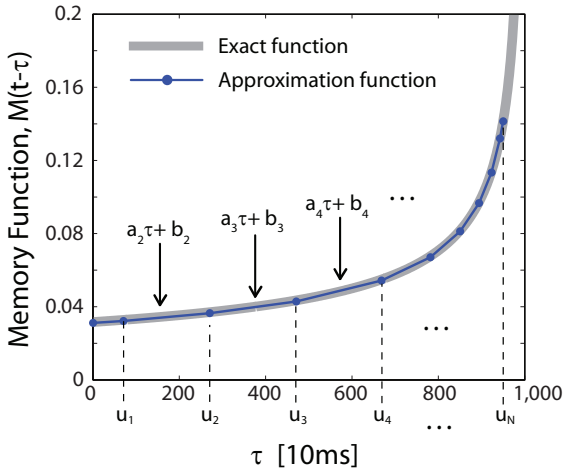

Figure 3.1: Approximation of the memory function, $M(t-\tau)$. The memory function for α =0.5 and t =1,000 [$\times$10 ms] is shown. $a_i\tau + b_i$ indicates the equation for the i^{th} linear approximation.

Finally, the position of cargo is calculated by substituting Eqs. 3.4 and 3.5 into Eq. (3.3). One obtains

$$x_c(t) = x_c(0) + \frac{1}{\zeta}\frac{1}{\Gamma(\alpha)\Gamma(3-\alpha)}\Big[\sum_{i=0}^{i=N}\{a_i\big(U(u_{i+1}) - U(u_i)\big) + b_i\big(V(u_{i+1}) - V(u_i)\big)\} + \int_{u_N}^{t-\varepsilon}(t-\tau)^{\alpha-1}F_c(\tau)d\tau + F_c(t)\frac{1}{\alpha}\varepsilon^{\alpha} + \frac{F_c(t) - F_c(t-\varepsilon)}{\varepsilon}\frac{1}{\alpha+1}(-\varepsilon^{\alpha+1})\Big] \quad (3.6)$$

This approach reduces the calculation time significantly. For example, when computing the convolution from 0 to 0.1 s with the time step of 0.01 ms, the approximated convolution

of Eq. (3.6) is about 90 times faster than the numerical integration with no modification. Also, the error due to the approximation made in Eq. (3.6) was checked for $F_c(\tau) = \tau^2$ because an exact solution exists for this F_c. When integrating from 0 to 0.1 s with the time step of 0.01 ms, the error is about 1%.

3.3.2 Relation between the FBM and the complex modulus

Because a viscoelastic fluid allows energy storage and loss, its modulus contains both real and imaginary part. In the frequency domain, the complex modulus G is expressed as $G(f) = G'(f) + jG''(f)$, where f represents frequency. The value of the real and imaginary part are determined by MSD and α as follows [94]

$$
\begin{aligned}
|G(f)| &= \frac{k_B T}{\pi r MSD(t = 1/f)\Gamma[1 + \alpha(f)]} \\
G'(f) &= |G(f)|cos(\pi\alpha(f)/2) \\
G''(f) &= |G(f)|sin(\pi\alpha(f)/2),
\end{aligned}
\tag{3.7}
$$

where r is radius of the interesting sphere in the fluid. The phase of the complex modulus can be expressed with α. A α value of 0 (or 1) corresponds to a fluid which is purely elastic (or purely viscous). For the fluid characterized by a single fractional number, a small α indicates that the fluid has higher elasticity and lower viscosity and vice versa. G_r and f_r are used to determine the magnitude of the complex modulus. The magnitude at a certain frequency depends on the values of MSD and α at that frequency. Also, MSD depends on α and ζ [87] as follows

$$
MSD(t) = \frac{k_B T}{\zeta} \frac{sin(\alpha\pi)}{\pi(1 - \alpha/2)(1 - \alpha)\alpha} t^{\alpha}. \tag{3.8}
$$

Thus, ζ in Eq. (3.3) is determined using Eqs. 3.7 and 3.8.

The parameter f_r is a reference frequency (a value around 0.01 s^{-1}). The parameter G_r is the ratio of G'' for water and G'' for the fluid of interest at the reference frequency $f = f_r$.

If viscosity and elasticity are caused by independent elements like a spring and a dashpot, then one can define viscosity and elasticity separately. Then, it is easy to observe their effects separately. For a fluid of a single fractional number, however, viscosity and elasticity are coupled by the fractional number. Therefore, it is impossible to change one property while the other is fixed. Either viscosity or elasticity can be the reference for the magnitude of viscoelasticity. If the elasticity is used as the reference value, then a fluid characterized by a large α has higher elasticity and higher viscosity than a fluid characterized by a small α. Then, the comparison of the motion of kinesin over α can become unclear because both properties increase with α. Thus, using G'' as a reference value of viscosity can lead to more clear comparisons for various values of α.

G'' has a slope of α over frequency in a log scale. Thus, the ratio between G'' and G''_{water} changes over frequency. The reference frequency f_r deals with this issue. When $f > f_r$, the smaller α is, the lower the viscosity of the fluid is. When $f < f_r$, the relation between α and viscosity is reversed. As we want a fluid of small α to have low viscosity over a wide range of frequencies, f_r is chosen to have a low value ($f_r = 0.01s^{-1}$), as shown in Fig. 3.2.

3.3.3 Calculation procedure

To compute the motion using our model, the variables which determine the mechanochemical motion of kinesin are updated in time. During each time step Δt (which typically is a small fraction of the dwell time) the cargo and neck interact as given by the mechanical governing equations (Eqs. 2.1– 2.4 and 3.6). The (past) data is stored to evaluate the

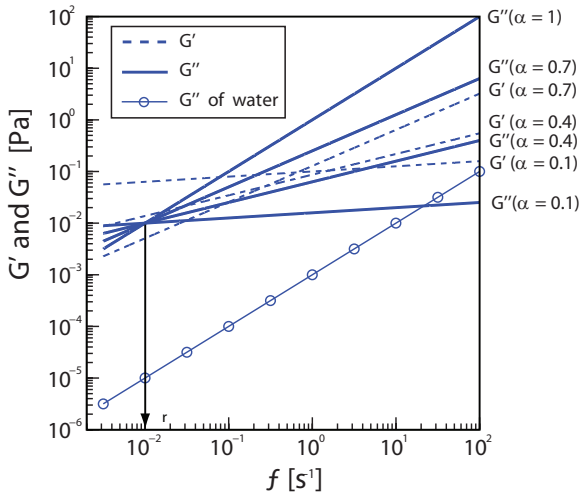

Figure 3.2: Complex modulus for G_r =1,000, and α =0.1, 0.4, 0.7 and 1.

memory effects due to the viscoelastic fluid. At the current time instant t, the required (past) data are the value of $F_c(\tau)$ for all τ from u_N to $t-\Delta t$, $x_{fhd}(t-\Delta t)$, $x_{bhd}(t-\Delta t)$, $x_n(t-\Delta t)$, $x_c(t-\Delta t)$, ρ, $\int_0^{t-\Delta t} F_c d\tau$, and $\int_0^{t-\Delta t} \tau F_c d\tau$. Here, Δt denotes the time interval between the current time instant t and the previous time instant. The cargo is assumed to interact with a kinesin at time t in the same mode as at time $t-\Delta t$. Note that there are three different modes of interaction between the cargo and a kinesin as described in Fig. 2.3.

Next, the values of three variables (x_c, x_n and F_c) are calculated at the current time t using Eq. (2.1) (which provides two relations) and Eq. (3.6) (which relates $x_c(t)$ and $F_c(t)$).

Next, the newly calculated variables are used to ascertain if they satisfy the assumed interaction (e.g., slack or no slack, assisting or resisting loads, etc). If they do not satisfy the assumed interaction, then the interaction type is updated and the calculation for the dynamics is carried out again over that time step.

Next, the rate of the chemical state variable is obtained using Eqs. 2.7 and 2.6. Then,

the value of ρ is calculated as $\rho(t) = \rho(t - \Delta t) + \frac{d\rho}{dt}\Delta t$. If $\rho(t)$ is between 1 and -1, the chemical cycle has not completed. Thus, the heads of kinesin remains in their previous position. If $\rho(t)$ is larger than 1 (or less than -1), the time instant $\widetilde{t}$ when the chemical cycle is completed ($t - \Delta t \leq \widetilde{t} \leq t$) is computed by capturing the instant when ρ becomes 1 (or -1) through a linear interpolation. The positions and forces at the current time are also changed to the values corresponding to $\widetilde{t}$. At that instant the heads are assumed to change positions. Namely, the trailing head is instantaneously relocated to the next binding site because the diffusion of the head is assumed to occur instantaneously. Also, the forces are updated to the values corresponding to that instant and those new positions. This procedure is carried out at every time instant during the calculation.

3.4 Results

In most previous studies of kinesin transport, the effects of the properties of the fluid were not analyzed because they do not play a major role *in vitro*. In a highly viscoelastic fluid, however, the properties of the fluid can have significant influences on kinesin behavior. The model introduced in this chapter is designed to account for these effects. Since the friction exerted by the fluid decreases with the size of the cargo, a nano-sized cargo may be too small to clearly highlight the effectiveness of the model. Hence, the radius of the cargo was selected as 1 μm because that is the size of large intracellular cargoes such as mitochondria [98].

In this section, we analyze the motion of kinesin in fluids with various properties to reveal the effects of viscosity and elasticity. In addition, the response of kinesin to fluctuating loads is examined by using the ability of the model to predict transient dynamics. Notably, we observe that even if the magnitudes of the fluctuating loads are the same, the speed of the kinesin changes with the frequency of the load.

3.4.1 Effects of load and viscosity

Many researchers have demonstrated that the speed of kinesin *in vitro* depends on the load [25, 27–29]. If a single motor has no load, its *in vitro* velocity is about 800 nm/s when the concentration of ATP is 2 mM. The speed decreases to about 200$\sim$300 nm/s under a load of 6 pN. This speed is about 25 % of the speed in the absence of a load. This large decrease indicates that the effect of the load is dominant in a fluid of low viscosity. However, the dependence of the velocity on the load becomes weak if the fluid is highly viscous. When viscosity is 1,000 times higher than that of water, for example, the velocity under a high load (6 pN) is just 50 % of the velocity under no load. Another noticeable feature is the nonlinear relationship between load and velocity. For a fluid having low viscosity, kinesin maintains its highest velocity (for a given ATP concentration) even if the load is small ($0 \sim 3$ pN). As the load increases, the velocity of kinesin starts to decrease. The rate of decrease keeps growing with the load. This nonlinear behavior of kinesin abates in a highly viscous fluid. Because kinesin significantly slows down when moving in fluids with high viscosity (even without a load), its force-velocity curve has an almost constant slope for high G_r, as shown in Fig. 3.3. Similarly, Fig. 3.4 shows that the effects of the load are more pronounced as G_r decreases.

3.4.2 Effects of elasticity

For viscoelastic fluids, it is difficult to observe the effects of elasticity when G_r is small. Fluids governed by the GLE have viscosity and elasticity that are proportional to G_r. So, in the range of low G_r, viscous and elastic force are weak. To observe the effect of elasticity, transport velocities in fluids with complex moduli corresponding to G_r higher than approximately 200 are needed to be compared. Thus, velocities of kinesin for various α were calculated for G_r values of 500, 1,000 and 1,500.

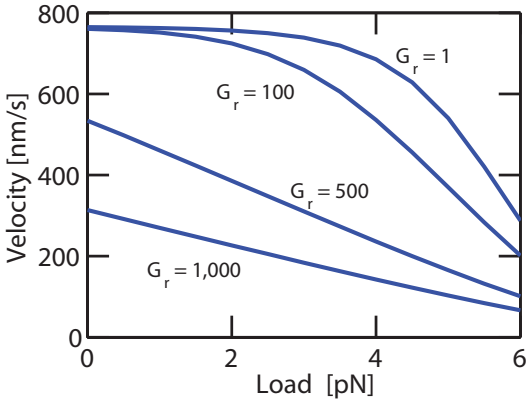

Figure 3.3: Effect of load on force-velocity curves for transport in various purely viscous fluids; [ATP] = 2 mM.

The effect of the elastic component of the fluid force depends on α, as shown in Fig. 3.5. Recall that a small α value corresponds to a low viscosity and a high elasticity. This property results in the rapid deceleration of the high initial velocity. The velocities can be examined by dividing the motion into three parts. At the beginning ($t < 0.2$ s), the motion in the fluid with smaller α is faster because the viscous force is small while the elastic force is negligible (Part 1). As the kinesin moves forward (0.2 s $< t <$ 3 s), the intriguing relation between α and velocities is revealed. Since elasticity creates different forces over α, the motor protein has high speeds at α = 0.3 $\sim$ 0.5 (Part 2). For longer travel ($t >$ 3 s), the speed of kinesin is approximately proportional to α (Part 3).

Part 3 may be inconsequential for kinesin transport for the following reasons. First, Part 3 can only take place if kinesin were to move for a very long time, which would require a run length much longer than that of a typical single kinesin. In vitro, a single kinesin moves about 0.8 μm, and that takes about 1 s. After that, the kinesin detaches from the MT [25]. The run length depends on the load, but the order of magnitude of the time for

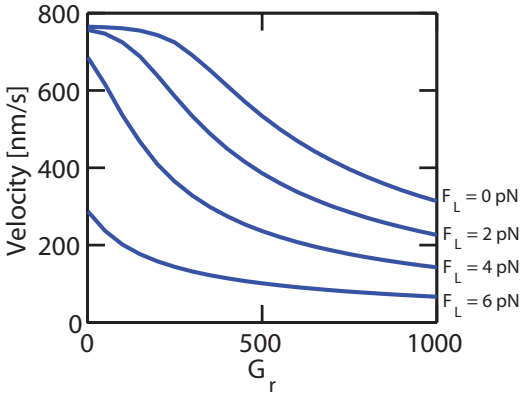

Figure 3.4: Effect of viscosity on velocity at various loads for transport in purely viscous fluids; [ATP] = 2 mM.

a run length does not change significantly. If this run length and its duration are also valid for viscoelastic fluids, then Part 2 will dominate the motion of a single kinesin. Although the run length increases by some factor [99], kinesin may not have an opportunity to enter into Part 3. Thus, if the steady state begins during Part 2, then there will be no Part 3.

The elastic force exerted by the fluid on the cargo is related to the displacement of the cargo. A simple spring cannot be an accurate substitute for the elasticity of a complex fluid. However, a combination of a spring and a virtual reference is a physically feasible approximation for the dynamics. Fig. 3.6 shows the conceptual explanation of the function of the elastic force on a molecular motor. When a cargo starts to move in the fluid, the elastic component of the fluid force is small and proportional to ℓ, where ℓ refers to the distance between the cargo and the virtual reference. As the kinesin continues to move, the cargo and the virtual reference move also. The cargo moves faster than the virtual reference, and the difference in their velocities increases ℓ, which in turn increases the elastic component of the fluid force. The increased force decreases the speed of kinesin until the motion of the cargo and the virtual reference are balanced. Then, ℓ does not

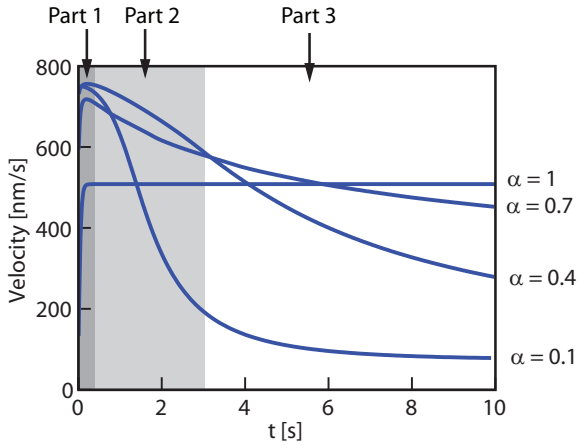

Figure 3.5: Velocity over time for [ATP] = 2 mM, G_r = 1,000, α = 0.1, 0.4, 0.7 and 1. For α of 1, the velocity does not change because there is no elastic force. For α less than 1, the velocity decreases over time due to the growth of the elastic component of the fluid force.

change, and $\ell = \ell_s$.

To capture the steady state motion, the memory function in the GLE has to be modified. The original memory function contains all past states. Thus, the continuously accumulating states in the function prohibit a steady state. However, for a long travel, states from the distant past have no effect on the current motion of kinesin. This is similar to the idea of a virtual reference. That means that there exists a limited range of time in which the memory function varies. Beyond that, the memory function should have a constant value. This physically insightful approach, however, raises a challenge, namely that the current data about the cytoplasm do not supply too many clues about the steady states. Nevertheless, we can estimate the limited range from the experiments on the steady state motion of kinesin in the following way. In a cell, a cargo proceeds by pushing its way through polymers in the cytoplasm. In this motion, the key for establishing the limited range is the effective length, ℓ_s. This length indicates the distance over which one polymer affects the cargo. ℓ_s depends on the size of the cargo and the length of the polymers. We assume that

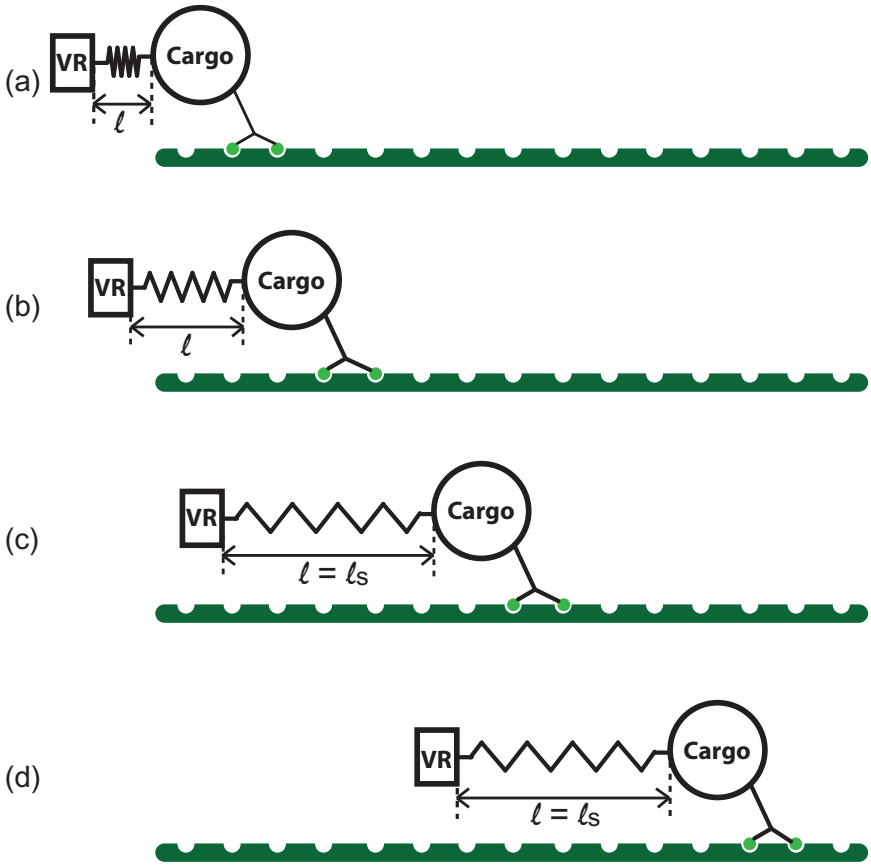

Figure 3.6: Behavior of the elastic component of the fluid force. VR denotes the virtual reference. When the motion of the cargo starts, ℓ is very small (a). ℓ increases as the kinesin moves (b). The steady state begins, and ℓ becomes ℓ_s (c). In the steady state, ℓ remains constant $\ell = \ell_s$ (d).

the average effect of the length of the polymers on ℓ_s is the same regardless of the values of α and G_r. If this assumption is applicable for a wide range of G_r, the size of the cargo is the only parameter that determines ℓ_s. Thus, ℓ_s is assumed to be proportional to the radius of the cargo ($\ell_s = \beta r$, and β is constant over G_r and α). In experiments with kinesin in an artificially mixed viscoelastic fluid (α = 0.51, G_r = 1,590 and [ATP] = 1 mM), the steady state velocity of a single motor is about 370 nm/s [79]. By inserting this data into our model, the value of β was calculated as 0.25. With the concept of ℓ_s, the steady state velocities were obtained for G_r = 500, 1,000, and 1,500 and [ATP] = 2 mM are shown

in Fig. 3.7. These results support the idea that the steady state begins during Part 2. The exciting result is that a single kinesin can transport cargoes faster in a viscoelastic fluid than in a purely viscous fluid, and it has a maximum velocity (for a given value of G_r) when α is between 0.4 and 0.5, as shown in Fig. 3.7. This indicates that a ratio of approximately 0.5 between elasticity and viscosity builds the optimal circumstance for the fast transport (done by a single kinesin) in a highly viscoelastic fluid.

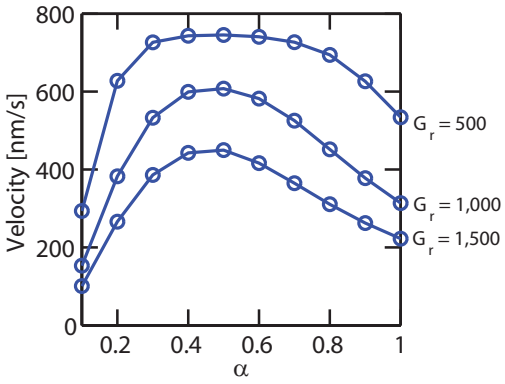

Figure 3.7: Steady state velocity versus α for G_r = 500, 1,000, and 1,500.

3.4.3 Motion of vesicles *in vivo*

Kinesins are involved in fast anterograde axonal transport. Their degraded intracellular transport capacity can cause neurodegenerative diseases [100]. Thus, speed of kinesin is one of the most significant characteristics of the transport. The speed of kinesin *in vivo* is affected by the viscoelasticity of the cellular fluid. The characteristics of the viscoelastic fluid may lead to a slower or a faster transport.

The key parameters of the viscoelastic fluid are α and G_r. Parameter α provides information regarding the ratio between viscosity and elasticity, and parameter G_r is an indicator for the magnitude of energy dissipation/viscosity/friction in the fluid. The model

is able to predict the motion of kinesin if α or G_r are constant over frequency, as happens in some cytoplasm. Hill et al. [80] measured the MSD of vesicles in the neurites of PC12 cells. They also tracked the motion of vesicles of radius 0.3 $\sim$ 0.4 μm which are transported by kinesin. They found an average velocity of 1,250 $\mathrm{nm/s}$. The complex modulus of the cytoplasm of PC12 cells follows the FBM with the constant α and G_r ($\alpha = 0.75$ and $G_r = 2,154$), as shown in Fig. 3.8 (a). Our model predicts that for the G_r value of 2,154 (as in the PC12 cell), a cargo of radius 0.35 μm (the size of vesicles used in experiments) has high velocities when α is 0.2 $\sim$ 0.8 (Fig. 3.8 (b)). Though the predicted velocity is less than the observed velocity, α of 0.75 is the value for faster transport for the given G_r value. Note that the speed of vesicles in PC12 cells changes over time [80]. This speed is even higher than the maximum speed of a single kinesin *in vitro*. This considerably faster transport was also found by other researchers [52, 53, 101]. Thus, it is possible that the faster transport observed *in vivo* is due to other factors such as the cooperation of several kinesins. We also note that the values of α for several other cytoplasms vary over frequency [102]. Thus, the FBM with fixed α and G_r is not a general tool to predict motion of beads in any cytoplasm.

3.4.4 Effects of the frequency of fluctuating loads

The model provides accurate predictions for transient motions of kinesin. To observe the dynamics of kinesin under time-varying loads, sinusoidally fluctuating loads are applied to the cargo. Of course, these fluctuations are transfered to the motor heads through the linkers. Thus, the rate of chemical reaction at the heads changes. The behavior of the cargo can be conceptually understood as the motion of a very small body connected to the ground by a spring and a dashpot. If the body experiences a fluctuating load, the amplitude of its fluctuating displacement is inversely proportional to the spring stiffness, the dashpot

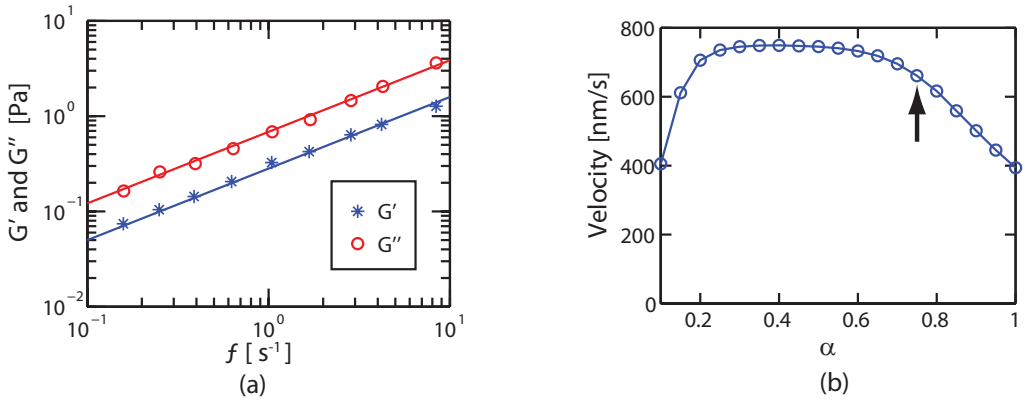

Figure 3.8: (a) The complex modulus of PC12 cell. Circles and stars are the experimental data, and lines represents the complex modulus of $\alpha = 0.75$ and $G_r = 2,154$. (b) The predicted velocity of the cargo of radius 0.35 μm for $G_r = 2,154$ and various α. The arrow indicates the velocity corresponding to the property of PC12 cells.

viscosity and the frequency of the load. Similar to that simple system, the fluctuations in the position of the cargo decrease as the viscoelasticity of the fluid increases, or the frequency of the load increases. As a result, the effects of the fluctuations vanish at high frequency, and the velocity-frequency curve flattens. In contrast, at lower frequencies, this curve has exponential variation. The approximate exponential curve is obtained using least mean square fitting to exact model predictions.

To discover the relationship between the motion of kinesin and the frequency of the load, two values are calculated: the changes in velocity (Δv), and the frequency (f_τ) corresponding to 90 % of the velocity difference. These values are shown in Fig. 3.9 (a). For G_r = 500, the changes in velocity over frequency are large compared to other G_r values, and Δ v has its highest value at α = 0.6. The dependence of the velocity on frequency becomes weak when the viscoelasticity is strong, as shown in Fig. 3.9 (b) (not unlike the case of a rigid body connected to the ground by a spring and dashpot). The value of f_τ also decreases over G_r. The velocity for high G_r saturates at a relatively

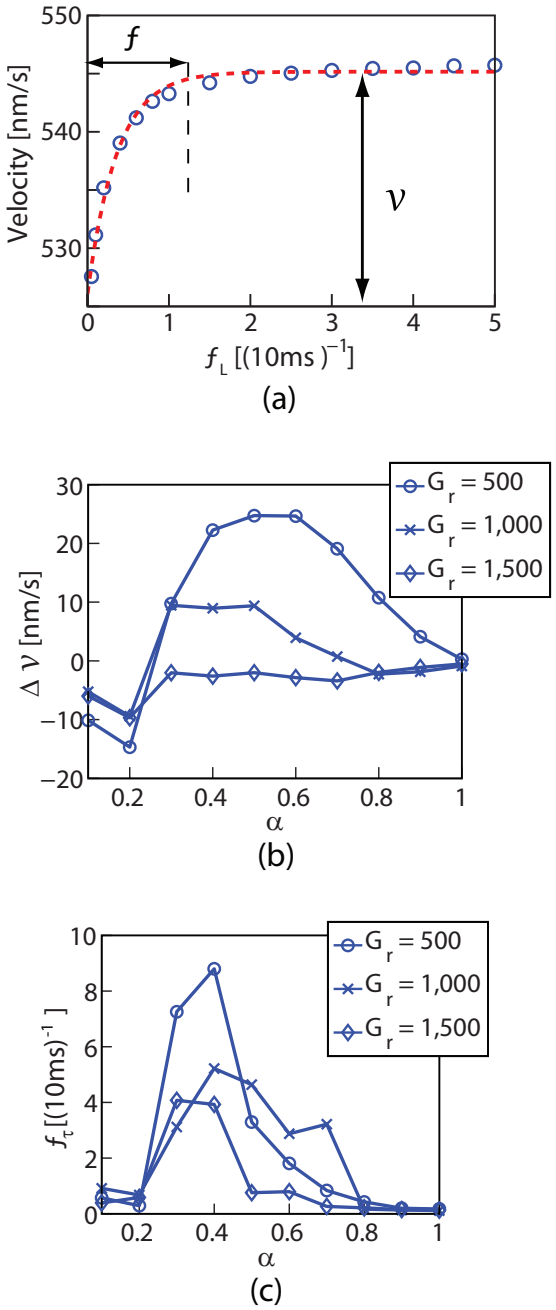

Figure 3.9: The response of kinesin to a load of $F_L(t) = 2 - 2sin[(2\pi f_L)t]$. f_L denotes the frequency of the load. (a) Velocity-frequency curve for α = 0.7, G_r = 500. (b) Δv versus. α for G_r = 500, 1,000, and 1,500. (c) f_τ versus. α for G_r = 500, 1,000, and 1,500.

low frequency because viscoelasticity accelerates the saturation of the velocity-frequency curve, as shown in Fig. 3.9 (c). This result indicates that kinesin is more sensitive to a fluctuating load in a fluid with low viscoelasticity than in a fluid with high viscoelastcitiy.

3.5 Conclusions

The newly developed model for the motion of kinesin provides solutions for several restrictions of existing models. By regarding a kinesin molecule as a structure composed of linearly elastic elements, it is possible to capture its transient and steady state dynamics. This approach also enables the prediction of the response of molecular motors under time varying loads. For a sinusoidally fluctuating load, the speed of kinesin changes with the frequency of the load. However, the effects of the fluctuation disappear at high frequency.

To describe the transport done by kinesin in a viscoelastic fluid, the GLE was applied to the model. The GLE was converted into a form which is suitable for calculating displacements with previous forces. This method is also useful for analyzing movements of other motor proteins in the presence of subdiffusion.

The cytoplasms is a highly viscoelastic fluid. We focused on the effect of large viscosity and elasticity on transport performed by molecular motor. Fluids having viscosity comparable with that of water do not have significant effects on the motion of kinesin. However, highly viscous fluids decrease the speed of kinesin to a quarter of its velocity in water. Moreover, the high viscosity also influences the shape of the force-velocity curve. While the curve for a fluid with low viscosity has a region where velocities are almost constant, the presence of large viscosity excludes that behavior.

To observe the effect of elasticity, the velocity of kinesin was calculated for various α. Due to the complicated features of the complex modulus in subdiffusion, the viscoelastic properties were carefully designed. For fluids exhibiting subdiffusion, viscosity and elas-

ticity cannot be changed individually. It would be great if a fluid of small α would have a lower viscosity and higher elasticity than another fluid of high α. However, it is unavoidable that this relation is not followed in some frequency range for fluids following FBM. This problematic frequency range was reduced by a carefully selected reference frequency and by choosing the viscosity as the reference value for the magnitude of viscoelasticity. However, for a pure FBM, the elastic component of the fluid force grows as a motor walks. As a result, the α value (for the maximum instantaneous velocity) changes over time. Initially, α corresponding to the maximum velocity is 0.1. If a steady state analysis is pursued, the value continuously increases over time.

Experimental data obtained through passive microrheology provides only limited information regarding the steady motion of a particle under a constant force in a cellular fluid. To address this issue, we used experimental steady state velocity values for cargoes transported by kinesin in a viscoelastic fluid and made an assumption regarding the effective length of the memory function. This approach predicted that kinesin has a maximum steady state velocity when α is $0.4 \sim 0.5$. Experimental research could verify this result. Also, the distance ℓ_s for a cellular fluid can be measured by exerting a constant force to a particle which is not connected to kinesins and measuring the distance that the particle moves before its velocity does not change over time. Moreover, the fundamental equation used in this chapter is available for the FBM having a single fractional number. This approximation is well suited for artificially created fluids and simulated cytoplasm [35, 79, 81]. However, it is not guaranteed that this relationship holds for every fluid. To cover more general cases, the memory function has to be extended to the level of describing the FBM with multiple fractional numbers. In addition, it is likely that a spatially varying complex modulus is present *in vivo*. That may require the memory function to transform continuously with the change in the complex modulus.

CHAPTER IV

Effects of kinesins binding/unbinding on their collective transport

4.1 Summary

In this chapter, the unbinding of kinesin from the MTs and the rebinding to the MTs are characterized with stochastic models. Then, the unbinding and rebinding models are integrated with the mechanistic model for the walking motion (chapter II) to predict the collective transport of a cargo when several kinesins are attached to the cargo. The results of this chapter suggest that the collective transport is beneficial particularly for the long range intracellular movements because the run length of the cargo increases dramatically over the number of the kinesins.

4.2 Background and motivation

Several experiments have measured the run length of cargoes transported by kinesins. Block et al. [30] reported that cargoes move about 1.4 μm when they are pulled on average by about one and half kinesin molecules. The distribution of the run length in those experiments follows an exponential probability distribution. The effects of external resisting loads exerted on the cargo and the concentration of ATP on the run length was observed by Schnitzer et al. [25]. The run length decreases with increasing resisting load and de-

creasing ATP concentration. In the experiment performed by Uemura et al. [103, 104], the magnitude of the loads causing unbinding were measured. They exerted loads toward the plus or the minus-end of the MTs to discover the effects of the direction of the load. Their results show that kinesins tend to unbind more easily when subjected to loads toward the plus-end of the MTs than by loads toward the opposite direction. However, the difference is not considerable. The experiment of Beeg et al. [2] focused on the transport of cargoes by groups of kinesins. To observe the relation between the number of kinesins and the run length, they varied the number of kinesins attached to the cargo. The run length increased as more kinesins participate in the transport. However, the run length was surprisingly reduced when the cargo was moved by considerably many kinesins.

Mathematical models have been proposed to calculate the run length of kinesin. Schnitzer et al. [25] established an equation regarding the run length of a single kinesin molecule by using Arrhenius-Eyring kinetics. The approach produced a successful fit to experimental data for various ATP concentrations and external loads. However, the model is only applicable to the motion of single molecules. For transport by several kinesins, Klumpp et al. [42] utilized discrete Markov chains to obtain a master equation regarding the number of motors which effectively participate in the transport. Then, they obtained the stationary solution for the master equation. By substituting the transition rates of kinesins (i.e., binding rate to MT, and unbinding rate from MT), their model obtained an analytical solution for the mean value and the probability density function (pdf) of the run length. Their unbinding model accounts for the effects of load by assuming that the load is equally distributed over every kinesin bound on the MT. However, the distribution of loads over motors continuously changes due to the stochastic motion of kinesins [51, 105, 106]. Furthermore, their binding model is not able to capture the locations where rebinding occurs, despite the fact that those locations also affect the collective transport.

The goal of this chapter is to develop a binding/unbinding model which is able to capture the stochastic unbinding and binding of kinesins to the MTs and their dependencies on the force acting on them. By using the model, the run length and velocity of collective transport under constant loads are obtained. The characterization on the unbinding of kinesins captures an interesting behavior of kinesins, namely that they spend a long time remaining on the MT when large resisting loads are applied. The model predicts that this behavior of kinesin is beneficial for the cargo to overcome obstacles. Also, the velocity of collective transport is affected by the stochastic rebinding process as well as by the velocity of kinesin molecules itself.

4.3 Models

The mechanistic model introduced in chapter II is used to capture the walking motion of kinesins. Kinesin molecules are assumed to have state [K+MT], $[\mathrm{K.ATP} + \mathrm{MT}]_1$, $[\mathrm{K.ATP} + \mathrm{MT}]_2$, or $[\mathrm{K.ADP.Pi} + \mathrm{MT}]$ when they are bound to the MT. Thus, before calculating the unbinding probability, the instant of the transition between bound states is captured by the mechanistic model. The details of the mechanistic model are provided in chapter II. Both heads of kinesin are strongly bound during the state $[\mathrm{K.ATP} + \mathrm{MT}]_2$ and $[\mathrm{K.ADP.Pi} + \mathrm{MT}]$. Thus, it is assumed that the probabilities to unbind during the states $[\mathrm{K.ATP} + \mathrm{MT}]_2$ and $[\mathrm{K.ADP.Pi} + \mathrm{MT}]$ are negligible, and the preponderance of instances of unbinding occurs either from state $[\mathrm{K} + \mathrm{MT}]$ or state $[\mathrm{K.ATP} + \mathrm{MT}]_1$. Thus, the unbinding probabilities corresponding to states $[\mathrm{K} + \mathrm{MT}]$ and $[\mathrm{K.ATP} + \mathrm{MT}]_1$ are calculated in this chapter.

Among several kinesins connected to a cargo, some kinesins walk along the MT, and others are not attached to the MT but just follow the cargo. Since both heads of unbound kinesins are free from the MT, the position of these heads fluctuates over time. The effect

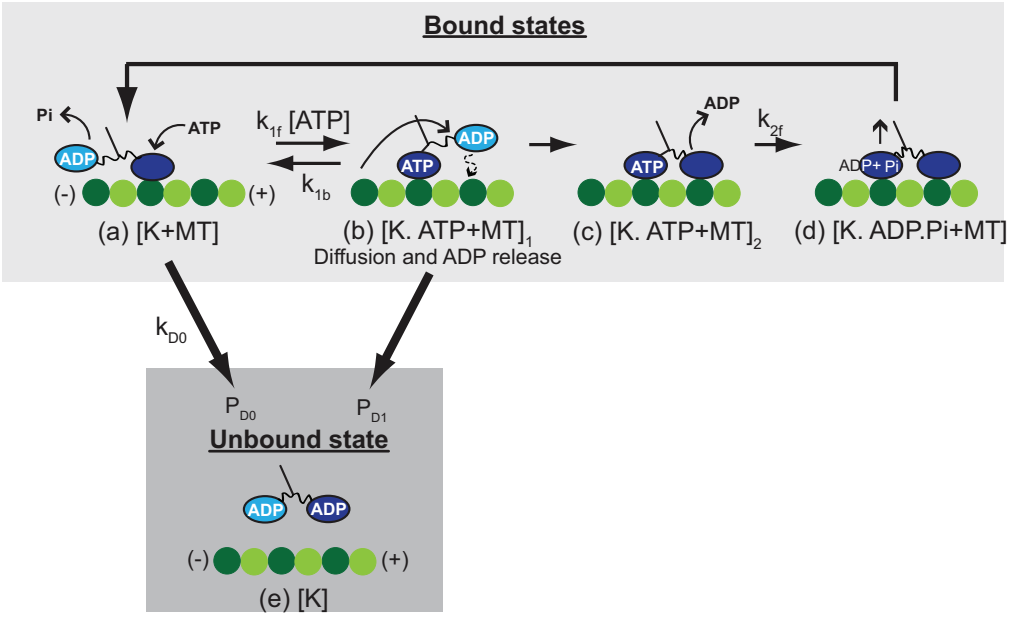

Figure 4.1: The kinesin cycle. The states in the upper box relate to the walking cycle of the kinesin. K denotes the kinesin molecule. The lower box relates to the unbound state of the kinesin. The variables denoted by k are transition rates between states, and P_{D0} and P_{D1} represent the probability of unbinding from the MT when the kinesin is in the state $[\mathrm{K} + \mathrm{MT}]$ and $[\mathrm{K.ATP} + \mathrm{MT}]_1$. (a) An ATP molecule binds to the leading head of the kinesin. (b) The binding of ATP to the kinesin head results in a structural changes in the head [1]. This change induces the docking of the NL to its head. The docking of the NL to the leading head generates a force to move the trailing head toward the plus-end of MT. Then, the trailing head diffuses to the next binding site of MT by Brownian motion. (c) The moving head binds to the MT and releases ADP. (d) ATP in the rear head is hydrolyzed, and then this hydrolysis enables the release of phosphate (Pi) from the head. Then, the NL returns to the disordered state from the docked state.

of this fluctuation on the rebinding is included in the model by calculating the pdf of the positions of unbound kinesins.

4.3.1 Unbinding model

The unbinding probability during the state $[\mathrm{K} + \mathrm{MT}]$ is calculated over time using the transition rate k_{D0} from the state $[\mathrm{K} + \mathrm{MT}]$ to the unbound state [K], as shown in Fig. 4.1.

If the i^{th} cycle starts at an instant t_i, the unbinding probability in state [K+MT] during this cycle is obtained by solving the following set of equations with the initial condition $P_{[K+MT]}(t = t_i) = 1$.

$$\frac{d}{dt}P_{[K+MT]} = -k_{D0}P_{[K+MT]}, \tag{4.1}$$
$$P_{[K+MT]}(t) + P_{D0}(t) = 1,$$

where $P_{[\mathrm{K+MT}]}$ is the probability that kinesin remains attached to the MT, and $P_{D0}(t)$ is the unbinding probability in state [K+MT]. Thus, the growth of P_{D0} over time can be calculated as

$$P_{D0}(t) = 1 - \exp(-k_{D0}t) \tag{4.2}$$

The time constant of the cargo motion transported by single kinesin was experimentally measured by Carter et al. [27] to be approximately $15.3\ \mu\mathrm{s}$ for a resisting load of 5 pN applied to the cargo. The dwell time of kinesin has also been measured experimentally by numerous researchers for that load, including Visscher et al. [28]. That dwell time is about 70 ms. Hence, the duration of state $[\mathrm{K.ATP} + \mathrm{MT}]_1$ is much shorter than the dwell time and thus negligibly short. Due to this very short duration of state $[\mathrm{K.ATP} + \mathrm{MT}]_1$, a single unbinding probability value (i.e., P_{D1}) is used for this state instead of capturing the changes of the probability over time.

This model is able to predict the instant of transition between bound states. Thus, the effect of ATP concentration on unbinding is intrinsic to the model. The model also accounts for the effects of force by using Bell model [107] and expressions inspired by Boltzmann's law as

$$k_{D0} = k_{D0,0}\exp\frac{|F_{\mathrm{kin}}|d_0}{k_BT},$$
$$P_{D1} = P_{D1,0}\exp\frac{|F_{\mathrm{kin}}|d_1}{k_BT}, \tag{4.3}$$

where $k_{D0,0}$, $P_{D1,0}$, d_0, and d_1 are parameters of the unbinding model. F_{kin} is the force transferred from the cargo to the kinesin. The equation for this force is provided in chapter II. The occurrence of an unbinding event is determined by comparing the calculated probability with uniformly distributed random numbers.

The transport performed by a single kinesin does not include the rebinding process. Instead, the experimentally observed run lengths of single kinesins [25] are used to determine parameters of the unbinding model. The parameters of the model are obtained so that the model predicts run lengths measured experimentally. The fitting is done by using the nonlinear least-squares fit function (lsqnonlin) in MATLAB. Note that the results of the fitting indicate that the effects of the load on unbinding during the state $[\mathrm{K} + \mathrm{MT}]$ are very weak. Hence, d_0 is very small compared to other parameters. Thus, the value of d_0 is set as zero. Tab. 4.3.1 represents the values of the parameters, and Fig. 4.2 shows the run length of the experiments and the model. The values of the parameters can be changed by the interactions between kinesins. When the number of kinesins is small (e.g., between 1 and 5) and not considerably large (like hundreds), the effect of interference among kinesins on the unbinding of kinesins is assumed negligible. Thus, the parameters of unbinding used in this chapter apply to the cargoes transported by one to five kinesins.

4.3.2 Rebinding model

The kinesin released from the MT can possibly bind again to several binding sites, as shown in Fig. 4.3. The probability of rebinding to the j^{th} binding site is calculated using the transition rate $k_{A,j}$. The value of $k_{A,j}$ decreases as the distance between the unbound kinesin and the j^{th} binding site increases. The position of the neck and heads of the unbound kinesins are assumed to be the same. Thus, those positions are denoted by a single variable $x_{u,k}$. The dependence on the distance is assumed to have a parabolic

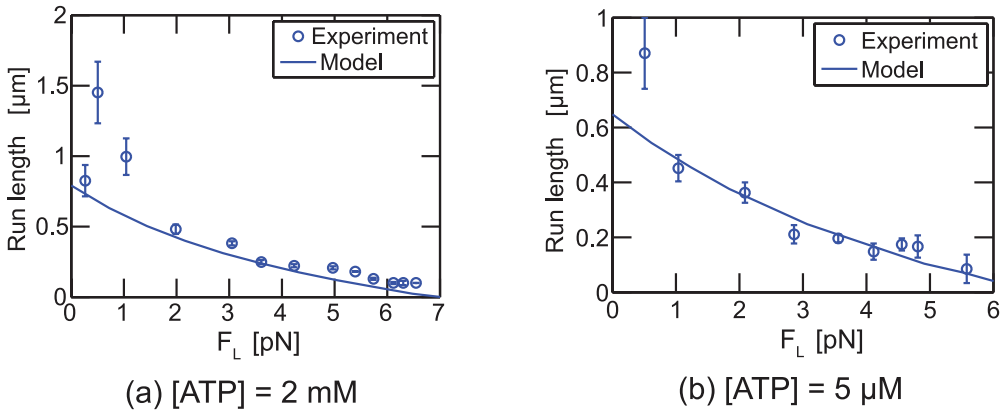

Figure 4.2: The run length of single kinesins. (a) shows the run length for various loads for [ATP] = 2 mM; (b) shows the run length when [ATP] = 5 μM.

Table 4.1: The values of parameters regarding unbinding.

Parameter	Value	Unit
$k_{D0,0}$	0.01633	s^{-1}
$P_{D1,0}$	0.01	probability
d_0	0	nm
d_1	1.272	nm

distribution, as shown in Fig. 4.3.

Since the time scale of the thermal fluctuations of an unbound kinesin is very short, the value of $k_{A,j}$ (which depends on the position of the unbound kinesin) also changes rapidly over time. Intensive computations are required to capture the value of $k_{A,j}$ over time. Instead of calculating the rapidly changing $k_{A,j}$, the following method is used. First, the pdf of the position of the unbound kinesin is obtained by using the strain energy in the kinesin structure. Then, the time average of $k_{A,j}$ is obtained at every time step by

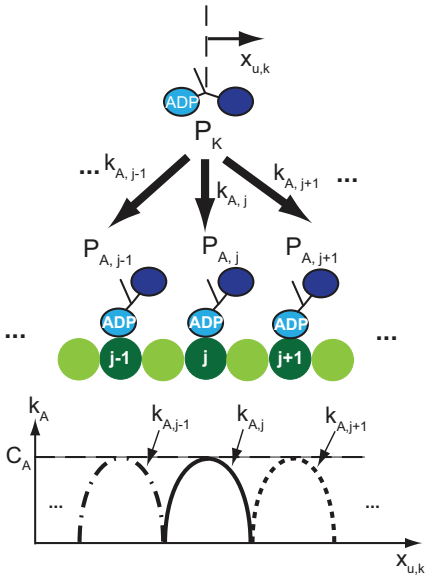

Figure 4.3: The rebinding of the unbound kinesin. The unbound kinesin has probabilities to rebind at several binding sites of the MT. P_K is the probability to stay in the unbound state, while $P_{A,j-1}$, $P_{A,j}$, and $P_{A,j+1}$ are the probabilities to rebind at the $(j-1)^{\text{th}}$, j^{th}, and $(j+1)^{\text{th}}$ binding site. $k_{A,j}$ is the transition rate from the unbound state to the bound state at the j^{th} binding site. The values of k_{A_j-1}, k_{A_j}, and k_{A_j+1} vary over the position of unbound kinesin $x_{u,k}$ with respect to the position of binding sites of the MT. C_A is a parameter of the model which denotes the rate of rebinding to a certain binding site when the unbound kinesin is exactly above that site.

spatially integrating the value of $k_{A,j}$ weighted by the pdf of the unbound kinesins. By using this method, the amount of computation reduces significantly because the time step can be determined by the dynamics of bound kinesins not by the fluctuating motion of the unbound kinesin.

pdf of the position of the unbound kinesin

The pdf of the position of the unbound kinesin is obtained by using two pdf of position (i.e., the pdf of the cargo and pdf of unbound kinesin with respect to the cargo). The pdf of the position of the cargo can be obtained using the Boltzmann law, $P \propto \exp(-E/k_BT)$,

where E is the mechanical potential energy in the kinesin. When only one kinesin is bound to the MT, the potential energy arisen from the tension in the bound kinesin is calculated as

$$E_c(x_c) = \begin{cases} \frac{1}{2}K_e(x_c - x_r - L_c)^2 + F_L(x_c - < x_c >) & \text{if } x_c > x_r + L_c, \\ \frac{1}{2}K_e(x_c - x_r + L_c)^2 + F_L(x_c - < x_c >) & \text{if } x_c < x_r - L_c, \\ F_L(x_c - < x_c >) & \text{otherwise,} \end{cases} \tag{4.4}$$

where E_c is the potential energy of the bound kinesin, and $x_r = \frac{1}{2}(x_{fh} + x_{bh})$ is the position in the middle of two heads. $K_e = \frac{2K_nK_c}{2K_n+K_c}$ is the equivalent stiffness of kinesin due to its cargo linker and two NLs. K_c and K_n are the stiffness of the cargo linker and the NL. $< x_c >$ is the position of the cargo where F_L and F_{kin} are balanced. The potential energy of the cargo is shown in Fig. 4.4 (a). Using the spatial distribution of energy and the Boltzmann law, the pdf of the position of the cargo, $\text{pdf}(x_c = x)$, is obtained, as shown in Fig. 4.4 (b). The pdf of the position of the unbound kinesin ($x_{u,k}$) is obtained through two steps. First, the pdf of the unbound kinesin with respect to the cargo, $\text{pdf}(x_{u,k} - x_c = x)$, is calculated by considering the potential energy of the cargo linker of the unbound kinesin, as shown in Figs. 4.4 (c) and (d). Note that this pdf is identical with the pdf of the cargo in the absence of the load. This pdf is also assumed as invariant with respect to external loads on the cargo because the external loads do not act on the unbound kinesins. Next, the pdf of the unbound kinesin, $\text{pdf}(x_{u,k} = x)$, is determined by the convolution of two pdfs of x_c and $x_{u,k} - x_c$ as

$$\text{pdf}(x_{u,k} = x) = \int_{-\infty}^{\infty} \text{pdf}(x_c = u)\ \text{pdf}(x_{u,k} - x_c = x - u)\ du. \tag{4.5}$$

The pdf of the unbound kinesin is shown in Fig. 4.4 (e).

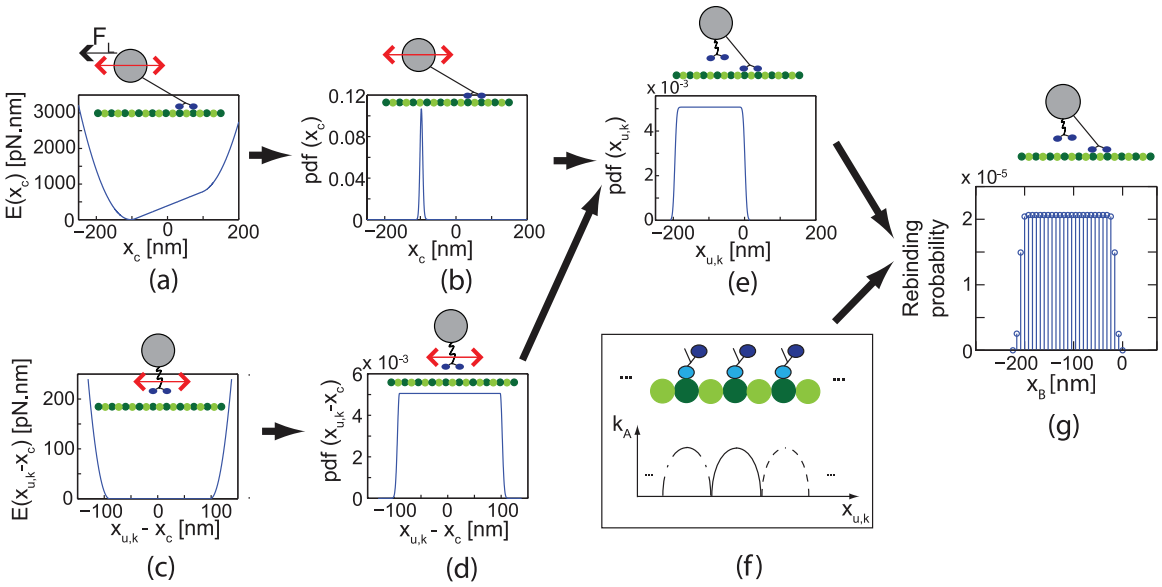

Figure 4.4: The rebinding model. The pdf of the position of the cargo $\mathrm{pdf}(x_c)$ (b) is obtained from the strain energy in the structure of the bound kinesins (a). The pdf of the position of the unbound kinesin respect to the cargo $\mathrm{pdf}(x_{u,k} - x_c)$ (d) is obtained from the strain energy in its structure (c). The pdf of the position of the unbound kinesin $\mathrm{pdf}(x_{u,k})$ (e) is calculated as the convolution of $\mathrm{pdf}(x_c)$ and $\mathrm{pdf}(x_{u,k})$. (f) shows the values of k_A over the position of unbound kinesin. (g) The rebinding probability on each binding site during a time step is obtained by using $k_{A,j}$ and $\mathrm{pdf}(x_{u,k})$.

Time average of the transition rate k_A

Instead of calculating the rapidly changing value of $k_{A,j}$ over time, the time average of the transition rate is used to avoid intensive computations with excessively short time steps for capturing the changes. The time average is calculated several times before a rebinding event so as to consider the changes in the position of the cargo by bound kinesins. This idea is depicted in Fig. 4.5. By using this approach, the probability $P_{A,j}(t, t+T)$ to rebind to the j^{th} binding site between two time steps t and $t+T$ can be expressed as

$$P_{A,j}(t, t+T) =< k_{A,j} > P_K(t)\, T, \tag{4.6}$$

where $< k_{A,j} >$ is the time average of $k_{A,j}$ between t and $t+T$. $P_K(t)$ is the probability that the kinesin remains in the unbound state until time is t.

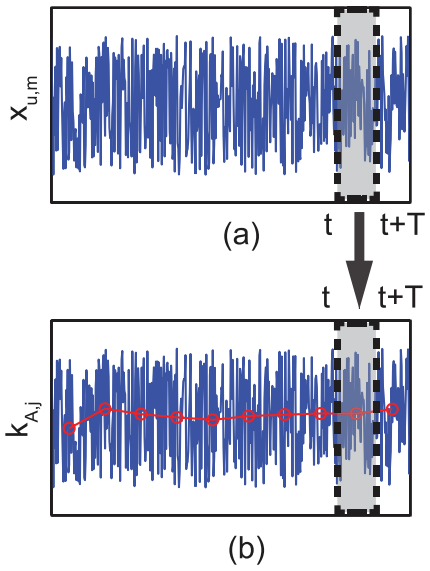

Figure 4.5: Time average of the transition rate. (a) shows the fluctuating position $x_{u,k}$ of unbound kinesin, and (b) shows the transition rate $k_{A,j}$ to rebind at the j^{th} binding site. The rate also fluctuates over time. Circles and the bold line indicate the moving average of the rate.

The efficiency of the computation is improved by converting the time average $< k_{A,j} >$ into a spatial average. First, by using the pdf of the unbound kinesin (i.e., $\text{pdf}(x_{u,k} = x)$), the time when $x_{u,k}$ is between two points (x_ℓ and $x_\ell + \Delta x$ in Fig. 4.6) during t and $t+T$ can be calculated as

$$\Delta\tau_\ell = T \int_{x_\ell}^{x_\ell+\Delta x} \text{pdf}(x_{u,k} = x)\, dx. \tag{4.7}$$

Then, the time average of $k_{A,j}$ is changed to the spatial average as followings.

$$\begin{aligned} < k_{A,j} > &= \frac{1}{T}\int_t^{t+T} k_{A,j}(\tau)d\tau = \frac{1}{T}\lim_{\Delta t\to 0}\sum_n k_{A,j}(t_n)\Delta t \\ &= \frac{1}{T}\lim_{\Delta x\to 0}\sum_\ell k_{A,j}(x_\ell)\Delta\tau_\ell = \int_{-\infty}^{\infty} k_{A,j}(x)\ \text{pdf}(x_{u,k} = x)dx \end{aligned} \tag{4.8}$$

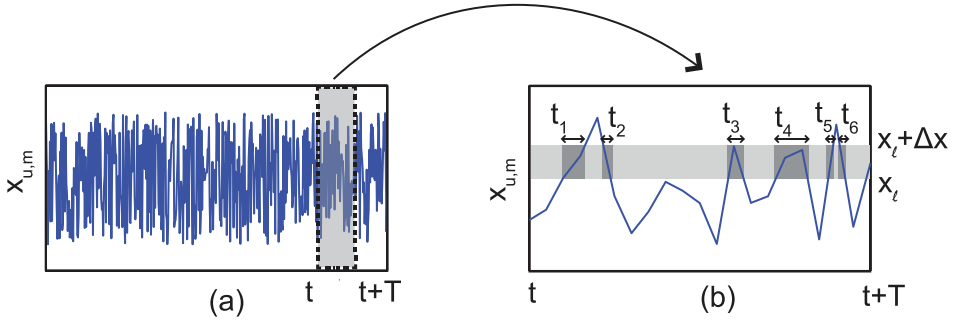

Figure 4.6: An example of fluctuation of the unbound kinesin. (a) shows the position of unbound kinesin over time. (b) shows details for $x_{u,k}$ between time steps t and $t+T$. $t_{1\ldots6}$ are the durations when $x_{u,k}$ exists between x_ℓ and $x_\ell + \Delta x$.

where $\mathrm{pdf}(x_{u,k} = x)$ is the pdf of the position of the unbound kinesin.

By using the pdf of the unbound kinesin and Eq. (4.6), the probability that the kinesin rebinds to each binding site between two time steps can be obtained, as shown in Fig. 4.4 (g).

In vitro experiments shows that kinesins rebind to the MT with the rate of approximately 5 s^{-1} in average in the absence of load [2, 108, 109]. Using this information, the maximal value of k_A (which represents as C_A in Fig. 4.3) can be determined as 7.68 s^{-1}. This value provides the average rebinding rate of 5.1 s^{-1} which is the rate reported in [2]. For various ATP concentrations and loads, the average rebinding rate remains almost the same. However, the rebinding probabilities over binding sites vary, as shown in Fig. 4.4 (g). The method to determine the instant and location of rebinding is provided in the following.

4.3.3 Simulation procedure

The simulation begins with the state where one kinesin is bound to the MT. The dynamics of the cargo, the chemical reactions and the unbinding are considered for bound

kinesins, and rebinding to the MT are considered for unbound kinesins at every time step. The positions of the necks of bound kinesins and cargo are obtained by using the mechanistic model (which is described in chapter II). Then, the chemical states the bound kinesins are determined from the mechanistic model. At the beginning of every cycle of bound kinesin, the unbinding probability is zero. Four uniformly distributed random numbers (e.g., r_w, r_{d0}, r_{d1}, and r_b) are also generated between 0 and 1 at the beginning of every cycle for each bound kinesin. The cycle of kinesin starts with state $[\mathrm{K} + \mathrm{MT}]$. First, if the value of P_{D0} becomes r_{d0} before the transition from $[\mathrm{K} + \mathrm{MT}]$ to $[\mathrm{K.ATP} + \mathrm{MT}]_1$ occurs, then the kinesin unbinds when P_{D0} is equal to the value of r_{d0}. Otherwise, the chemical state of kinesin changes to $[\mathrm{K.ATP} + \mathrm{MT}]_1$ when $P_{[\mathrm{K+MT}]}$ becomes r_w. Then, if the value of P_{D1} is higher than r_{d1}, then the kinesin unbinds during the diffusion of its free head. Otherwise, the free head moves to the next binding site without unbinding. At this moment, the free head can move to the forward binding site or to the backward binding site. The backward motion of kinesin can be captured by considering the diffusing motion of the kinesin head which is affected by the force acted on the kinesin molecule [110]. In this chapter, if the probability of backward steps (which is obtained using experimental results [27]) is larger than the random number r_b, the kinesin is assumed to move backward. Otherwise, it walks toward the plus-end of the MT. When $P_{[\mathrm{K+MT}]} + P_{[\mathrm{K.ATP+MT}]_2}$ becomes r_w, the transition from $[\mathrm{K.ATP} + \mathrm{MT}]_2$ to $[\mathrm{K.ADP.Pi} + \mathrm{MT}]$ occurs. If two or more kinesins are attached on the cargo, the probability distribution of rebinding for every unbound kinesin is also calculated at every time step. First, uniformly distributed random numbers r_{a1} and r_{a2} are generated for each unbound kinesin. If the summation of the rebinding probabilities over binding sites (shown in Fig. 4.4 (g)) are larger than r_{a1} at a certain time step, the rebinding occurs. Otherwise, the unbound kinesin does not bind to the MT at this time step. If the kinesin is determined to bind at this time step, the rebinding probabilities are normalized

with their summation. Then, the normalized rebinding probabilities are cumulated over binding sites. The kinesin binds to the binding site where this cumulative value is larger than r_{a2}.

4.4 Verification of the model

The run length and velocity calculated from the model were compared with the previous experimental data [2]. In that experiment, beads are mixed with kinesins to obtain cargoes coated with kinesins. Different concentrations of kinesins (c_k) were used to observe the effects of the number of kinesins attached to single cargoes. Their results are shown in Fig. 4.7. The results of the model for the used c_k are obtained as follows. The run length distribution and mean velocity of the cargo transported by one to five kinesins were calculated from the model. Then, the weighted averages of these results were calculated by using the probability regarding the number of kinesins (which was proposed in a previous study [2]) for each c_k. The run length distribution and mean velocity of the model are similar to the experimental results, as shown in Fig. 4.7.

4.5 Results

4.5.1 Unbinding probability

The unbinding probabilities for the states [K+MT] and $[\mathrm{K.ATP} + \mathrm{MT}]_1$ (i.e., P_{D0} and P_{D1}) are calculated for various forces applied to single kinesins and for various ATP concentrations, as shown in Fig. 4.8. The values of P_{D0} in Fig. 4.8 are unbinding probabilities when the time t in Eq. (4.2) is the average duration of state [K+MT]. When the resisting load is not significant, the duration is very short. Thus, P_{D0} is close to zero (e.g., for loads F_L between 0 and 5 pN at [ATP] = 5 μM). For large resisting loads, the duration of state [K+MT] is long. Hence, P_{D0} is large and increases with the load (e.g., for F_L loads be-

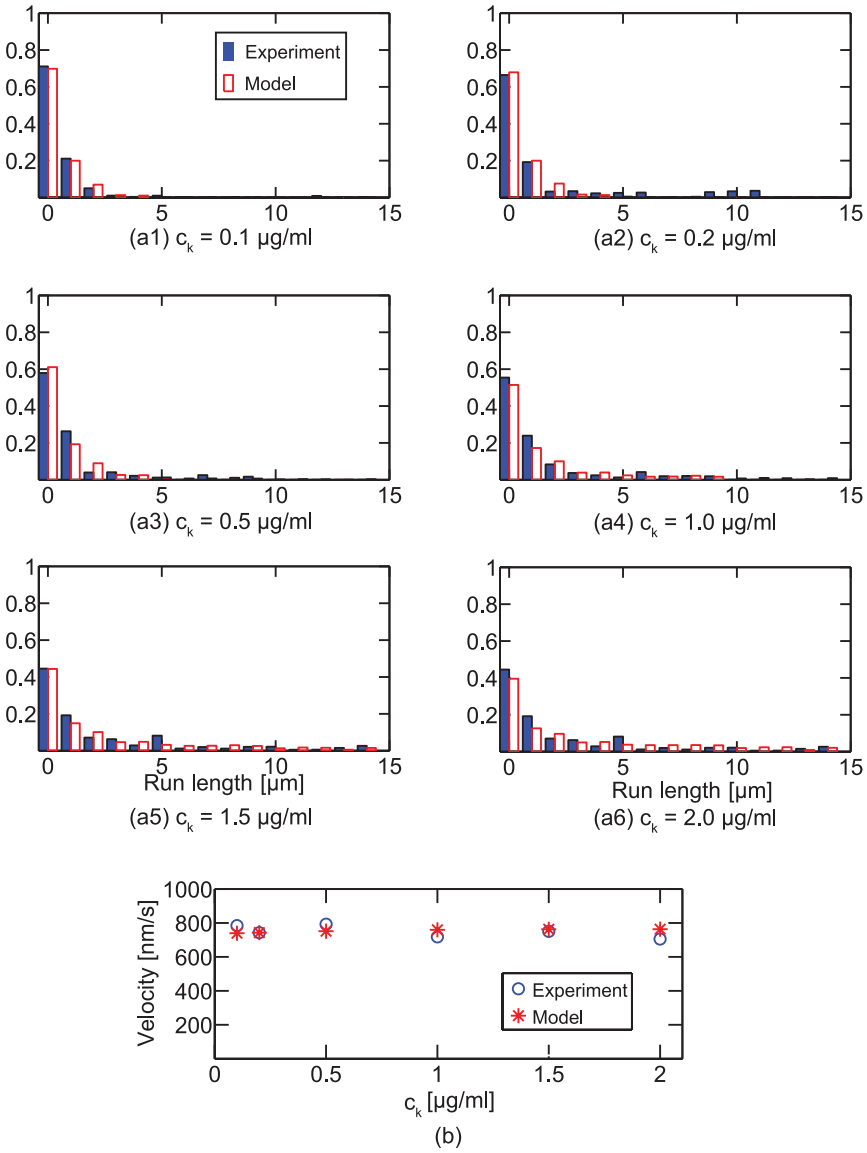

Figure 4.7: The run length distribution and mean velocity for various concentrations of kinesins. The experimental data obtained by Beeg, et al. [2] and the results calculated from the model are shown. All results are obtained in the absence of loads on the cargo. Whereas the run length increases with c_k, the velocity is almost constant for the shown concentrations.

tween 5 and 12 pN at [ATP] = 5 μM). Also, P_{D0} exponentially converges to 1 by Eq. (4.2) (e.g., for a load F_L of approximately 12 pN at [ATP] = 5 μM), as shown in Fig. 4.8 (b).

Note that P_{D1} is much higher than P_{D0} for a wide range of forces when the ATP con-

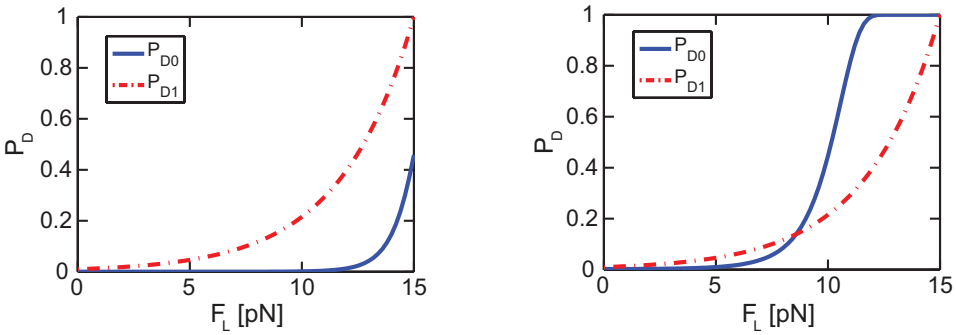

Figure 4.8: The unbinding probabilities for various resisting loads. The solid line denotes P_{D0}, and the dotted line shows P_{D1}. The unbinding probabilities for [ATP] = 2 mM (a) and 5 μM (b) are shown. Note that P_{D1} is much higher than P_{D0} in a wide range of loads for high [ATP].

centration is high. This difference suggests that most kinesin molecules unbind while in the state $[\mathrm{K.ATP} + \mathrm{MT}]_1$ if the ATP concentration is high enough (so that an ATP molecule binds to the kinesin head very fast). This rapid binding of ATP to the kinesin head decreases P_{D0} significantly. This characterization on the unbinding of kinesins predicts that kinesins mostly unbind when their free heads move to the next binding sites. If large resisting loads act on a kinesin, then the time required to complete one cycle of kinesin is very long. Thus, the interval between steps is also very long for the large loads. Consequently, the time until the unbinding of the kinesin occurs is very long when the load is large. This is a specific kinesin behavior which we refer to as highly loaded behavior (HLB) of kinesins. Because the leading kinesin undergoes the largest resisting force among kinesins, HLB is mostly likely to be observed in the leading kinesin. However, when the resisting load acting on the cargo is very large, then the next or second next leading kinesins also can exhibit HLB together with the first leading kinesin. The effects of HLB on the collective transport are described in the following.

4.5.2 Highly loaded behavior (HLB) of kinesins for robust intracellular transport: Ability to overcome obstacles

Transport by kinesins can be inhibited by other surrounding particles which act like obstacles. To consider the effect of cellular particles on the motion of the cargo, static and moving obstacles are modeled in this chapter. First, a static obstacle is located ahead of the cargo, as shown in Fig. 4.9 (a). When the cargo confronts a static obstacle, the cargo is assumed stuck to the static obstacle until the sum of the forces generated by kinesins exceeds a force $F_{\rm obs}$ which is required to overcome the obstacle. Second, the obstacle is assumed to move backward, toward the minus-end of the MTs. This motion pushes the cargo backward with a velocity $V_{\rm obs}$, as shown in Fig. 4.9 (b). The retrograde motion due to the moving obstacles also vanishes when the sum of the forces generated by kinesins exceeds a force $F_{\rm obs}$.

To check the role of HLB in overcoming obstacles, three virtual motors are created to compare their abilities of overcome obstacles with that of kinesin. The virtual motors are designed by modifying properties of kinesin which are necessary for HLB. First, the virtual motor 1 is modeled so that the unbinding probabilities for three states (i.e., [K+MT], $[\mathrm{K.ATP} + \mathrm{MT}]_1$ and $[\mathrm{K.ATP} + \mathrm{MT}]_2$) are the same. To apply this modification, the unbinding probabilities corresponding to the current force on the kinesin are added together. Then, that summation is divided by three and assigned to the current state so that the motor has equal unbinding probabilities for those three states. Second, the virtual motor 2 has a stepping frequency which is invariant over forces acting on the motor. This modification is accomplished by removing the dependency of the chemical reactions on forces. Third, the virtual motor 3 has both of the changes of virtual motors 1 and 2. Note that the unbinding probability (of a single molecule) per step is the same for all motors, virtual and actual. However, the responses of the teams composed of each type of motors in the presence of

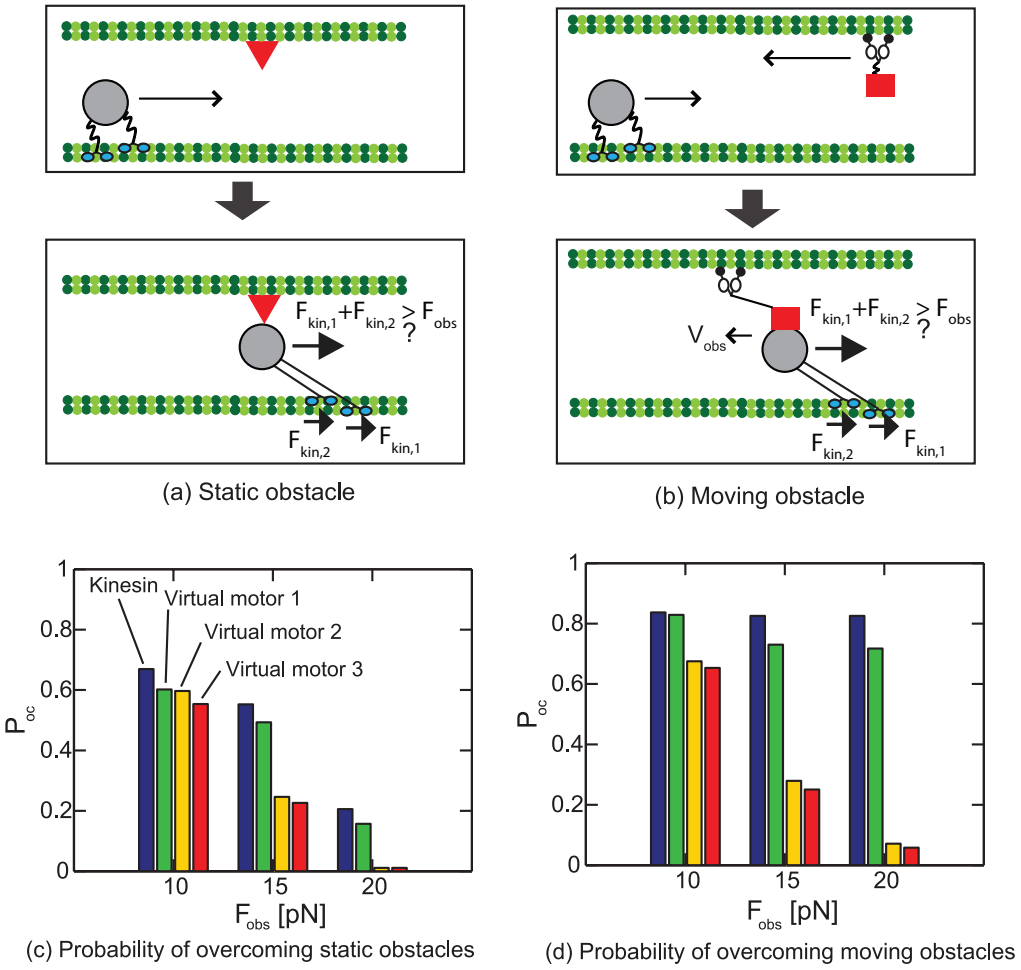

Figure 4.9: The transport of the cargo in the presence of obstacle. (a) depicts transport when a static obstacle (shown as a triangle) is on the path of the cargo. (b) shows a moving obstacle (shown as a rectangle) approaching the cargo. The cargo moves backward with velocity of $v_{\rm obs}$ due to the moving obstacle. $F_{\rm kin,1}$ and $F_{\rm kin,2}$ are forces (acting on the cargo) of two kinesins. The cargo overcomes the obstacle when the sum of those two forces is larger than $F_{\rm obs}$. (c) and (d) present the probability P_{oc} that the cargo overcomes one obstacle without unbinding from the MT. (c) shows the probabilities for static obstacles which require forces of 10, 15, and 20 pN to be overcome it. (d) shows probabilities to overcome moving obstacles when the cargo is retrograded by the obstacles with the velocity of 200 nm/s.

obstacle are considerably distinct. The team of two actual kinesins show higher probability P_{oc} of overcoming one obstacle without dissociating from the MT compared to other

teams, as shown in Fig. 4.9. The difference is remarkable for the team of virtual motors 2. This suggests that the low stepping frequency for high loads is the primary reason for the HLB of kinesin. In addition, if a team of motors confront n-obstacles, the overcoming probability decreases to P_{oc}^{n}. Then, the cargo transported by virtual motors is not able to reach the final destination, while actual kinesins can resist the interruption of obstacles by using their HLB.

4.5.3 Run length of transport by several kinesins

To obtain run lengths for teams of kinesins, both unbinding and rebinding are considered together with the mechanistic model. At the beginning of the transport, only one kinesin is bound to the MT, and every other kinesin is unbound. Each transport is assumed to be terminated when all kinesins detach from the MT. The run length is defined as the difference in the position of the cargo at the beginning and the position at the termination of the transport. To minimize the error from Monte Carlo simulation, a large number of data is obtained for each load and number of kinesins in the team. The average of the run length over the number of used data converges at about 100 to 150 sets of data. The results presented were obtained using 200 sets to calculate average values. When several kinesins are involved in the transport, the run length of the team increases with the number of kinesins in the team, as shown in Fig. 4.10 (a). The run length of single kinesins monotonically decreases with the load. However, the run length of a team of kinesins increases with the load when the load is larger than 8 pN.

This interesting feature can be explained by the HLB of kinesins, as shown in Fig. 4.10 (b). HLB is attributed to properties of the unbinding and stepping frequency. Kinesins mostly unbind when the free heads move to the next binding site. Thus, the unbinding probability for a given time interval increases as the kinesin takes more steps in a given time interval.

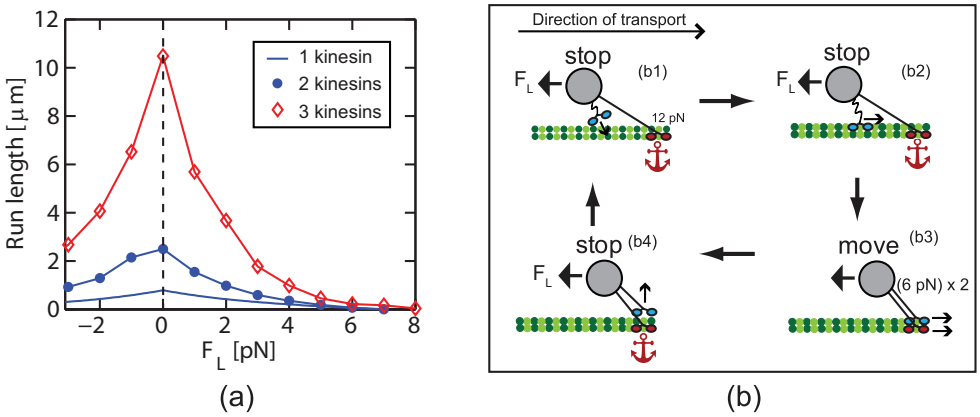

Figure 4.10: The run length of transport by several kinesins. (a) shows the run length of one, two, and three kinesins for [ATP] = 2 mM. (b) shows an example of HLB when a large resisting load acts on the cargo. (b1) The leading kinesin is stationary while waiting for ATP. During this long interval, another kinesin binds to the MT. (b2) It is likely that the distance between the newly bound kinesin and the cargo is less than the length of the cargo linker. Thus, the newly bound kinesin does not have a load. Consequently, the lagging kinesin walks toward the leading one (the anchor) with high velocity. (b3) The two kinesins cooperate to transport their cargo against the large load. (b4) One of the kinesins unbinds and the other kinesin acts as an anchor again.

The stepping frequency of kinesins is decreased by resisting loads. As a consequence, when the high resisting force acts on a kinesin, the kinesin walks slowly and remains bound on the MT for a long time, like an anchor. During this long time, other unbound kinesins attached to the same cargo have time to bind to the MT, as shown in Fig. 4.10 (b). It is unlikely that large resisting loads, larger than 8 pN, continuously acts on the cargo in cells. However, this HLB can be used in cells to make the transport more robust. Also, we note that the run length will decrease for loads F_L close to $F_L = 7 \times n$ [pN], where n is the number of kinesins attached to the cargo. For those large loads, the cargo will move backward because the kinesins walk backward with high probability when a resisting load close to 7 pN is applied to a single kinesin.

4.5.4 Velocity of transport by several kinesins

In the absence of load, a single kinesin moves with a velocity of about 800 $\mathrm{nm/s}$ [22, 28, 29, 111]. The velocity of the transport performed by several kinesins was predicted in this chapter. For moderate resisting loads, the transport is realized with slower velocity compared to the motion of single kinesins. While the velocity of single kinesins reach a maximum around 800 $\mathrm{nm/s}$ at small loads, the motion of a team of kinesins is accelerated by assisting loads, as shown in Fig. 4.11 (a).

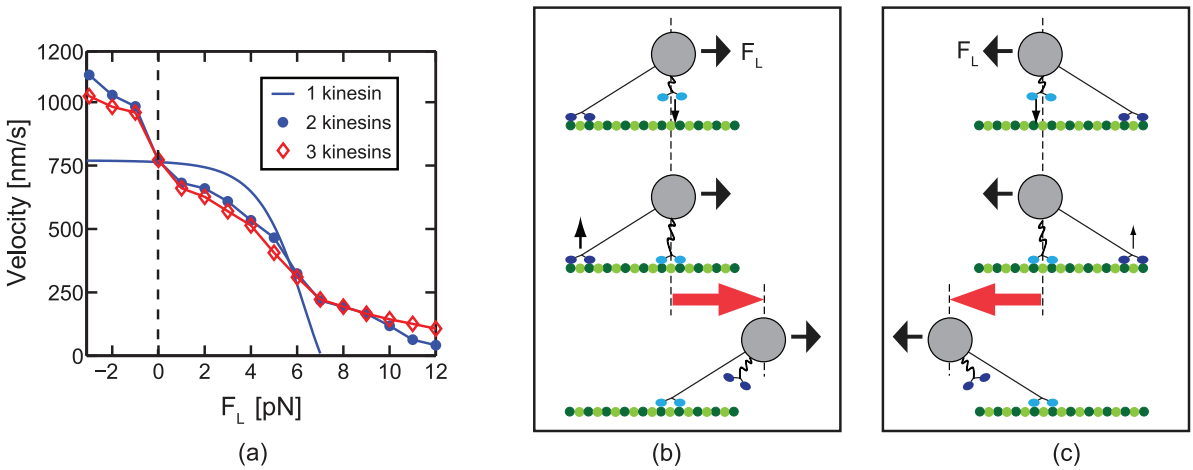

Figure 4.11: The transport velocity by teams of kinesins. (a) is the transport velocity by one, two, and three kinesins for [ATP] = 2 mM. (b) and (c) show the effect of the binding and unbinding on the motion of the cargo when the assisting or resisting load is acted on the cargo.

The motion of collective transport can be decelerated or accelerated by binding and unbinding of kinesins. When an assisting load acts on the cargo, the unbound kinesin is likely to bind to a binding site located in front of the other, already bound kinesin as shown in Fig. 4.11 (b). Consequently, the cargo moves forward a distance longer than just 8 nm (one kinesin step). Hence, the velocity of the cargo increases beyond that of a single kinesin, as shown in Fig. 4.11 (a). This behavior contrasts single molecule experiments at

high ATP concentrations where the velocity is not increased by assisting loads. Also, resisting loads (less than 6 pN) decrease the transport velocity. That is because, for resisting loads, the unbound kinesin rebinds with high probability behind the other, already bound kinesin as shown in Fig. 4.11 (c). Thus, the transport is decelerated by resisting loads less than 6 pN, as shown in Fig. 4.11 (a). The velocities for resisting loads higher than 7 pN are larger than the single kinesin velocity. This difference is due to the degree of cooperative work of kinesins for various loads [105]. Due to the slack behavior of kinesins, some bound kinesins in a team do not generate forces for transport if the load is small. However, a team is predicted to work in a cooperative fashion for high resisting loads.

4.6 Conclusions

When several kinesins are involved in a transport, the characteristics of the transport are significantly affected by the unbinding and rebinding of the kinesins. Novel methods to predict the probability to rebind were presented to reduce the computational effort dramatically. Particularly, the conversion from time average to spatial integration is the key advantage. Note that this approach can be used for other systems which have properties fluctuating with high frequencies. This method revealed that the instant of rebinding depends very weakly on the load. The changes of the run length and of velocity over the load are different for a single kinesin and for a team of kinesins.

The possibility of transport against resisting loads larger than 7 pN per motor implies that the capabilities of a single kinesin can be enhanced by teams of kinesins. To transport a cargo in cells, the cargo needs to navigate in highly viscoelastic cytoplasm which is filled with several many molecules [80, 81, 92]. A single kinesin is not reliable to perform that task for at least two reasons. First, when the resisting load is higher than 7 pN, processivity of single kinesins is not guaranteed because its backward motion occurs frequently. Sec-

ond, the observed distribution of the run length [17, 30, 56, 99, 112] indicates that most of single kinesins detach from the MT before they reach 1 μm. However, a group of kinesins shows comparable velocity toward the plus-end of the MT for a broad range of loads.

The velocity of collective transport has three noticeable characteristics compared to the velocity of single kinesins. First, the cargo of several kinesins moves faster than the cargo transported by a single kinesin for assisting loads and slower for resisting loads less than 6 pN. Second, the increase in transport velocity due to assisting loads is larger than the decrease due to resisting loads. Third, the magnitude of the changes in velocity is similar for two and three kinesins. Although the cargo of three kinesins experiences more frequent binding and unbinding events, the distances of the anterograde and retrograde motion of the cargo indicated by red arrows in Figs. 4.11 (b) and 4.11 (c) are shorter for three kinesins. These characteristics are also observed in previous experiments. Dujovne et al. [113] applied external forces on MTs in their inverted gliding assay by using an electric field. In their experiments, the velocity increases or decreases due to assisting or resisting loads. Also, the change in the velocity is larger for assisting loads, like our results. The low and medium density of kinesin shows a similar velocity change over the electric field. This is also consistent with the velocity predictions in this chapter.

The team operation of kinesins also prevents the early termination of the transport by obstacles in cells. The interference between the cargo and the obstacles can result in significant loads on the cargo. Especially in axons where several MTs are aligned, the motion of the cargo can be affected by static obstacles such as MT associated proteins, or tangles of the proteins [114]. Also, the cargo could encounter other cargoes transported by different motor proteins such as dyneins which move reverse to the walking direction of kinesin. The cargoes transported toward the minus-end of MTs act as moving obstacles to the anterograde transport of kinesins. The huge load resulting from the static and moving

obstacles is fatal to the transport if the cargo is transported by a single kinesin. However, if several kinesins are attached to the cargo, one or more kinesins function as temporary anchors until the transient load vanishes. Thus, kinesins are able to continue and complete their task as a team. The comparison of transport by actual kinesins and virtual motors suggests that the reduction in velocity of kinesins for high resisting loads is necessary to maintain cellular transport in the presence of obstacles. When the motion of the cargo is blocked by obstacles, the leading kinesin acts like an anchor as its velocity decreases. Thus, time is available for the other kinesins in the team to cooperate and overcome the interruption due to the obstacle. Together with the velocity of the transport by several kinesins, the HLB suggests that cells utilize teams of kinesins for the (harsh) cellular transport.

CHAPTER V

Metrics for characterizing the collective transport by multiple kinesins

5.1 Summary

The collective transport is complex because the stochastic motion of the kinesins attached to the same cargo affect each other. To characterize the coupled motion of kinesins, several metrics are proposed in this chapter. One interesting feature revealed from the metrics is that the kinesins move independently when the resisting load acting on the cargo is small. However, the kinesins are more likely to to walk in a cooperative manner where the load increases.

5.2 Background and motivation

Several *in vivo* experiments have discovered evidence of collective transport of vesicle by multiple kinesins [115, 116]. However, the effects of the coordination of multiple kinesins on the velocity remains controversial [52, 53, 117, 118]. Shubeita et al. [117] observed droplets pulled by kinesin in Drosophila embryos. The number of kinesins did not raise the transport velocity in their experiments compared to single molecule measurements. In the experiments of peroxisome with kinesins and dyneins [52], the cargo moved to the plus-end of the MTs 10 times faster than the *in vitro* single molecular motion. An-

other coordinated transport of kinesins is also found in the extraction of membrane tubes along MTs. Leduc et al. [108] assume that kinesins pull membrane tubes around the tips of tubes, where kinesins bound on other parts of tubes exert no force on the tubes. Thus, they were able to obtain the binding rate of kinesins to MTs by measuring the velocities of the tubes.

Various mathematical models have been developed to analyze the dynamics of the collective transport of kinesins. The stochastic model of Leibler et al. [119] predicts the nonlinear relation between the speed of the cargo and the number of kinesins. When the number of kinesins is less than 2, the velocity linearly increases with the number of kinesins. However, the velocity saturates at a specific number of kinesins. Shtridelman et al. [81] proposed a shared-load model to obtain the transport velocity when there are multiple kinesins. Their model is able to calculate the average velocity of the collective transport. They also considered the effect of the viscosity of the fluid. Their main assumption is that kinesins equally share the load applied to the cargo. In addition, their model neglects changes in the number of kinesins bound to the MT during the transport. Klumpp et al. [42] modeled the number of kinesins using a Markov chain and obtained the stationary solution of states in the chain. Although the probabilities of the number of kinesins and the corresponding transport velocity are calculated through this mean-field model, their model also assumes that loads are uniformly distributed over kinesins. However, the load can be unequally distributed over kinesins in actual transport. Thus, other several models focused on the effect of stochastically fluctuating loads on kinesins have been proposed. Jülicher et al. [120] proposed a stochastic model for multiple kinesins. Their model assumes that each kinesin has two states. They considered fluctuating forces and fluctuating potentials of each state. The mechanistic model of Hendricks et al. [51] is able to describe the stochastic chemical reaction in kinesin heads and captures the depen-

dence of the chemical reaction rate on the fluctuating loads on kinesins. Thus, their model also allows predicting the collective dynamics of kinesins. Berger et al. [121] calculated theoretically the transport velocity done by two coupled kinesins to clarify the effect of coupling. They argued that the effects of coupling are determined by the ratio of the force induced by coupling, the stall force and the detachment force. Their model predicts that the effects of coupling on the collective transport are different for various kinds of molecular kinesins. Bouzat et al. [122] studied theoretically the effects of the number of tracks in collective transport. Their results suggest that transport characteristics such as velocity and run length change over the number of kinesins in a single track, but the changes decrease when multiple tracks are allowed.

Collective transport involves coupled stochastic processes of molecular kinesins. The goal of this chapter is to introduce metrics to characterize this stochastic dynamics. First, the modal amplitude fluctuation is used to observe the degree of synchronization between kinesins. The value of modal amplitude fluctuation is calculated by using the states of kinesins collected over many time intervals. Although modal amplitude fluctuation does not have the usual physical meaning of normal modes, a specialized variant of modal analysis allows this quantity to represent the degree of synchronization in the motion of a group of kinesins. This metric originates from the energy analysis proposed by Hendricks et al. [51]. They defined and calculated the degree of synchronization between kinesins during a long time interval with one single value of modal amplitude fluctuation. Their metric is extended in this chapter so that it can properly capture the changes in the synchronization over time.

When two kinesins transport a cargo, the difference in the number of steps of each kinesin is defined as D_c. This quantity can be used to observe the relative motion between the two kinesins. Zhang et al. [123] computed D_c in the absence of slack in the cargo

linkers. Differently from their model, the nonzero unstretched length of the cargo linker is accounted for in this chapter. In addition, the standard deviation of D_c of two coupled kinesins is obtained to capture the effect of coupling via cargo linkers. However, D_c contains not only the effect of coupling via cargo linkers, but also the stochasticity of the chemical reactions of kinesins. Thus, this quantity was compared to the difference in the number of steps of two uncoupled kinesins.

The transport executed by two kinesins can be of two types. One is a transport where the two kinesins pull the cargo together/simultaneously (cooperative transport). The other type is a slack transport where sometimes one kinesin carries the entire load while the other experiences no load or an assisting load, and other times the roles of the two kinesins are reversed. In the slack transport, the cargo linker of one kinesin (sometimes one, sometimes the other) is slack or exerts resisting forces on the cargo. Although D_c is an effective metric to characterize the relative motion between kinesins, it is not a direct metric to discern the type of transport. Also, when the kinesins are not identical, it becomes more complicated to infer from D_c the load distribution among kinesins. Thus, the difference in the forces on each kinesin (D_F) is defined as a metric in this chapter. Also, the slackness is defined and calculated to capture the dominant type of transport. In this chapter, cooperativity relates to how equally kinesins share the load. As the load is more fairly distributed over the kinesins, the cooperativity improves. Thus, the standard deviation of D_F is also computed to characterize the degree of cooperation during collective transport. This perspective is most useful when studying identical dimeric motors which transport a cargo (and the cargo deformation due to the load is negligible). This correlation between D_F and cooperativity has limited usefulness if the cargo is soft and pulled by monomeric kinesins. In those cases, higher cooperativity can be achieved by asymmetric distribution of the load [124].

Some of the chemical energy from ATP hydrolysis is lost when the chemical energy

is transformed into mechanical work. This energy is dissipated by the fluid where the transport takes place. Most previous research has focused on the efficiency of kinesin by comparing the chemical energy and the work done by the kinesin molecule. In this chapter, the energy loss (or the power loss) in the fluid is computed instead of the efficiency. This quantity offers two valuable clues about the dynamics of collective transport. First, the power loss reflects the effectiveness of the transport. Second, the power loss provides a metric for the degree of smoothness in the motion of the cargo.

5.3 Metrics for characterizing collective dynamics

While the movement of a single kinesin is mainly influenced by the external load and the concentration of ATP, kinesins which participate in collective transport have more complicated motion due to the interaction between kinesins. The modal amplitude fluctuation, D_c, D_F, and the power loss are developed to analyze the dynamics of collective transport.

5.3.1 Modal amplitude fluctuation

To find the correlation among the motions of kinesins, the modal amplitude fluctuation is calculated through a variant of modal analysis. The modal amplitude fluctuation is denoted by A and is defined as the time average of quadratic value of the states as

$$A = \frac{1}{T}\int_0^T \frac{1}{2}\mathbf{x}^T(t)\mathbf{x}(t)dt, \tag{5.1}$$

where $\mathbf{x}$ is the vector which contains the states of the system. For the multiple kinesin system, the positions of all kinesin heads are chosen as the components of the state vector for the system. The position of the neck and the chemical state variable are not included because they yield less clear results of the correlation among the motions of the kinesins. This modal analysis requires two modal amplitude fluctuation values, A_T and A_S. A_T is the total amplitude fluctuation calculated from the states whose drift mode and mean value

are removed. The states projected onto a certain mode are used for the calculation of A_S. The ratio between these two modal amplitude fluctuation values indicates the degree to which the motion is in that mode. In this research, the synchronous modes are used to acquire the degree of synchronized motion among the kinesins. The procedure starts with the construction of a matrix which contains discrete states, namely

$$[\mathbf{X}] = \begin{bmatrix} \bar{x}_1(t_i) & \bar{x}_1(t_{i+1}) & \dots & \bar{x}_1(t_f) \\ \bar{x}_2(t_i) & \bar{x}_2(t_{i+1}) & \dots & \bar{x}_1(t_f) \\ \vdots & \vdots & \ddots & \vdots \\ \bar{x}_M(t_i) & \bar{x}_M(t_{i+1}) & \dots & \bar{x}_M(t_f) \end{bmatrix}, \tag{5.2}$$

where $\bar{x}_k(t_j) = [x_{hd1,k}(t_j)\, x_{hd2,k}(t_j)]^T$ denotes the state of *k*-th kinesin at time t_j and $x_{hd1,k}$ and $x_{hd2,k}$ represent the position of two heads of the *k*-th kinesin. The state matrix, $[\mathbf{X}]$, includes states between time instances t_i and t_f. The degree of synchronization between kinesins (namely zero phase difference) is first observed using zero shifted states. In addition, nonzero shifted states are used to capture constant but non-zero phase differences. Thus, each state is shifted in time by τ_k with respect to the first kinesin as follows

$$[\mathbf{X}] = \begin{bmatrix} \bar{x}_1(t_i) & \bar{x}_1(t_{i+1}) & \dots & \bar{x}_1(t_f) \\ \bar{x}_2(t_i+\tau_1) & \bar{x}_2(t_{i+1}+\tau_1) & \dots & \bar{x}_1(t_f+\tau_1) \\ \vdots & \vdots & \ddots & \vdots \\ \bar{x}_M(t_i+\tau_{M-1}) & \bar{x}_M(t_{i+1}+\tau_{M-1}) & \dots & \bar{x}_M(t_f+\tau_{M-1}) \end{bmatrix}. \tag{5.3}$$

Before calculating the modal amplitude fluctuation, the original coordinates have to be translated to the frame that moves with the average velocity of the system. To perform this transformation, a mode shape of the drift is defined as

$$\mathbf{d} = \begin{bmatrix} 1 & 1 & \dots & 1 \end{bmatrix}^T. \tag{5.4}$$

The components of the dynamics associated with the drift and the mean are then subtracted as

$$\mathbf{x}'_j = \mathbf{x}_j - \frac{\mathbf{d}^T\mathbf{x}_j}{\mathbf{d}^T\mathbf{d}}\mathbf{d}, \tag{5.5}$$

$$\tilde{\mathbf{x}}_j = \mathbf{x}'_j - < \mathbf{x}'_j > . \tag{5.6}$$

The modal amplitude fluctuation with removed drift and mean is calculated for the time interval $[t_i,\ t_f]$ as

$$A_T = \frac{1}{t_f - t_i}\sum_{j=i}^{f}\frac{1}{2}\tilde{\mathbf{x}}_j^T(t)\tilde{\mathbf{x}}_j(t)(t_{j+1} - t_j). \tag{5.7}$$

Next, the mode shape of synchronous motion for one kinesin is defined as

$$\bar{s} = \begin{bmatrix} 1 & -1 \end{bmatrix}^T. \tag{5.8}$$

The synchronous mode shapes for multiple kinesins are created based on this mode shape. The two heads of kinesin and their motions are assumed to be identical. Thus, there are two synchronous mode shapes for the system of two kinesins as

$$\begin{aligned} \mathbf{s}_1 &= \begin{bmatrix} 1 & -1 & 1 & -1 \end{bmatrix}^T, \\ \mathbf{s}_2 &= \begin{bmatrix} 1 & -1 & -1 & 1 \end{bmatrix}^T. \end{aligned} \tag{5.9}$$

The projection of $\tilde{\mathbf{x}}_j$ along the m^{th} synchronous mode is

$$\tilde{\mathbf{x}}^{||}_{j,m} = \frac{\mathbf{s}_m^T\tilde{\mathbf{x}}_j}{\mathbf{s}_m^T\mathbf{s}_m}\mathbf{s}_m. \tag{5.10}$$

Finally, the modal amplitude fluctuation along all the synchronous modes is calculated for the time interval $[t_i,\ t_f]$ as

$$A_S = \frac{1}{t_f - t_i}\sum_{j=1}^{f}\Big[\sum_{m=1}^{M}\frac{1}{2}[\tilde{\mathbf{x}}^{||}_{j,m}]^T[\tilde{\mathbf{x}}^{||}_{j,m}]\Big](t_{j+1} - t_j), \tag{5.11}$$

where M is the total number of possible synchronized modes. The degree of synchronization between kinesins is given by the ratio of A_T and A_S. A quadratic form of states is

used to compute the modal amplitude fluctuation. However, the concept of synchronization is usually related to the states of the kinesins themselves (instead of the quadratic of the states). Thus, the square root of the ratio of A_S and A_T is denoted by A_R and is used to observe the degree of synchronization. A_R is defined as

$$A_R = \sqrt{\frac{A_S}{A_T}}. \tag{5.12}$$

A high value of A_R indicates that the kinesins move in a highly synchronized fashion. The interval of integration is referred to as the window. The size of this window, $[t_i,\ t_f]$, is determined so that a window contains 10 steps of each kinesin. Several, possibly overlapping, windows are used to observe the characteristics of the dynamics as follows

$$[t_1,\ t_1 + \Delta T]_{\text{window 1}},\ [t_1 + \Delta t,\ t_1 + \Delta t + \Delta T]_{\text{window 2}}, ..., \tag{5.13}$$

where ΔT is the size of each window and $\Delta t\ (= t_f - t_i)$ denotes the time interval between adjacent windows. With this method, the degree of synchronizations of time windows of a size of approximately 10 steps is obtained over time. Both the value of A_R without shift and with shift are computed in this chapter. The range of the shift is limited to the longest dwell time in each window. The value of A_R varies over the shift. Its maximum value in each window is used in this work.

5.3.2 Difference in the number of steps of kinesins

When two kinesin kinesins transport a cargo, the difference in the number of steps of each kinesin is defined as D_c ($D_c = n_{mt,1} - n_{mt,2}$, where $n_{mt,i}$ is the number of steps of the i^{th} kinesin, and $n_{mt,i}$ is counted from the instant when the loads on each kinesin are the same). This quantity is used to observe the relative motion between the two kinesins. The subscript c indicates that the two kinesins are coupled (they transport a cargo together).

In addition, the standard deviation of D_c for the two coupled kinesins is observed.

Large values of the standard deviation indicate that the two kinesins move in an unbalanced fashion (i.e., they are unequally loaded). At times a kinesin is more loaded than the other, and at other times the kinesin is less loaded. Lower values of the standard deviation are obtained when the motion of one kinesin strongly depends on the other. However, D_c contains both the effects of coupling via the cargo linker and the inherent stochastic dwell time of kinesin. Thus, to understand the dynamics of the cooperativity better (and apart from the stochasticity), the values of the standard deviation are normalized by the standard deviation of D_{uc}, where D_{uc} denotes the difference in the number of steps of each kinesin for two uncoupled kinesins (i.e., when each kinesin transports its own cargo independently).

5.3.3 Difference in the forces on each kinesin

Due to the stochasticity of the dwell time, kinesins in a collective transport share the load, and the load on each kinesin change continuously. To characterize the load distribution among kinesins, D_F is introduced. When two kinesins transport a common cargo, D_F can be defined as

$$D_F = \frac{1}{2}(F_{\text{kin},1} - F_{\text{kin},2}). \tag{5.14}$$

The slack transport is revealed by the absolute value of D_F. If that value is larger or equal to the load per kinesin, then the transport is slack. For cooperative transport, the absolute value of D_F is less than the load per kinesin. From a statistical perspective, the probability of D_F can be used to identify the dominant type of transport. When one kinesin is likely to carry the entire load (sometimes one kinesin, sometimes the other), the probability of D_F has two peaks (at plus and minus the load per kinesin). If the transport is cooperative (i.e., kinesins share the load), the probability has only one peak close to a D_F of zero. As the cooperativity increases, the probability of D_F has a sharper peak. Thus, the standard

deviation of D_F represents the inverse of cooperativity.

Loss of power by drag

Instead of comparing the consumed chemical energy and the work done by the kinesins, the dissipating power during the transport of the cargo is calculated. The loss of power is obtained using the drag force and the velocity. The drag force is determined by the following relation between forces exerted on the cargo

$$F_D(t) + F_L(t) = \sum_{i=1}^{N} F_{\text{kin},i}(t), \tag{5.15}$$

where F_D is the drag force, and F_L is the external load on the cargo. The average loss of power over the given interval $[t_i,\ t_f]$ is

$$P_{loss} = \frac{1}{t_f - t_i} \int_{t_i}^{t_f} F_D(t) v(t) dt, \tag{5.16}$$

where v is the velocity of the cargo. The objective of this analysis is to observe efficiency and smoothness of the cargo motion simultaneously. The lack of smoothness is in part due to the significantly fast stepping motion of kinesins and the relatively long time for their chemical reactions. Thus, the velocity of the cargo changes rapidly over time. These rapid changes are affected by the level of viscosity. They are also affected by the number of kinesins. Thus, the amount of wasted power changes over the number of kinesins even when the cargo moves with the same average velocity. Among the possible types of transport with the same average velocity, a transport with a lower power loss has a smoother motion than other types of transport. Note that segments of transport time histories which have the same average velocity are compared to use the power loss as a measurement of the smoothness of the motion.

Smooth motion is preferable from the perspective of energy efficiency. However, less smooth motion can be beneficial for high speed. The average stresses on each kinesin

depend on the smoothness of the motion. While the smooth motion causes the leading kinesin to remain in a highly deformed state, a high stress on the lagging kinesin reduces by the smoothness of the motion. As a result, the motion is smoother when the leading kinesin slows down and the lagging kinesin accelerates. If a molecular kinesin has a linear dependence of its speed on the load, then the effects of smoothness are not remarkable. However, since kinesin has a nonlinear force-velocity curve, the deceleration that enhances the smooth motion can be large for some range of loads. Consequently, the smooth motion slows down the transport.

5.4 Results

The collective dynamics of kinesin depends on the external load, the number of kinesins, and the stiffness of the cargo linker. Their effects are characterized using A_R, D_c, D_F and the power loss.

5.4.1 Modal amplitude fluctuation

A_R is used to observe the effects of the external loads and the stiffness of the cargo linker on the degree of synchronization between kinesins. Although their motions are not perfectly synchronized due to the stochasticity of the transport, A_R increases over the load, as shown in Fig. 5.1 (a)-(c). This behavior suggests that the kinesins tend to be more synchronized where the external load is larger. This feature is consistent with the result in [51]. In addition, changes in A_R over time show another behavior of collective dynamics. The standard deviation of A_R is calculated to measure the fluctuation of A_R over time (Fig. 5.1 (d)). The degree of synchronization changes over time. That change is larger when the cargo experiences a small load because stochastic processes dominate the dynamics. Thus, A_R has low values, and its fluctuation is large. However, a large load decreases the effects of the stochastic processes on the dynamics. As a result, A_R exhibits

only small fluctuations over the windows where a large load is applied. For medium loads, the standard deviation of A_R is larger than that for small and large loads. A possible explanation is that the kinesins tend to become synchronized by the load, but stochastic processes interfere with the synchronized motion. This phenomenon repeats over time.

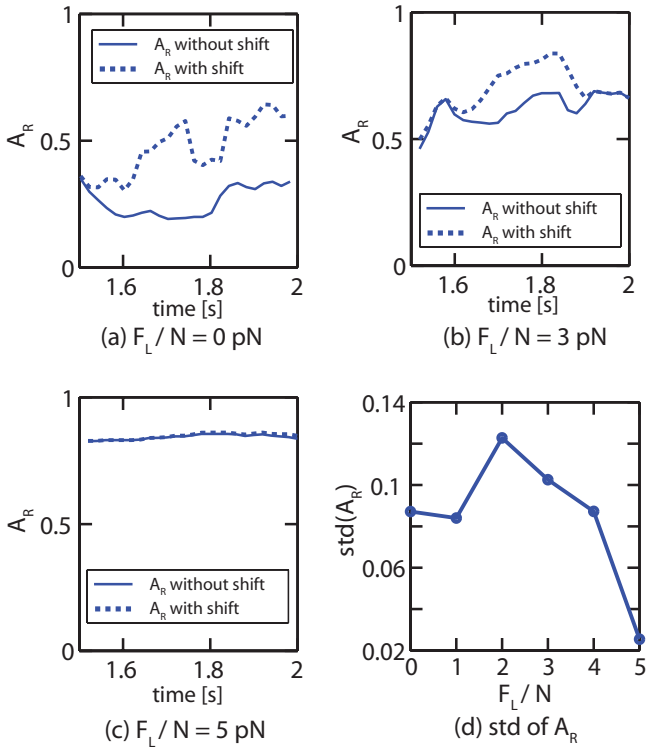

Figure 5.1: Fluctuations of the degree of synchronization A_R over time for various loads. (a), (b), and (c) show A_R values over time for loads per kinesin of 0, 3, and 5 pN, respectively. The stiffness K_c of the cargo linker is 0.125 $\mathrm{pN/nm}$. Solid lines show A_R of the original states, and dotted lines show A_R with shifted states. (d) shows the values of the standard deviation (std) of A_R for various loads per kinesin.

Another interesting feature is that A_R for small loads increases if shifted states are used. The shifted states are used to identify when synchronization is at a non-zero phase difference between the motion of the kinesins. For example, if a constant phase difference

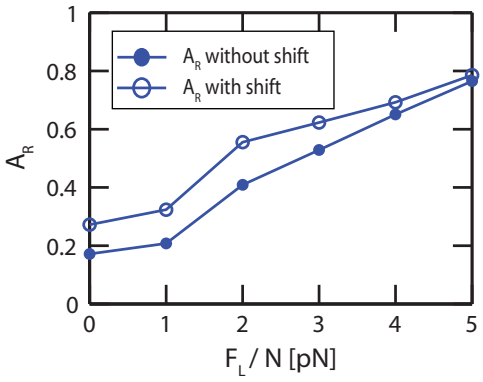

Figure 5.2: Average values of the degree of synchronization A_R for various loads per kinesin. The stiffness K_c of the cargo linker is 0.125 $\mathrm{pN/nm}$. Average values of A_R and values with shifted states are plotted. For small loads, A_R increases by shifting the states of the kinesins, indicating a phase-locked dynamics. For large loads, the effect of the shifting is negligible, indicating synchronization (at zero phase difference).

is present between the motion of two kinesins (in a time window), then the shifted states of one kinesin are synchronized with the regular (not shifted) states of the other kinesin. As the load increases, the A_R does not increase even with shifted states, as shown in Fig. 5.2. This behavior indicates that large loads make the group of kinesins move in a fashion which has the maximum degree of synchronization (in that given stochastic situation).

The cargo linkers play an important role in the collective transport because the coupling among the kinesins is affected by the cargo linkers. When one kinesin walks faster than other kinesins, its cargo linker is stretched more. The kinesin then experiences a larger force which is proportional to the stretching length and the stiffness of the cargo linker. This increased force slows down the leading kinesin. Hence, the cargo linkers not only connect kinesins and the cargo, but they also couple the motions of kinesins. Thus, highly stiff cargo linkers result in strong coupling between kinesins. The values of A_R for various stiffnesses of cargo linkers shown in Fig. 5.3 indicate that the large stiffness causes

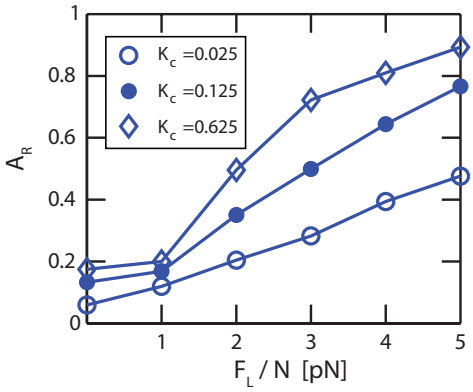

Figure 5.3: Average value of the degree of synchronization A_R vs. load per kinesin for values of the stiffness K_c of the cargo linker of 0.025, 0.125 and 0.625 $\mathrm{pN/nm}$.

synchronized motion.

5.4.2 Difference in the number of Steps

Since the two kinesins are considered identical, the probability distributions of D_c are symmetrical about zero. Interestingly, the probability distributions of D_c become wider as the load decreases, as shown in Fig. 5.4 (a)-(c). The values of the standard deviation of D_c which are normalized by the standard deviation of D_{uc} were calculated for various loads. The results are shown in Fig. 5.4 (d). If the normalized standard deviation of D_c is 1, the coupling via cargo linkers does not have any effect and the two kinesins move independently. Small values of the normalized standard deviation of D_c indicate that the motions of the two kinesins are correlated (restricted by each other). Also, the normalized standard deviation of D_c decrease over the loads. This suggests that the two kinesins share the load more fairly when the load is larger.

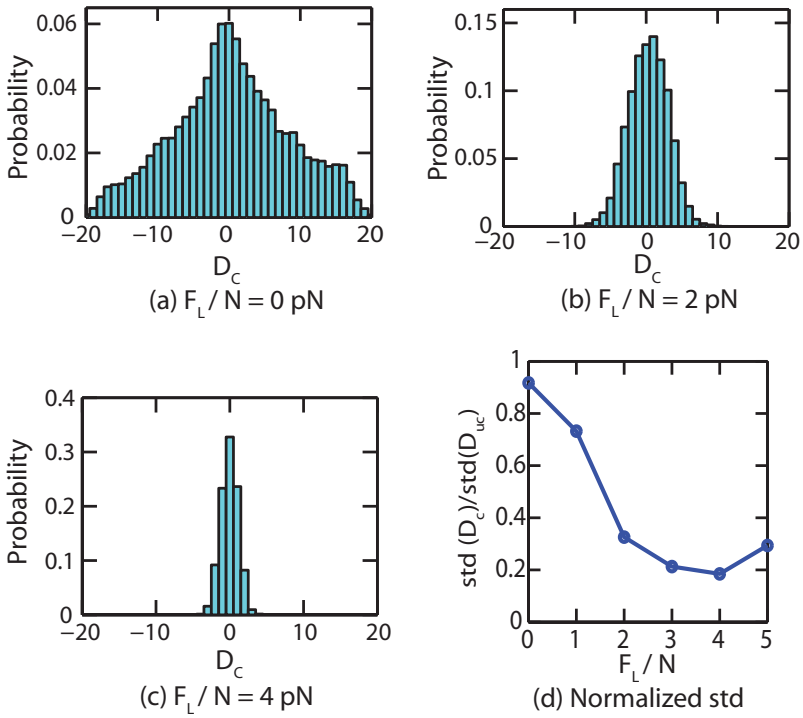

Figure 5.4: Difference D_c in the number of steps of two coupled kinesins for various loads per kinesin. (a), (b), and (c) show probabilities of D_c for loads per kinesin of 0, 2 and 4 pN. The stiffness K_c of the cargo linker is 0.125 $\mathrm{pN/nm}$. (d) shows the normalized standard deviation (std) of D_c vs. load per kinesin.

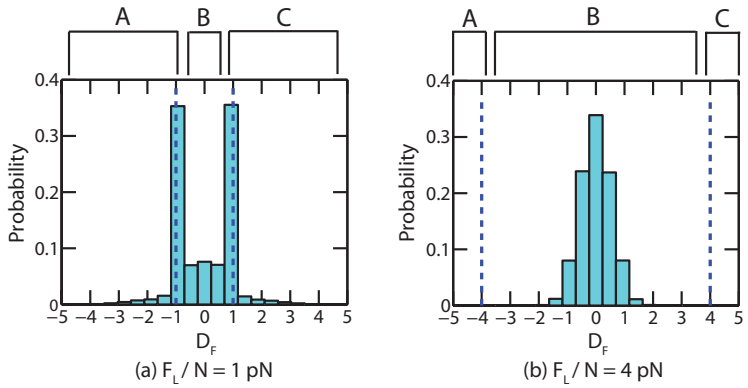

Figure 5.5: Probability of the difference D_F in forces acting on two coupled kinesins. (a) shows results for a load per kinesin of 1 pN. Due to the slack transport, the probability has two peaks. (b) shows results for a load per kinesin of 4 pN. Due to the cooperative transport, the probability has only one peak. The stiffness K_c of the cargo linker is 0.125 $\mathrm{pN/nm}$. Dotted lines denote load per kinesin. Regions A and C correspond to slack transport, and region B corresponds to cooperative transport.

5.4.3 Difference in the Forces on Each kinesin

The probability of D_F demonstrates which type of motion is dominant for a given load. When a small load is applied to the cargo, the probability of D_F has two peaks which correspond to the $\pm$ value of the load per kinesin, as shown in Fig. 5.5 (a). D_F has this shape when the slack transport is the prevalent motion. If the load increases, the two peaks vanish, and one peak is visible in the center, where D_F is zero as shown in Fig. 5.5 (b). This shape corresponds to the cooperative transport.

The probability that D_F is in region B in Fig. 5.5 (where the absolute value of D_F is less than the load per kinesin) represents the probability of cooperative transport. The probability that D_F is in regions A or C in Fig. 5.5 (where the absolute value of D_F is larger or equal to the load per kinesin) represents the probability of slack transport. The probability of slack transport is referred to as slackness. Slackness can have values

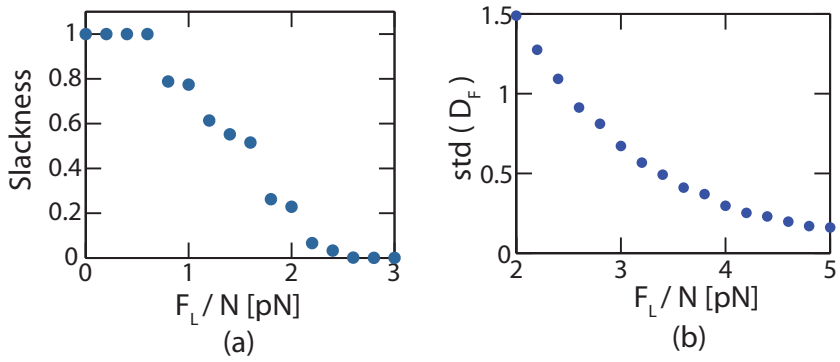

Figure 5.6: The slackness and the standard deviation of the difference D_F in the forces on two coupled kinesin. (a) shows the slackness for various values of the load per kinesin (0 - 3 pN). (b) shows the standard deviation (std) of D_F for various values of the load per kinesin (2 - 5 pN). The stiffness K_c of the cargo linker is 0.125 $\mathrm{pN/nm}$.

between 0 and 1. When the two kinesins always exert forces on the cargo in the direction of transport, slackness is 0. Otherwise, the slackness is positive, and the value increases as one kinesin (sometimes one, sometimes the other) does not assist or even impedes the transport of the cargo. The slackness is large when the load per kinesin is less than 2 pN. That is because the velocity of single kinesins does not change considerably when the force acting on a kinesin is less than 2 pN. Hence, the dependency of the motion of a kinesin to other kinesin motion is weak when the load per kinesin is less than 2 pN. The slack transport decreases as the load increases, as shown in Fig. 5.6 (a). However, the shape of the probability becomes shaper. To capture this variation, the standard deviation of D_F is calculated. The standard deviation of D_F decreases as the load increases, as shown in Fig. 5.6 (b). That is consistent with the kinesins cooperating more closely when the load is larger.

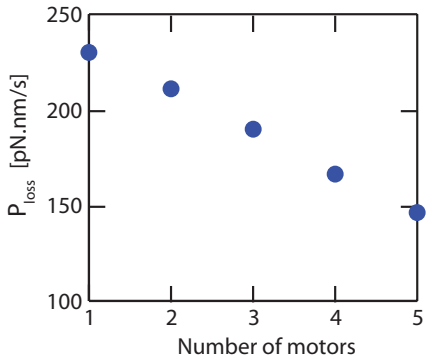

Figure 5.7: Power loss for various numbers of kinesins. This power loss is induced by the drag force exerted by the fluid on the cargo. The stiffness K_c of the cargo linker is 0.125 $\mathrm{pN/nm}$.

5.4.4 Loss of power by drag

The power loss is about 200 $\mathrm{pN.Nm/s}$ (Fig. 5.7). This value is comparable to the rate of energy released by a kinesin. Kinesins use the energy from the hydrolysis of one ATP molecule ($20\ k_BT$) per step [25, 41]. Considering that the efficiency of kinesin is about 30% [29], and considering that a kinesin carries out about 100 steps per seconds, the power from a single kinesin molecule is approximately 2,480 $\mathrm{pN.nm/s}$. Thus, kinesins dissipate about 10% of their power.

A cargo transported by a single kinesin advances 8 nm in each step. In contrast, a group of kinesins pulls their cargo with smaller advances of $8\ \mathrm{nm}/$(number of kinesins). The power loss decreases as the number of the cargo increases (as shown in Fig. 5.7) because the power loss is small when the motion of the cargo is smooth. Thus, the power loss is minimum when the cargo moves with constant velocity. The minimum power loss can be obtained as $6\pi r_c \eta v_c^2$ from Eq. (5.16), where v_c is the velocity of the cargo. The result of the power loss suggests that a group of kinesins is more efficient from the perspective of energy than single kinesin.

5.5 Conclusions

Kinesins involved in collective transport experience fluctuating forces even when the external load remains constant. Thus, the effect of a varying force on the chemical reactions at each kinesin domain has to be considered. The stochastic mechanistic model proposed recently [51, 125] captures the instantaneous force on each domain of kinesin and calculates the instantaneous chemical reaction rate based on the instantaneous force.

The collective transport by kinesins is controlled by coupled stochastic kinesins. By using an energy-like concept based on the states of kinesins, A_R enables to quantify the portion of synchronized motion in the transport for various time intervals. If a dynamics continuously fluctuates from a weakly correlated motion to a highly correlated motion, the standard deviation of A_R has a high value. Thus, the standard deviation of A_R can be used to capture such a dynamics. For the transport by two kinesins, this phenomenon is found when the load per kinesin is about 2 pN.

Another metric for the correlation among kinesins is D_c. The effects of coupling between kinesins are revealed using the normalized standard deviation of D_c. The model predicts that the coupling has the most significant effects on the relative motion of kinesins when the load per kinesin is about 4 pN. The concept of D_F is similar to D_c. However, D_F is a better method to discern the type of collective transport. By using the slackness derived from the probability of D_F, one can recognize if the two kinesins pull the cargo together/simultaneously or if sometimes one kinesin carries the entire load while the other experiences no load or an assisting load (and other times the roles of the two kinesins are reversed). The slack transport almost vanishes when the load per kinesin is 2 pN. Beyond this load, the degree of cooperation can be estimated from the standard deviation of D_F. The values of the power loss suggest that a larger group of kinesins causes a smoother

motion of the cargo.

Atzberger et al. [126] discovered that the cargo linker has a nonlinear elastic behavior (i.e., the tensile force is proportional to the cubic of the stretched length). It should be noted that the nonlinearity is considerable only for a long extended length. The cargo linker and NL in this chapter are hypothesized as linear elastic components because the stretched lengths are not sufficiently long to generate the nonlinear behavior. However, multiple kinesins coupled with nonlinear linkers are worth additional study. The linear behavior of the cargo linker could be the reason for the similar or lower velocity in multiple kinesins. If strongly nonlinear cargo linkers are synthesized and kinesins are linked via those linkers, coordination between kinesins may improve the transport velocity.

CHAPTER VI

Model to quantify the two dimensional motion of kinesin in the presence of obstacles on MTs

6.1 Summary

When a large number of molecular motors and other proteins are bound on the same MT, the interference between kinesins and other motors or proteins changes the stepping motion of kinesin and its unbinding probability from the MT. In this chapter, the stepping motion of kinesin is studied by analyzing the diffusive motion of the kinesin head. Also, the increase of the unbinding probability is considered by calculating the probability the kinesin heads contact other proteins on the MT. The methods and results described in this chapter are also used in the next chapter which characterizes the effect of tau proteins on the long range transport.

6.2 Background and motivation

Cells use various motor proteins for active transport along the cytoskeleton. Among these proteins, kinesin-1 is responsible for the anterograde cellular transport along MTs. Two identical heads of kinesin-1 are connected to their NLs which are folded at the neck by a coiled-coil structure, as shown in Fig. 6.1 (a). The neck is linked to the cargo linker which is connected to the tail domain where a cellular cargo binds. MTs have several

tubulins where the kinesin heads can bind. Kinesins repeat one mechanochemical cycle per step. At every cycle, one head moves to a different binding site 16 nm away from the previous site. Thus, the cargo attached to the kinesin moves 8 nm per step. The time required to complete one mechanochemical cycle is determined by the interaction of kinesin heads and adenosine triphosphate (ATP) [24, 127–131]. The average period of the step is about 10 ms at high ATP concentrations. Hence, the velocity of kinesins is about 800 nm/s, and varies with the load acting on the cargo [22, 24, 28, 132]. Kinesins can move about 1 μm before they are released from the MTs [2, 25, 30, 42, 56].

These characteristics of kinesins can be changed by other proteins bound on the MTs. Recent experiments suggest that proteins attached to the MT surface can act as obstacles for each kinesin [43, 50, 57–61]. Kinesin motion can be affected by other nearby kinesins. Leduc et al. [43] observed that the velocity of kinesins decreased dramatically when the number of motors on a MT exceeds a critical value. Also, nonmotile kinesin mutants bound on MTs decrease the velocity and the run length of other walking kinesins [59]. Also, the motion of kinesin is also inhibited by MT associated proteins such as tau. The effects of tau proteins on kinesin and dynein have been compared by Dixit et al. [58]. They revealed that the dependency of kinesins on tau proteins bound to the MT is 10 times larger than that of dynein. Experiments with cargoes in cells also suggest that tau proteins decrease the distance of transport by molecular motors [50].

In this chapter, the diffusive motion of kinesin heads in the absence of obstacles is modeled. Then, that diffusion model is generalized and used to predict the motion of kinesin in the presence of obstacles. Several models were proposed to describe the motion of kinesin heads [40, 133–137]. These previous models focus mainly on the one dimensional motion of the kinesin head. However, several experiments with static obstacles [59, 60, 138] suggest that kinesins can bypass obstacles by executing two dimensional movements along

the MT surface. To capture that two dimensional stepping motion, various methods are introduced and described in this chapter. First, the diffusion of the kinesin head along the surface of the MT is captured by solving the Fokker-Plank equation. Absorbing boundaries are designated on the sites near the kinesin to calculate the probability for the direction of the next step. Because one head is fixed while the other head diffuses, the NLs have to be extended for the diffusing head to reach the binding sites. Thus, the motion of the diffusing head depends on the forces which act on the NLs. A worm-like chain model (WLC) [139] is used to calculate the force needed to stretch the NLs. The neck of kinesin has a coiled-coil structure which can unwind if a large force is applied to the NLs. The unwinding is considered by using the experimental data of Bronshlogl et al. [67]. Also, the most favorable posture of the diffusing head to bind to the MT is incorporated in the model.

The interactions between kinesins and obstacles are characterized by using a diffusion model which also includes obstacles. A deterministic model is developed to predict the changes in the average velocity and run length of kinesins by static obstacles. Also, the motion of kinesin on the same MT with other plus-end directed motors or with minus-end directed motors is captured by using the stochastic model.

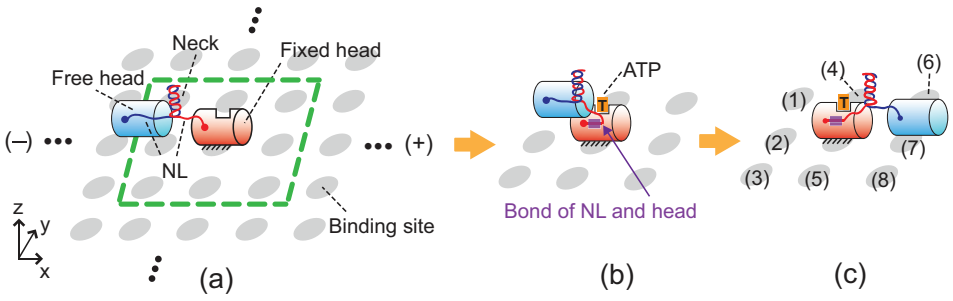

Figure 6.1: Procedure of kinesin stepping motion. (-) and (+) indicates the polarity of the MT. The binding sites around the kinesin are distinguished with the numbers in parenthesis. Because kinesins are likely to walk toward plus-end, site-(7) is defined as the forward binding site.

6.3 Diffusion model of kinesin free head

The kinesin takes its step through the procedure which is described in Fig. 6.1. The kinesin starts with the state where one head is fixed on the MT, and the other head is not bound on the MT, as shown in Fig. 6.1 (a). When ATP binds to the fixed head, the structure of kinesin changes. This change creates the bonds between the fixed head and its NL, as shown in Fig. 6.1 (b). Then, the free head diffuses until it reaches one of the binding sites, as shown in Fig. 6.1 (c). Therefore, two types of motion are considered in our model as follows: 1) The motion resulting from the structural change is taken into account by using the result of the previous study performed by Zhang et al. [140]. They predicted that the free head moves fast to the location 2 nm behind the fixed head when the structural change is completed. This resulted in our assumption that the free head starts to diffuse at that position; 2) The motion of the free head after that fast movement is captured by using our diffusion model. In the diffusion model, the free head is connected to the fixed head through the two NLs which are regarded as nonlinear springs. The springs have to be stretched for the free head to reach the binding sites. The MTs are composed of a large number of binding sites. However, the diffusion of the free head occurs around the fixed head. Thus, the model focuses on the motion in the domain containing nine binding sites, as depicted in Fig. 6.1 (a) with dotted lines. Note that this domain moves as the kinesin walk to other binding sites. The spatial probability distribution of the position of the free head is calculated by solving the following Fokker-Plank equation.

$$\frac{\partial p}{\partial t} = D\frac{\partial^2 p}{\partial x^2} + D\frac{\partial^2 p}{\partial y^2} - \frac{\partial}{\partial x}\Big(\frac{F_x}{\gamma}p\Big) - \frac{\partial}{\partial y}\Big(\frac{F_y}{\gamma}p\Big), \tag{6.1}$$

where p is the probability distribution function of the position of the free head. The direction of x and y are shown in Fig. 6.1 (a). The absorbing boundary condition (i.e., p=0) is

applied to the 8 neighboring binding sites, as shown in Fig. 6.2 (a). The reflective boundary conditions (i.e., no flux along the normal direction of the boundary) are used for other boundaries. D is the diffusion coefficient, and γ is the drag coefficient of the free head. The head is assumed as a cylinder with the length of 7 nm and the diameter of 4.5 nm. The size of the head is obtained from the previous study on the crystal structure of kinesin heads [141]. By using the method proposed by Swanson et al. [142] to calculate a drag coefficient of cylinders in low Reynolds numbers, the value of γ is calculated as 5.625×10^{-8} g/s with the viscosity of water. Then, the diffusion coefficient is calculated as $73.6\ \mu\mathrm{m}^2/\mathrm{s}$ with the temperature of 300 K. Note that the dependency of γ and D on the moving direction is negligible for the geometry of the used cylinder [142]. F_x and F_y are the x and y components of the force acting on the free head resulting from the stress in the NLs when the free head is located at certain positions. The software COMSOL is used to solve this partial differential equation with the finite element method.

6.3.1 Stretching of kinesin structure

The relation of the position of the free head and the stress in the NL depends on the number of amino acids (AAs) in the structure. Kinesin-1 has fourteen AAs (AA 325-338) in each NL. However, only four AAs (AA 335-338) are deformable for the docked neck linker (DCNL) because AA 334 of the DCNL tightly bound to the fixed head with two backbone hydrogen bonds [143]. The stretching of NLs is considered by using the WLC [66, 139]. The neck consists of two coils which are connected to each NL. The coils are coiled with each other about 10 turns, and that coiled-coil structure is maintained by hydrophobic interactions [144]. It is observed that each turn of the neck is unwound by forces about 10 pN [67]. Because the unfolding of one turn increases the number of AAs by 3 or 4 for each NL, the relation of the force acted on the NL and its length changes if the

force reaches the unwinding forces, as shown in Fig. 6.2 (b). The forces in Eq. (6.1) (F_x and F_y) are obtained by considering the WLC and the unwinding of the neck. Details are described in .

6.3.2 Binding with tilted posture

To consider the effect of the affinity of the kinesin head and the binding sites, the positions of the specific AAs of the free head are investigated. First, AA 142–145, AA 273–281, AA 238 and AA 255 are responsible for the binding to the MT [143]. Hereafter, these AAs are referred as the attachable AAs. The head can bind to a binding site when the center of the attachable AAs reaches the binding site. Second, the NL is not connected to the center of the free head, as shown in Fig. 6.2 (c). Due to this structure, if the free head bind to site-(8) with a tilted posture, the length of the two NLs required to reach that site is shorter than the distance between that diagonal site and the fixed head, as shown in Fig. 6.2 (d). Thus, it is assumed that the binding to the diagonal site with tilted posture is favorable to the free head. To consider this behavior, the positions of the absorbing boundaries in the domain are changed, as shown in Fig. 6.3 (a). Note that this behavior is only applicable to the diagonal sites because there is not enough space for the free head to rotate when it is near the side, forward, or backward binding sites due to the geometric interference with the fixed head.

6.3.3 Fit to the experiment

The spatial probability distribution of the free head calculated from our model is shown in Fig. 6.3 (a). This probability distribution depends on the three parameters; ℓ_{DC}, d_{side}, and θ_d. Some AAs of the DCNL are docked to the fixed head, and others are not. ℓ_{DC} is the length of the docked part. The distance between two adjacent binding sites along the tangential direction of the MT is referred to as d_{side}. θ_d represents the allowable angle

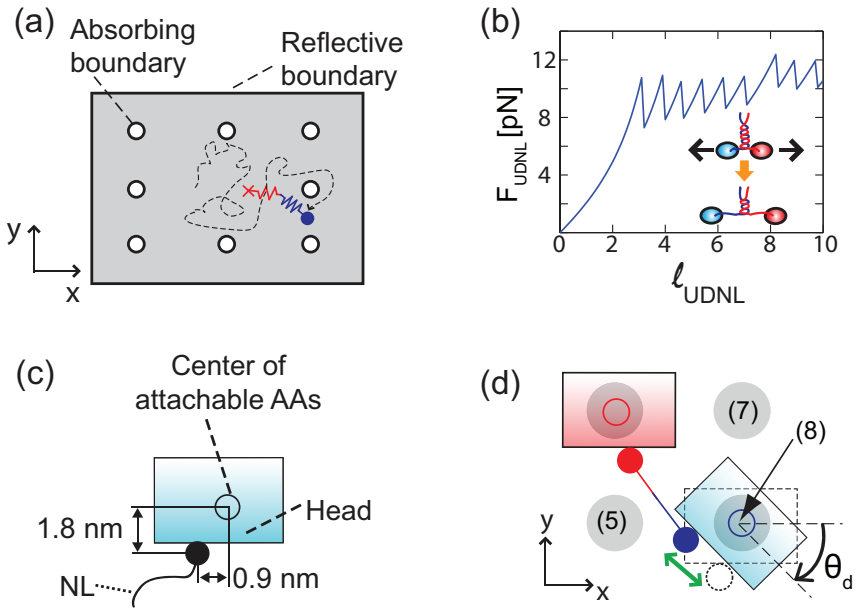

Figure 6.2: Diffusion model of kinesin motion in the absence of obstacles. (a) shows the domain where the diffusion of free head occurs. The fixed head is located at the center of the domain. (b) depicts the changes of the force over the length of the undocked neck linker (UDNL). The hollow circle in (c) is the center of the attachable AAs. The filled circle represents AA324 where the free head and its NL are connected. (d) shows the binding of the free head to the diagonal site with the tilted posture.

for the binding with tilted posture. The hypothesis of the interaction between the free head and the binding site is as follows: If the free head is tilted at an angle larger than θ_d, the attraction between the binding site and the attachable AAs of the free head is not strong enough to cause the binding. If the center of attachable AAs is close to the binding site, and the tilted angle is less than θ_d, the interaction between the head and the site is strong. Thus, the head can bind to the site, and then be aligned along the MT axis by the interaction between the attachable AAs and the site.

The values of parameters are determined by using the previous experiments. Yildiz et al. [68] tracked the motion of the kinesin heads by labeling them with quantum dots. Their results show that 13% of the kinesin step involves the motion along y, and 70%

of that lateral motion occurs together with the motion toward the plus-end of the MT. Also, Nishiyama et al. [29] measured that the probability of backward step increases exponentially over the resisting load acting on the kinesin. According to their observation, the probability ratio of forward and backward step is about 1.3 when the resisting load is about 7 pN. The model calculated the probability of the free head binding to a certain site by integrating the flux $\dot{P}$ of the probability flowing out through the boundaries of the site (which is shown in Fig. 6.3 (b)) over time. A set of parameters ($\ell_{DC} = 2.9$ nm, $d_{\text{side}} = 6.4$ nm, and $\theta_d = 47°$) satisfies the probability of step observed in both experiments. The probabilities of forward, backward and sideway step in the absence of resisting load are presented in Fig. 6.3 (c). ℓ_{DC} and d_{side} are similar to the measured values of the previous studies. The distance between AA324 and AA334 of DCNL in the crystal structure of kinesin [145] is about 3 nm. Also, d_{side} is 6.4 nm when the diameter of MT is 26.5 nm. This diameter is in the range of the actual diameters of MTs observed in the cell [146, 147].

To predict the effect of the load on the behavior of kinesin, $P_{b,i}$ are calculated when the resisting load is exerted on the kinesin. Because the equilibrium position of the free head is shifted toward the center of the domain by the resisting loads, the probability of the sideway step considerably increases even for the small loads, as shown in Fig. 6.3 (d). This suggests that the sideway step is also responsible for the decrease in the velocity of kinesins by the load. Also, the probability of the backward step is noticeable when load is larger than 6 pN.

6.4 Results

The motion of kinesin is affected by the interaction of obstacles and kinesins and by the number of the obstacles on the MT. Thus, the diffusion model is used to consider the

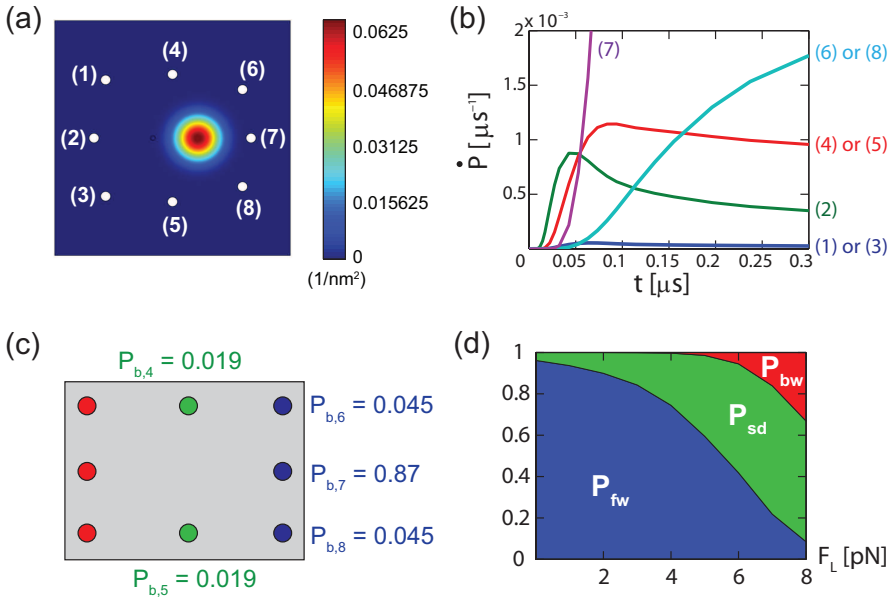

Figure 6.3: Probability of binding on sites. (a) is the spatial probability distribution of the position of the free head in the absence of external loads after $1\ \mu s$ since the diffusion started. (b) shows the rate of the probability flowing out through each absorbing boundary of binding sites. The numbers in (c) denote the probabilities regarding the direction of step ($P_{b,i}$). $P_{b,1-3}$ are not shown because their values are very small. (d) shows the changes in the probabilities of forward step ($P_{\rm fw} = P_{b,6} + P_{b,7} + P_{b,8}$), sideway step ($P_{\rm sd} = P_{b,4} + P_{b,5}$), and backward step ($P_{\rm bw} = P_{b,1} + P_{b,2} + P_{b,3}$) when the external resisting load acts on the kinesin.

interaction of the kinesin head and obstacles located near the kinesin. When an obstacle is bound on a binding site, the free head is not able to move to that binding site. Thus, a reflective boundary is located on that site, as indicated with $C_{\rm obs}$ in Fig. 6.4 (a). The shape of the reflective boundary is assumed as a circle. Then, the changes in the velocity and run length over the number of obstacles on the MT are calculated. Also, the effect of other molecular motors on the motion of kinesin is predicted when they walk on the same MT.

6.4.1 Interaction between kinesins and obstacles

The interaction between kinesins and obstacles modifies the unbinding probability of the kinesin from the MTs (or the run length) and its walking velocity. The effect of obstacles on the unbinding probability depends on the probability that the free head contact the obstacle ($P_{\rm cnt}$). The changes in the velocity are determined by the required number of steps to bypass obstacles ($N_{\rm step}$). Therefore, these two quantities are calculated for different sizes and numbers of obstacles. To characterize the effect of the location of obstacles, small virtual obstacles occupying single binding site are used. Because the distance between adjacent binding sites are about 8 nm along the x axis and 6 nm along the y axis, two different sizes of obstacles ($R_{\rm obs} = 4$ and 5 nm) are located near the kinesin.

When obstacles are located near the kinesin, the unbinding probability of kinesin ($P_{\rm ub}$) can be obtained as

$$P_{\rm ub} = P^0_{\rm ub} + P_{\rm cnt} P_{\rm ub,cnt} \ , \tag{6.2}$$

where $P^0_{\rm ub}$ is the unbinding probability per step in the absence of obstacle which are obtained from chapter VI. The changes in the unbinding probability caused by the interference with obstacles depends on two probabilities; the probability of the free head to contact obstacles ($P_{\rm cnt}$) and the probability of kinesin to unbind when the free head contact the obstacles ($P_{\rm ub,cnt}$). $P_{\rm cnt}$ can be calculated with the probability distributions along the reflective boundary of the obstacle as

$$P_{\rm cnt} = \int_{t_0}^{t_f} \oint_{C_{\rm obs}} p \ d\ell \ dt \tag{6.3}$$

where t_0 and t_f are the initial and final time when solving Eq. (6.1). $P_{\rm ub,cnt}$ depends on the type of obstacles present on the MTs. Thus, its value can be obtained using the experimentally measured run length of kinesins in the presence of obstacles. $P_{\rm cnt}$ for the obstacle located in the site-(7) is large compared to other sites, as shown in Fig. 6.4 (b),

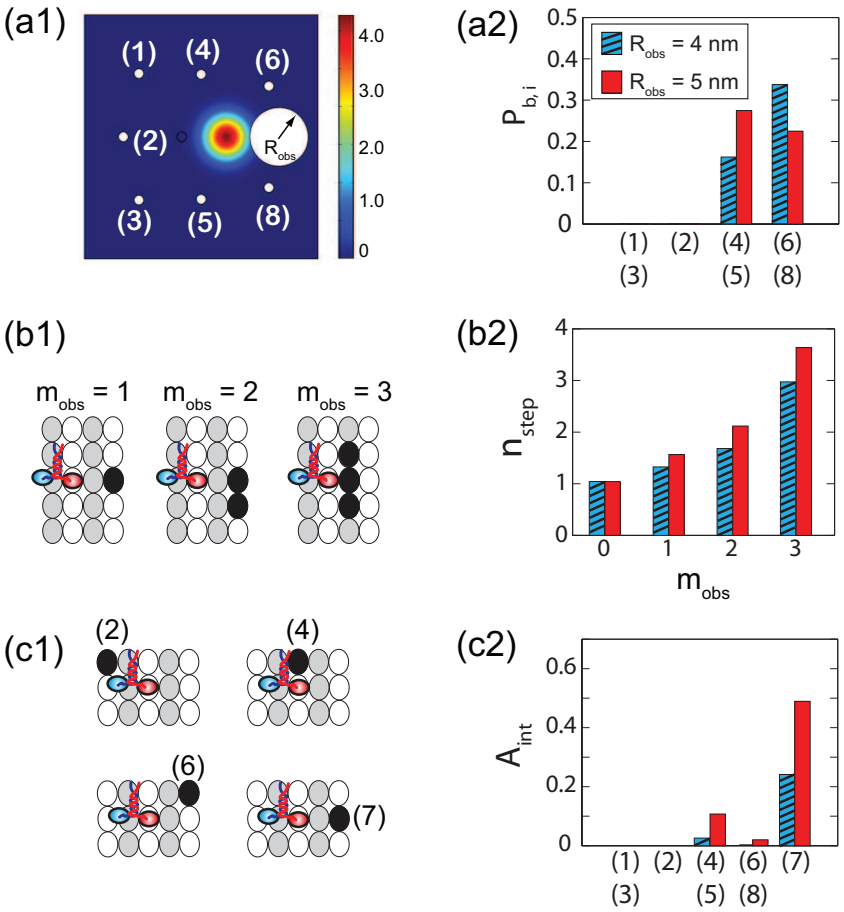

Figure 6.4: Motion of kinesin near obstacles. (a) shows the probability distribution over the domain if the binding site in front of the kinesin is occupied by an obstacle. The blocked region formed by the obstacle is included into the domain with the reflective boundary. (b) is the probability $P_{\rm cnt}$ when one of the neighboring site is occupied by obstacles. The numbers in parenthesis denote the binding site where the obstacle is located. (c) describes the situation when three binding sites in front of kinesin are blocked by obstacles ($n_{\rm bs,obs} = 3$). (d) shows the number of steps ($N_{\rm step}$) required to bypass obstacles when several binding sites ($n_{\rm bs,obs} = 1 - 7$) are occupied by obstacles.

because the free head tends to diffuse around the site-(7) due to its structural change. As expected, the probability to contact increases as the size of the obstacle increases.

The number of steps to bypass obstacles is increased significantly by the number of binding sites occupied by obstacles ($n_{\rm bs,obs}$), as shown in Fig. 6.4 (c) and (d). The filled

dot denotes the number of steps when selecting the optimal path with no failure. N_{step} of kinesin is much larger than values represented by the filled dots due to their stochastic stepping motion. Kinesins have to repeat several steps until they find a way to bypass obstacles by chance. Because N_{step} is affected by $n_{\mathrm{bs,obs}}$ and R_{obs}, the number of binding sites occupied by single obstacle and the value of R_{obs} can be obtained using the velocity of kinesins in the presence of obstacles.

6.4.2 Static obstacle

The interaction between kinesins and the unmovable kinesin, which acts as a static obstacle to walking kinesins, is characterized by three parameters, R_{obs}, m_{obs}, and $P_{\mathrm{ub,cnt}}$, where m_{obs} is the number of binding sites occupied by a single obstacle, as shown in Fig. 6.5. In the previous experiment performed by Telley et al. [59], the motion of kinesin was observed when the number of obstacles (i.e., unmovable kinesins) attached to the MT is 8 $\%$ compared to the number of obstacles if the MT is fully coated with the obstacles. The velocity and run length were decreased to 81 $\%$ and 57 $\%$ compared to the values in the absence of obstacles. The velocity depends on the R_{obs} and m_{obs}, whereas the run length or unbinding probability is affected by $P_{\mathrm{ub,cnt}}$ as well as R_{obs} and m_{obs}. Thus, the values of R_{obs} and m_{obs} are obtained using the measured velocity. After that, $P_{\mathrm{ub,cnt}}$ is determined comparing the run length of model and the experiment.

To obtain the value of parameters, a deterministic model is developed. The deterministic model is capable of calculating the velocity and run length for various numbers of obstacles by using the behavior of kinesin near obstacles explained in section 6.4.1. The velocities can be calculated as

$$V(\rho) \simeq V_0 \frac{1}{1 + \sum_{k=1}^{N} a_k \rho^k}, \tag{6.4}$$

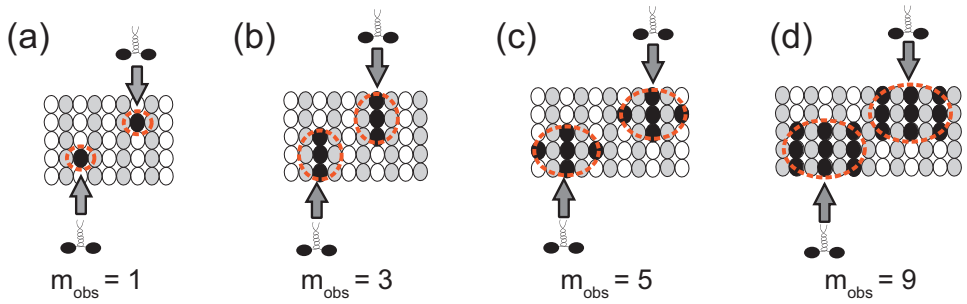

Figure 6.5: The number of occupied sites per obstacle. The figures show the examples of the MT if each unmovable kinesin occupy one (a), three (b), five (c), or nine (d) binding sites. The filled black circles are the binding sites occupied by the obstacles.

where $V(\rho)$ is the velocity when the molar ratio of the number of obstacles to the number of tubulin dimers of the MT is ρ. V_0 is the velocity in the absence of obstacles. The term $k = 1$ is introduced to capture the effect of single obstacles. The term $k = 2$ is required to consider the effect of two series of obstacles that are adjacent to each other along the y axis. The coefficient a_k is determined by the number of steps to bypass obstacles, which can be calculated in the diffusion model. The derivation of this equation is provided in Appendix A. Tab. 6.1 shows the velocities for various $R_{\rm obs}$ and $m_{\rm obs}$. The values of parameters are determined as $R_{\rm obs} = 5$ nm and $m_{\rm obs} = 3$ for the unmovable kinesin obstacles.

The parameter $P_{\rm ub,cnt}$ can be obtained by using the run length. The run length of the deterministic model can be calculated as

$$RL(\rho) = RL_0 \frac{1}{1 + \sum_{k=1}^{N} b_k \rho^k} \frac{V(\rho)}{V_0}, \tag{6.5}$$

where $RL(\rho)$ and RL_0 are the run length in the presence and absence of obstacles. The value of b_k depends on $P_{\rm ub,cnt}$. The value of $P_{\rm ub,cnt}$ is determined as $0.023\,{\rm nm/ms}$ because it produce the run length of the experiment. The derivation of this equation is also provided

m_{obs}	R_{obs} [nm]	V/V_0
1	4	0.99
1	5	0.98
3	4	0.88
3	5	0.82
5	4	0.9
5	5	0.85
9	4	0.94
9	5	0.92

Table 6.1: The velocity for various m_{obs} and R_{obs}

in A.

The stochastic model is developed to address the limits of the deterministic model. The deterministic model is incapable of considering the effect of temporal/spatial resolution of the experiments. Therefore, the velocity and run length are calculated again using the Monte-Carlo simulation with the stochastic model because this method allows to consider the resolution used in the experiments. The stochastic model is developed by integrating the diffusion model with the mechanistic model in chapter VI, which can describe the stochastic motion of the kinesin in the absence of obstacles. Details on the stochastic model are provided in Appendix A. The stochastic model with $R_{\mathrm{obs}} = 5\,\mathrm{nm}$ and $m_{\mathrm{obs}} = 3$ provides a similar velocity of the deterministic model because the effect of the resolutions on the velocity is not considerable. However, the run length is more sensitive to the resolution of the experiment. Thus, the value of $P_{\mathrm{ub,cnt}}$ is changed to 0.044 nm/ms when the

stochastic model is used to obtain the experimentally observed run length.

6.4.3 Moving obstacles

The characterization of interactions between moving kinesins and static kinesins enables us to predict the motion of kinesin when static or motile motor proteins exist on the MT. $\mathrm{K} + \mathrm{M}^{\Phi}$ represents the situation when the motion of kinesin is disturbed by the unmovable kinesins. Also, several kinesins can walk on the same MT ($\mathrm{K} + \mathrm{M}^{+}$). ($\mathrm{K} + \mathrm{M}^{-}$) denotes the situation when the kinesin share the same MT with minus-end directed motors. These cases are depicted in Fig. 6.6 (a).

When several motors share the same MT, the motion of kinesin has several characteristics. The decrease in the run length over ρ is more significant than the changes in the velocity because the run length is also affected by the reduction of the velocity as well as the increased unbinding probability by obstacles, as calculated in Eq. (6.5). Also, the changes in the velocity of ($\mathrm{K} + \mathrm{M}^{+}$) over ρ are not considerable, as shown in Fig. 6.6 (b). For the traffic of ($\mathrm{K} + \mathrm{M}^{+}$), the kinesin is not likely to meet other kinesins because every motor move in the same direction. Furthermore, the decrease in the velocity of ($\mathrm{K} + \mathrm{M}^{-}$) are small compared to ($\mathrm{K} + \mathrm{M}^{\Phi}$) due to the bypassing ability of the minus-end directed motors, as shown in Fig. 6.6 (b). For the kinesin and minus-end directed motors used in this chapter, the time for the chemical reaction per step (i.e., 1-10 ms) is much longer when compared to the time required to take a single step (i.e., 1-10 μs). Thus, when a kinesin confronts a minus-end directed motor, the instant of the kinesin taking a step is not likely to overlap with the stepping time of the minus-end directed motor. This behavior prevents the kinesin and the minus-end directed motor from taking steps in the same direction. As a result, the kinesin and the minus-end directed motor can pass each other fast. However, the kinesin need to take several steps to bypass static motors. Also, he

decreases of the run length are large with the order ($\mathrm{K} + \mathrm{M}^{\Phi}$), ($\mathrm{K} + \mathrm{M}^{-}$), and ($\mathrm{K} + \mathrm{M}^{+}$), as shown in Fig. 6.6 (c), because the changes of the run length depend on the decreases in the velocity. Details on the realization of the motion of the kinesin along with other movable motors are provided in Appendix A.

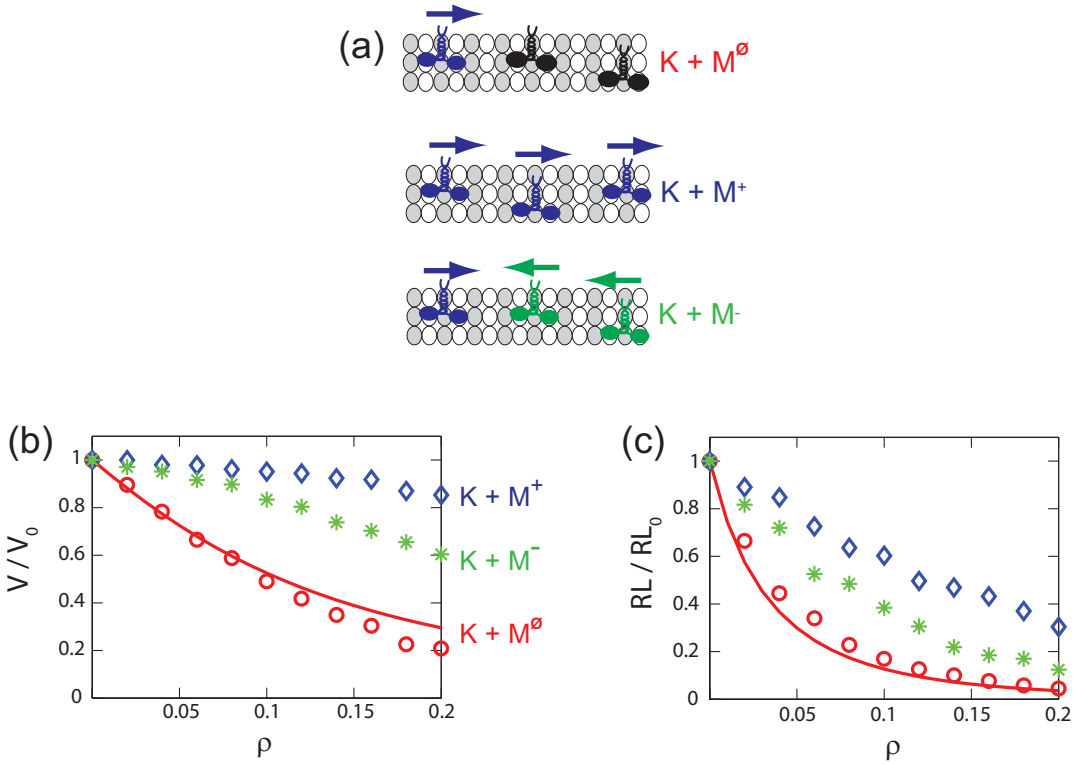

Figure 6.6: The velocity and run length of kinesins over the density of motors. (a) depicts the motions of the kinesin in ($\mathrm{K} + \mathrm{M}^{\Phi}$), ($\mathrm{K} + \mathrm{M}^{+}$), and ($\mathrm{K} + \mathrm{M}^{-}$). The motors with the arrow directing to the right are the moving kinesins. The motors with the arrow directing to the left are the minus-end directed motors. The unmovable kinesins are presented with motors without an arrow. The ρ represents the molar ratio of unmovable kinesins and tubulin dimers for $\mathrm{K} + \mathrm{M}^{\Phi}$, the molar ratio of walking kinesins and tubulins for ($\mathrm{K} + \mathrm{M}^{+}$), and the molar ratio of minus-end directed motors and tubulins for ($\mathrm{K} + \mathrm{M}^{-}$), respectively. The curves denote the velocity and run length for ($\mathrm{K} + \mathrm{M}^{\Phi}$) obtained from the deterministic model. The results denoted with circles, stars and diamonds are calculated from the stochastic model.

6.5 Conclusions

The diffusion model developed in this work predicts the two-dimensional motion of kinesin. The model suggests that both the unwinding of the neck and the binding with tilted posture can take place during the stepping motion of kinesin. If one of the mechanisms are not allowed, the model produces very small probability to step toward diagonal sites compared to the probability measured in the experiment [68]. The values of the probabilities are provided in Appendix A.

In this chapter, the interaction between the walking kinesins and unmovable kinesins are characterized. By using that interaction, the effects of other motors on kinesins are predicted when they move on the same MT. If several kinesins share one MT together, their velocities are almost not affected by other kinesins on the MT. The deceleration of kinesins by minus-end directed motors is also not considerable. These results suggest that cells can handle several intracellular transports effectively with a small number of MTs. However, both the velocity and run length decrease considerably by unmovable kinesins. Thus, the malfunctions of few motors or other static proteins bound on the MT could interrupt the transport performed by kinesins.

This result is consistent with the experimental observations on degradation of the transport by tau proteins which can be static obstacles to the kinesin. The run length of kinesin decreases for the excessive density of tau proteins in several experiments [50,58,148,149]. The experiments observed that the motion of single kinesins with small cargoes is not slowed down by tau proteins. However, the transport velocity of cargoes can be modulated by tau proteins. Large cargoes such as mitochondria are transported by several kinesins to overcome large viscous force in cytoplasm. Tau proteins are observed to increase the unbinding rate of kinesins and decrease the rebinding rate of kinesins to the

MTs [58, 148–150]. Thus, the number of kinesins bound to the MT could be decreased by tau proteins. For this reason, the large cargo can be transported slowly. Furthermore, slowly transported large cargoes can also act as large obstacles to other kinesins. As a result, the entire transport system would not operate normally.

The effects of obstacles on the motion of kinesin are important because several neurodegenerative diseases such as Alzheimer's disease (AD) could be the result of the abnormal intracellular transport. The negative effects of obstacles on the intracellular transport are observed *in vivo*. The transport of several cargoes is decelerated or failed by the excessive tau proteins [46, 48, 49]. Therefore, characterization of the motion of kinesin in the presence of tau proteins is necessary to reveal the quantitative relation between the degradation of the intracellular transport and tau proteins. The diffusion model can be used to characterize the interaction between tau proteins and the motion of kinesin.

CHAPTER VII

A novel model to consider kinesin mediated axonal transport and its regional traffic jam caused by tau proteins

7.1 Summary

The intracellular transport can be interrupted by tau proteins because they are capable of binding to the MTs. In this chapter, a new model is developed to characterize the binding of tau proteins to the MTs and the interaction between kinesins and tau proteins. It is predicted that the transport velocity along the long axon is not changed considerably by the concentration of tau protein. Thus, new metrics are proposed to quantify the regional traffic jam caused by tau proteins because this regional traffic congestion is highly sensitive to the concentration of tau protein.

7.2 Background and motivation

Motor proteins are responsible for the axonal transport of a variety of cargoes such as mitochondrion, neurotransmitters, and neurofilaments in the neuron [7–9]. Among them, kinesins walk from the cell body to the synapses along the MT biological track. The appropriate concentration of tau proteins is important to the transport with the following reasons: First, MTs can collapse if the amount of tau protein is not enough. Long and

hollow cylindrical structure of MTs is created by the polymerization of tubulin dimers. The tubulins located at the plus-end of MTs can be depolymerized in the absence of molecules which stabilize the structure of MTs. Because neurons use tau proteins to maintain their MTs [151, 152], a low concentration of tau protein can be noxious to the MTs in the axon; Second, excessive tau proteins can interrupt the motion of kinesin by blocking respective binding sites on MTs. It is measured that kinesins are easily released from the MT and that they slowly bind to the MT in the presence of excessive tau proteins [58, 148–150, 153]. Thus, the walking ability of kinesin is less useful to transport intracellular cargoes if there are excessive tau proteins are in the axon.

The effects of excessive tau proteins on kinesin mediated transport have been observed both *in vitro* experiments [58, 148–150, 153] and *in vivo* experiments [46–50]. For *in vitro* experiments, several behaviors of kinesin are modified by excessive tau proteins. The run length of kinesins is decreased [58, 149, 150, 153]. The cargoes transported by single kinesins are released from the MTs with high probability when they confront clusters of tau proteins on the MTs [58]. McVicker et al. [149] revealed that the ATPase of kinesin molecules is accelerated if they walk on the MTs that are coated with tau proteins. Also, the time required for the unbound kinesins to bind to the MTs is increased [148]. For *in vivo* experiments, the intracellular transport is not performed normally in various cells, including neurons, if they have excessive tau proteins. In the CHO cells, the transport of several cellular organelles (e.g., mitochondria and endoplasmic reticulum) to the cell periphery is inhibited if additional tau proteins exist [48, 50]. In neurons, mitochondria, peroxisomes, neurofilaments, and amyloid precursor proteins also fail to be transported along axons or dendrites in the presence of large numbers of tau proteins [46, 47, 49].

The goal of this chapter is to develop a model capable of predicting the axonal transport of cargoes in the presence of excessive tau proteins. This model accounts for both

the motion of the cargo when it is transported by kinesins and the Brownian motion of the cargo when its kinesin is released from the MT. The stochastic transitions between those two motions are also captured. The distribution of tau proteins on the MT surfaces is necessary to predict the motion of kinesin on MTs coated with tau proteins. That distribution is obtained by considering the affinities of tau proteins on the tubulin dimers of the MTs.

The model predicts the long range transport when the concentration of cargoes in the axon is small and large. When the number of cargo in the axon is small, the interference between cargoes or between kinesins is negligible. The times required to transport the cargo along the $50\ \mu\mathrm{m}$ long axon are calculated for various concentrations of tau protein and various densities of MT in the axon. When the axon contains a large number of cargoes, the interaction between kinesins and the interference between cargoes are considered. The effect of tau on the traffic of the cargoes is predicted. Also, a new metrics is introduced to estimate the condition of MTs more effectively by using the behavior of the kinesin near tau clusters.

7.3 Model

In this chapter, various types of motions of kinesins and their cargoes depicted in Fig. 7.1 are modeled. Also, the binding of tau proteins on MT and their effect on kinesins are considered to predict the changes in the transport by tau proteins.

7.3.1 Cargo bound to the MT via kinesin: walking and unbinding

For kinesins, the walking motion, the unbinding, and their dependency on the obstacles on the MT (namely tau proteins in this chapter) are captured with the mechanistic model introduced in chapter II-VI. The walking motion of kinesin is determined by the period and direction of its step. Its stochastic stepping period is calculated with the stochastic chemical kinetics described in chapter II. While the kinesin takes a step, one of its heads

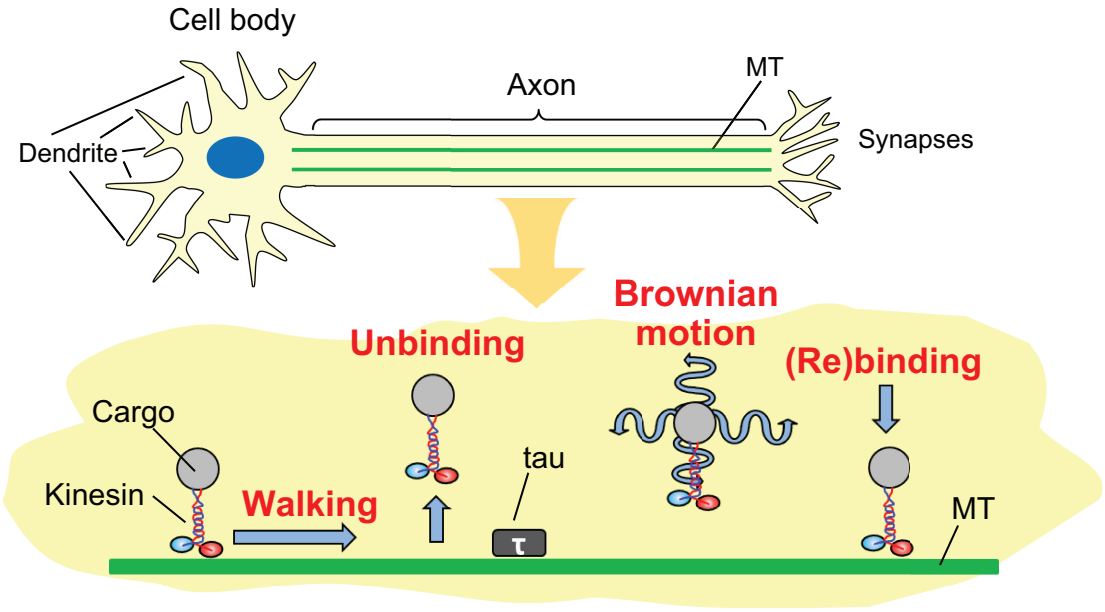

Figure 7.1: Various motions of the cargo in the neuron. When the kinesin is attached to the MT, the cargo is hauled by the kinesin. If the kinesin unbinds from the MT, the kinesin and its cargo diffuse around because of the Brownian motion. When the diffusing cargo moves close to the MT, its kinesin can bind to the MT and start to walk again. The tau proteins attached to the MT affect these various motions.

is bound to the MT and the other head moves by diffusion and conformational change in the structure. Thus, the direction of a step is considered according to the model in chapter VI, which is capable of capturing the diffusing motion of the kinesin head. The unbinding probability calculated in chapter IV and VI are used to capture the instant of releasing from the MT. When the kinesin walks along the MT, the motion of its cargo is calculated with Stokes' law as

$$v_c = \frac{F_c}{6\pi r_c \eta}, \tag{7.1}$$

where v_c is the velocity of cargo. F_c is the force acting on the cargo transferred from the kinesin. This force can be calculated with the stiffness of the cargo linker and the positions

of the cargo and the kinesin.

7.3.2 Cargo released from the MT: the Brownian motion and rebinding

When the kinesin is not bound on the MTs, the translational and rotational Brownian motion of the cargo in 3-dimensional space is calculated by the following equation.

$$x(t + \Delta t) = x(t) + r_{\mathrm{ndr}}(\sqrt{2D_c\Delta t}), \tag{7.2}$$

where x can be the position and the rotation angles of the cargo. Δt is the time step, and r_{ndr} is the normally distributed random number with a standard deviation (std) of $\sqrt{2D_c\Delta t}$ and zero average. D_c is the translational diffusion coefficient ($\frac{k_BT}{6\pi r_c\eta}$) of the cargo when Eq. (7.2) is used to obtain the position of the cargo. D_c represents the rotational diffusion coefficient ($\frac{k_BT}{8\pi r_c^3\eta}$) of the cargo when Eq. (7.2) is used to calculate the rotation of the cargo. Different values of r_{ndr} are used in different time steps to capture the random motion. The Brownian motion of the cargo is confined by the cell membrane and the MTs, as shown in Fig. 7.2 (a).

Significantly intensive computation is required to consider the Brownian motion of unbound kinesins because their heads diffuse with very high speed due to its small size. Instead, the following hypothesis is used; the probability of the position of the kinesin heads is uniformly distributed in the spherical space which has its center at the point where the kinesin attaches to the cargo, as shown in Fig. 7.2 (b). The radius of the spherical space is determined as 60 nm because it is the length of the kinesin (L_c) in the absence of stretching force [154]. This assumption is plausible considering the high diffusional coefficient of kinesins (22 $\mu\mathrm{m}^2/\mathrm{s}$) [155] and the restriction of the diffusion by the cargo linker.

When the unbound kinesin is far from a MT, the kinesin is not able to bind to the MT. When the heads of the unbound kinesins move close to the MT by thermal forces,

the attractive force between the heads and tubulins increases. Then, the probability of the kinesin to rebind to the MT becomes considerable. Thus, it is assumed that the MT has an attractive zone covering the outer surface of the MT with thickness 1 nm, as shown in Fig. 7.2 (c). If the head of the unbound kinesin enters this region, the kinesin can bind to the MT. The rebinding probability (P_{reb}) is calculated as

$$P_{\mathrm{reb}} = \dot{p}_{\mathrm{reb}} \frac{V_{\mathrm{K}\cap\mathrm{AZ}}}{V_{\mathrm{K}}} \Delta t, \tag{7.3}$$

where $V_{\mathrm{K}\cap\mathrm{AZ}}$ is the intersected volume created by V_K and V_{AZ} which are described in Fig. 7.2 (b) and (c), respectively. $\dot{p}_{\mathrm{reb}}$ is the parameter of the model. The value of $\dot{p}_{\mathrm{reb}}$ is obtained as $7.1 \times 10^5\ \mathrm{s}^{-1}$ by using previous experiments [76] on the binding rate of kinesins to the MTs.

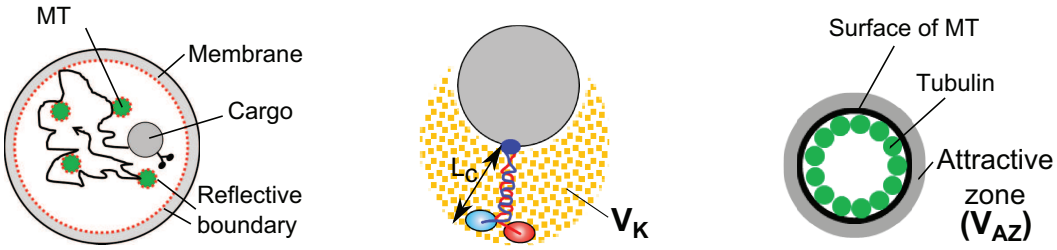

Figure 7.2: Brownian motion and rebinding. (a) shows the Brownian motion depicted from the cross section of the axon. The dots in (b) indicate the spherical space where the unbound kinesin heads can exist with spatially uniform probability distribution. (c) shows the cross section of the MT. The gray layer represents the attractive zone of the MT.

7.3.3 Binding of tau protein on MT

The following behaviors of tau protein (regarding its binding to MTs) are considered to obtain MTs coated with tau proteins: 1) When the molar ratio m_τ (= concentration of tau / concentration of tubulin dimer) is smaller than 0.2, almost all tau proteins bind

to the MTs [58, 69]. This molar ratio of 0.2 is also consistent with the stoichiometries obtained from other experiments [156–158]. Thus, a single tau protein is assumed to occupy four tubulin dimers, as shown in Fig. 7.3 (a). Single tau molecules are arranged with the square layout (i.e., two by two) because one tau molecule is believed to interact with two protofilaments [159, 160]. This interaction is also consistent with previous observation [161] which suggests that tau molecules bind both along and across protofilaments. 2) Some tau proteins fail to bind on the MTs when m_τ is higher than 0.2 [69]. This suggests that tau proteins are unlikely to bind to tubulins which are already occupied by single tau proteins. 3) Tau clusters are observed on the MT for high m_τ [58, 69, 162]. Note that if two or more tau proteins bind to the same location on the MT, those tau proteins are considered as tau cluster in this dissertation. Once one tau succeeds to bind to tubulins where one tau protein is already bound (even if the probability to bind to those tubulins is small), those tau proteins act as seed, so that other free tau proteins can easily bind to the tau clusters. This is consistent with other observations, according to which tau dimers function as building blocks in the formation of aggregation of tau proteins in the absence of tubulins [163]. 4) For large m_τ, the ratio of unbound tau proteins to bound tau proteins increases with m_τ. To capture this behavior, it is assumed that tau can bind to tubulins only when the number of tau proteins bound on the tubulins is equal or less than $N_{\max}$, as shown in Fig. 7.3 (b).

To consider the interaction between tubulins and tau proteins, tubulins on MTs are classified into three types. Then, different affinities to tau proteins are assigned to each type. The first type is tubulins with no tau proteins attached (TUB_1), as shown in Fig. 7.3 (c1). Thus, the affinity ($K_{a,1}$) between TUB_1 and tau proteins are strong. The second type is tubulins which already have one bound tau and their adjacent sites have no or one tau (TUB_2), as shown in Fig. 7.3 (c2). The affinity ($K_{a,2}$) between TUB_2 and tau pro-

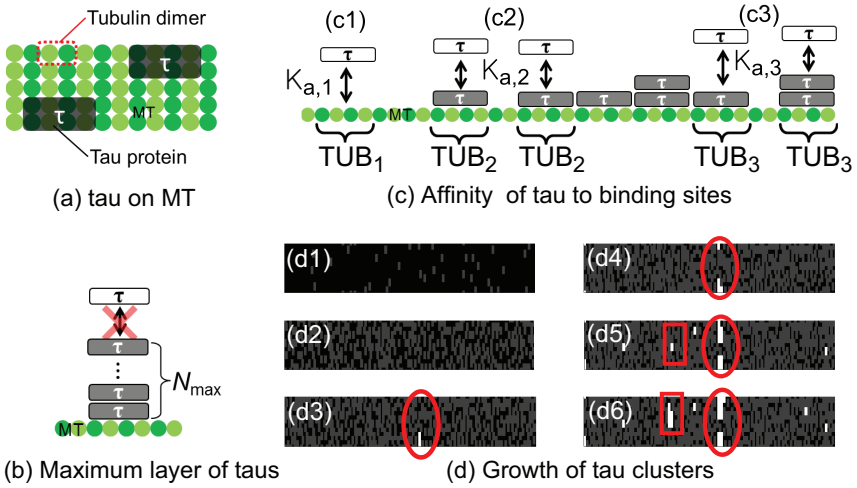

Figure 7.3: Binding of tau proteins on tubulins (a) describes the used assumption on the configuration of bound tau proteins. (b) describes the maximum number of tau proteins which can be stacked on the MTs. (c) describes three distinct affinities between free tau proteins and tubulins or bound tau proteins. (d) shows an example of the growths of tau clusters predicted from the model. Tubulins with no tau are depicted with black dots, and tubulins with single tau are described with gray dots. White dots are tubulins with two or more tau molecules (tau clusters). The growths of two tau clusters are indicated with the circle and rectangle. The numbers in parenthesis indicate the values of m_τ.

teins are weak. The third type (described in Fig. 7.3 (c3)) is the tubulins (TUB_3) where tau clusters are located. TUB_3 also includes the tubulins adjacent to tau clusters. Because TUB_3 represents the binding sites of the MT affected by tau clusters, their affinities ($K_{a,3}$) to tau proteins are strong. The values of $K_{a,1-3}$ are obtained as 3, 0.003, and 10 $\mu\mathrm{M}^{-1}$ by using the experimental data [58, 69]. $N_{\max}$ is obtained as 12. Detailed descriptions on the binding and the method used to acquire the values of parameters are provided in Appendix B.

7.3.4 Interference between kinesin and tau protein

Tau proteins affects several dynamics of kinesin; the walking, the unbinding from the MT, and the binding to the MT. First, the walking kinesin are changed by tau proteins bound on MTs. The velocity of single kinesins increases by about 10% in the presence of tau proteins [58]. Moreover, the ATPase of kinesins is accelerated when kinesins meet tubulins where single tau proteins are attached [149]. This suggests that tubulins occupied by single tau proteins do not act as obstacles to kinesins. The accelerated ATPase by tau proteins is incorporated in the model by increasing turnover rate in the ATPase by 10% when kinesin heads are bound on tubulins where single tau proteins are attached.

The unbinding of a kinesin from the MT increases when it encounters tau clusters [58]. Likewise, the run length is short in the presence of tau proteins [58, 149, 150]. Thus, tubulins with tau clusters are regarded as obstacles. Because the stepping motion of kinesin is realized by the diffusive motion of its head, reflective boundaries are located on the position of tau clusters when calculating the diffusive motion with the model in chapter VI. Using the same model, the increase of the unbinding probability is also quantified because the model can calculate the unbinding probability with the probability that the kinesin head contacts obstacles. Parameter on the interference between the tau clusters and the kinesin heads is provided in Appendix B.

The effect of tau proteins on the binding of floating kinesins to the MT is also considered. Dixit et al. [58] observed that the binding rate of kinesins decreases over the concentration of tau. Thus, it is assumed that unbound kinesins cannot bind to tubulins if the latter are occupied by tau clusters. Note that this is consistent with the previously mentioned hypothesis that tau clusters act as obstacle to the heads of the walking kinesin. Even if a tubulin is not occupied by tau clusters, the unbound kinesins are unlikely to bind on that tubulin if both the left and right tubulins are occupied by tau clusters because the

space is not enough for the heads to reach that site. Thus, that type of sites is also assumed inaccessible to the heads of unbound kinesins. The same restriction is applied to tubulins if both the forward and backward tubulins are occupied by tau clusters. The binding rate obtained with this assumption is similar to the experimental data [58].

7.4 Results

In this chapter, the motion of the small cargo ($r_c = 25\ \mathrm{nm}$) transported by single kinesins is investigated. The viscosity of cellular fluids acting on a particle depends on the size of the particle because the interaction between other intracellular particles and the particle affects the motion of that particle [164]. A previous experimental study revealed that the viscosity of particles in the cytoplasm of neurons increases over their diameters [165]. According to the result, the viscosity acting on the cargo used in this chapter is determined as 10 fold of the viscosity in water. The diameter (d_{ax}) of the axon is determined as 1 $\mu\mathrm{m}$ because it is the average diameter of axons in brains [166].

7.4.1 Velocity of transport

To predict the effect of MT density and the concentration of tau proteins ($[\tau]$) on the transport of cargoes, the velocity of the long transport (50 $\mu\mathrm{m}$) is calculated. The number of MTs (N_{MT}) in axons is changed from one to six because N_{MT} of one in the used axon (diameter of 1 $\mu\mathrm{m}$) approximately corresponds to the density in pathological neurons from AD patients ($1.2\ /\ \mu\mathrm{m}^2$), and the MT density with N_{MT} of six is similar to the density in healthy neurons ($7.1\ /\ \mu\mathrm{m}^2$) [167].

The velocity predicted in this model shows the following features. First, the transport velocity along the healthy axon (i.e., no excessive tau and high density of MTs, $N_{\mathrm{MT}} = 6$) is very similar to the walking velocity ($\sim$800 nm/s) of kinesins [28], as shown in Fig. 7.4 (a1). The long range transport can be delayed because the walking motion of

kinesins does not take place when they are not bound on the MTs. However, the delay is negligible in the healthy axon because the unbound kinesins can bind to one of the MTs in a very short time. Second, the changes in the transport velocity over MT density are considerable only when the axon contains a large concentration of tau, as shown in Fig. 7.4 (a). Also, the effect of $[\tau]$ on the velocity is not noticeable if the number of MTs is sufficient. Lastly, the velocity in the presence of tau proteins can be determined by the single variable m_τ (proportional to the ratio of $[\tau]$ and N_{MT}), even though the motion of the kinesins is changed by two variables ($[\tau]$ and N_{MT}). Fig. 7.4 (b1) shows that the velocities for different $[\tau]$ and N_{MT} are similar if m_τ are the same. This feature can also be observable from the strong correlation between the velocity and m_τ, as shown in Fig. 7.4 (b2). It is worth noting that the correlation between the velocity and $\widetilde{m}_\tau$ (= concentration of bound tau proteins / concentration of tubulin dimers) is not high, as shown in Fig. 7.4 (b3). Therefore, m_τ is more important than $\widetilde{m}_\tau$ when predicting the velocity. Detailed descriptions are provided in Appendix B.

7.4.2 Motion of the cargo near tau clusters

The changes of the velocity by excessive tau proteins are not noticeable unless the axon has a small number of MTs and a large concentration of tau proteins. Thus, the motion of kinesin near tau clusters is investigated to estimate the condition of MTs with the motion of kinesin. If kinesins encounter tau clusters, they bypass the cluster, or they get released from the MT. If the kinesin is unbound by the interference with tau clusters and diffuse forward, the motion of the cargo is not disturbed by the cluster anymore. However, if the cargo diffuses backward and binds to the MT, then the cargo has to repeat the above process when it encounters the tau cluster later, as depicted in Fig. 7.5 (a). As a consequence, the motion of both the kinesin and the cargo are delayed in front of tau clusters.

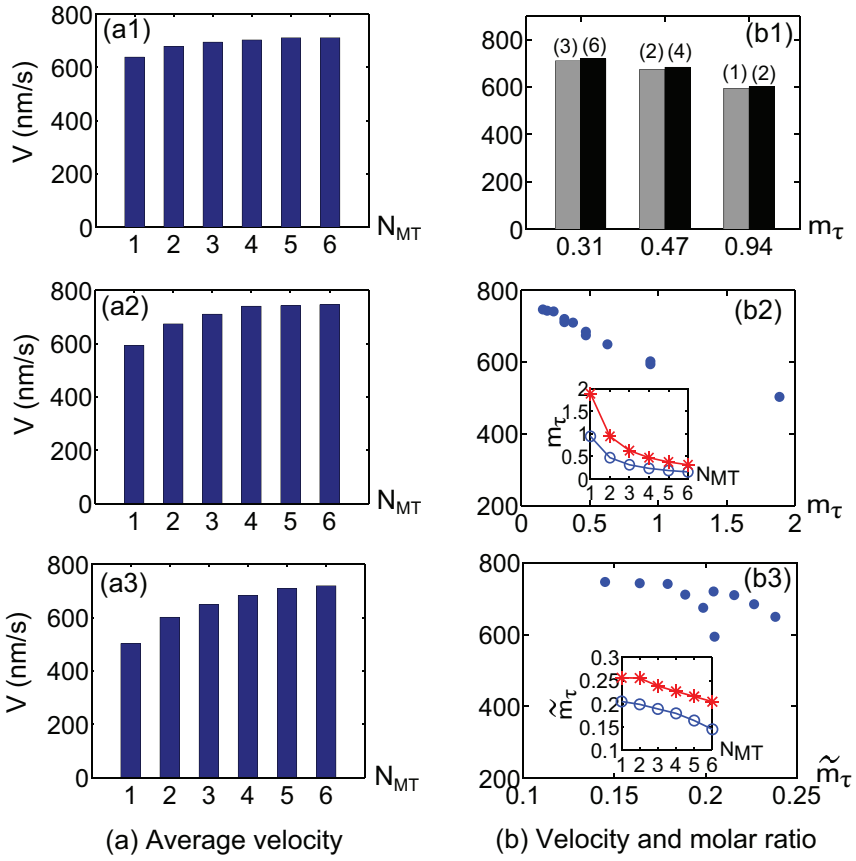

Figure 7.4: Average velocity of cargoes in the long axon. (a1) (a3) depict the average velocities for $[\tau] = 0$, 2, and 4 μM, respectively. (b1) shows the velocities in the axons with same m_τ. However, $[\tau]$ and N_{MT} of the axons are different. The velocity for $[\tau] = 2$ μM is presented by the gray bars. The black bars denote the velocity for $[\tau] = 4$ μM. The numbers in the parenthesis indicate N_{MT}. (b2) represents the velocities over m_τ. The inset graph shows m_τ of the used axons. For the inset graph, the circles and stars represent m_τ for $[\tau] = 2$ and 4 μM, respectively. (b3) shows the velocities over $\widetilde{m}_\tau$. The inset graph shows $\widetilde{m}_\tau$ of the used axons.

However, various stochastic behaviors of kinesins can also cause the regional delay in the transport. Because of this, a new metric is required to distinguish the delay originated from the tau clusters and another delay induced by the stochastic motion of kinesin. For this purpose, a large number of transports are statistically analyzed with the follow-

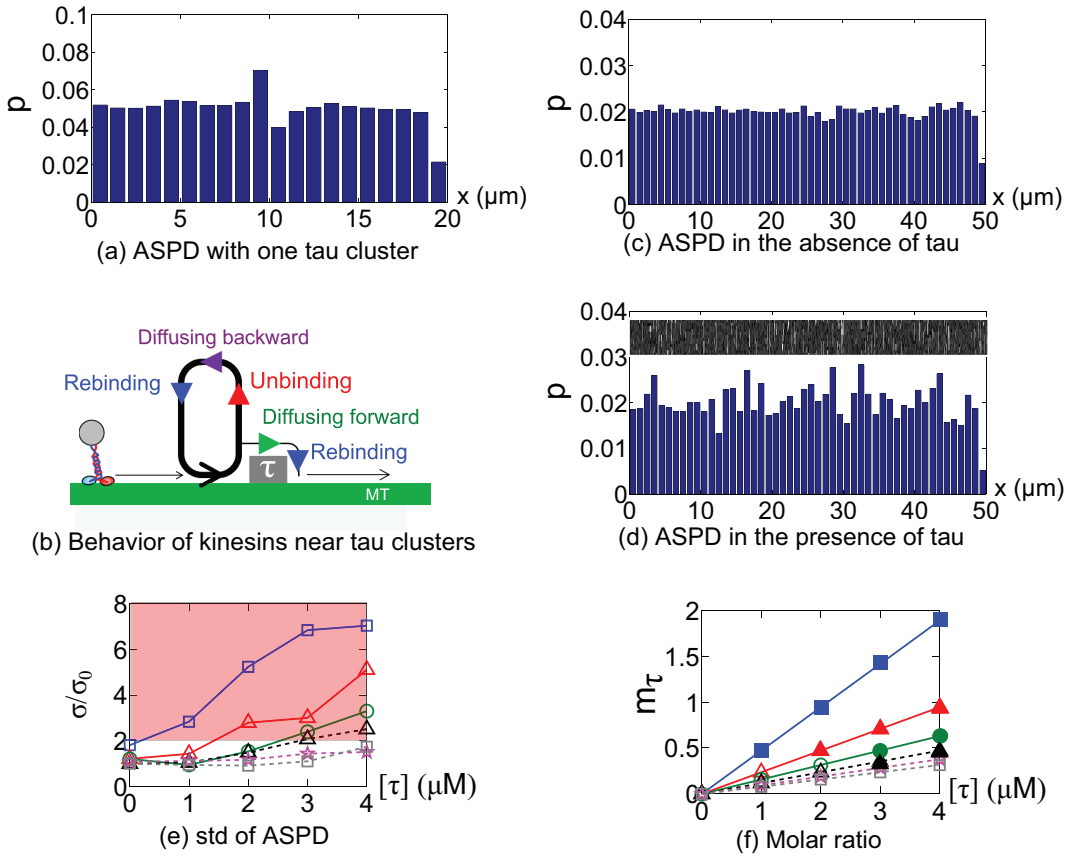

Figure 7.5: Effects of tau clusters on the motion of the cargo. (a) describes the cycle of the motion near the tau cluster. (b) shows ASPD of cargoes when tubulins at 10 μm are occupied by tau clusters. Other tubulins are free of tau proteins. (c) and (d) are the distributions for ($[\tau] = 0$ μM, $N_{\mathrm{MT}} = 6$) and ($[\tau] = 4$ μM, $N_{\mathrm{MT}} = 1$). (e) shows the normalized std. The values of std are described with the squares for $N_{\mathrm{MT}} = 1$, the triangles with the solid line for $N_{\mathrm{MT}} = 2$, circles with the solid line for $N_{\mathrm{MT}} = 3$, triangles with the dotted line for $N_{\mathrm{MT}} = 4$, stars with the dotted line for $N_{\mathrm{MT}} = 5$, and squares with the dotted line for $N_{\mathrm{MT}} = 6$. (f) shows m_τ for the used axons.

ing procedure. First, the position of the cargo is captured with the constant sampling time (0.1 s). Then, the position of the cargo in the captured images is classified with 1 μm interval. This creates the spatial probability distribution of the position. By using 200 sets of transports, 200 sets of distributions are obtained. Next, the averaged spatial probability

distribution (ASPD) is calculated by averaging the 200 sets of distributions. The delay caused by stochastic motion of kinesin is not included in ASPD because it is canceled out by averaging the probability distributions. ASPD indicates the time when the cargoes stay in each section along the axon. If there are no spatial changes in the properties affecting the motion of cargoes (i.e., viscosity, temperature, diffusivity, or ATP concentration) along the axon, the cargoes spend equal time on each section in the axon. Then, ASPD has to be spatially uniform, otherwise, ASPD fluctuates along the axis of axons.

To reveal the effect of tau clusters, tau proteins are positioned on the tubulins at 10 μm. Every other tubulin has no bound tau proteins. The ASPD increases in front of the cluster and decreases behind the cluster, as shown in Fig. 7.5 (b). In the absence of tau proteins, ASPD is almost uniform over the axon, as shown in Fig. 7.5 (c). This indicates that no acceleration or delay is occurred in any particular location. When tau clusters are developed on the MTs, ASPD fluctuates over the axon, as shown in Fig. 7.5 (d).

The std of ASPD is calculated to quantify its fluctuation. Then, the obtained std is normalized by the std corresponding to healthy axons (i.e., $N_{\mathrm{MT}} = 6$ and $[\tau] = 0$ μM), as shown in Fig. 7.5 (e). The result is surprising because the changes in std by $[\tau]$ and N_{MT} are significantly large compared to the changes in the transport velocity depicted in Fig. 7.4. This strong dependency of ASPD on $[\tau]$ and N_{MT} can be used to estimate the condition of MTs in the axon more effectively.

7.4.3 Cargo traffic in axon

When a large number of cargoes need to be transported to synapses, the transport is predicted by considering the following interaction between different kinesins and between different cargoes. First, the interference between walking kinesins are taken into account using the model described in chapter VI because it characterized the stepping motion of

kinesin when other kinesins are nearby. Second, effects of a bound kinesin and its cargo on an unbound kinesin are incorporated into the model by preventing the unbound kinesin from landing on the tubulins around the bound cargo, as depicted in Fig. B.4. Third, the interaction between unbound cargoes can be considered by using different viscosity when calculating the Brownian motion of the unbound cargoes. The change in the viscosity depends on the ratio between the sum of volumes of cargoes in the axon and the volume of the axon. The volume ratio is less than 0.5 $\%$ for the number of cargoes used in this chapter ($<$ 250). In previous studies [168], the increase in the viscosity by this level of volume fraction is very small ($< 10\ \%$). Thus, the effect of interaction between cargoes is assumed as negligible.

To realize the traffic of the transport, kinesins (which are attached to cargoes) are supplied near the minus-end of MTs with constant rate ($\dot{c}_{\mathrm{in}}$). Then, the number of cargoes (c_{axon}) in the observing volume (i.e., 0 to 5 $\mu\mathrm{m}$ in the axon with a single MT) is captured over time. The changes in the traffic of cargoes over time are depicted in Fig. 7.6 (a). In the beginning ($t <$ 10 s), the number of cargoes in the observing volume increases with the constant rate ($\dot{c}_{\mathrm{in}}$). During $10 < t <$ 20 s, c_{axon} keeps increasing, but its rate of change decreases over time because some cargoes flow out toward the synapse with the rate $\dot{c}_{\mathrm{out}}$. When $t >$ 20 s, the rate of change in c_{axon} is constant over the time. c_{axon} does not change over time if the axonal transport system is able to transfer cargoes with the rate $\dot{c}_{\mathrm{in}}$. Otherwise, c_{axon} increases over time with a constant rate (i.e., $\dot{c}_{\mathrm{in}} - \dot{c}_{\mathrm{out}}$). In the absence of excessive tau proteins, the axon can transport cargoes toward synapses with no increase in the traffic if $\dot{c}_{\mathrm{in}} \leq 10\ \mathrm{s}^{-1}$, as shown in Fig. 7.6 (b). If $[\tau]$ is larger than 2 $\mu\mathrm{M}$, the cargoes are accumulated in the axon if $\dot{c}_{\mathrm{in}} \geq 5\ \mathrm{s}^{-1}$.

The averaged spatial concentration distributions (ASCD) of cargoes are calculated using the spatial concentration distributions obtained with constant time sampling time. The

method to acquire ASCD is similar to that of ASPD. In the presence of tau protein, ASCD is also fluctuated, as shown in Fig. 7.6 (c). This result suggests that the regional traffic jams of the cargoes are generated by tau clusters. The std is normalized with the values of std in the absence of tau proteins. The normalized std increased significantly by excessive tau proteins, as shown in Fig. 7.6 (d). Also, the number of regions of the traffic congestion can increase as more cargoes are injected into the axon. Because the delayed transport caused by tau clusters (described in Fig. 7.5 (a)) can also be realized by the interaction between walking kinesins and by the interference between the bound cargoes and unbound cargoes, the normalized std for high $\dot{c}_{\mathrm{in}}$ is large.

7.5 Conclusions

In this chapter, a new model capable of predicting the complex motion of kinesins is developed to predict the effect of tau proteins on the long axonal transport. Kinetics such as chemical reactions, the effects of force on the chemical reactions, and electrostatic interactions among kinesins, tubulins, and tau proteins, determine the kinesin mediated transport. These kinetics are characterized by fitting the results of the model to the experimental data. By using this model, the transport along the axons with small/large number of cargoes is studied. The results on the transport with small number of cargoes show that both low density of MTs and large concentration of tau are required to cause considerable degradation of the transport. In the axons with a large number of cargoes, the interaction between cargoes changes the transport. The accumulation of the cargoes in the axon is predicted when the inflow rate of cargoes to the axon is large. In addition, the cargoes can be accumulated even for small inlet flux if there are excessive tau proteins in the axon.

The regional traffic jam (or delay) can be useful to monitor the condition of MTs due to its high sensitivity to the concentration of tau proteins and to the MT density. The

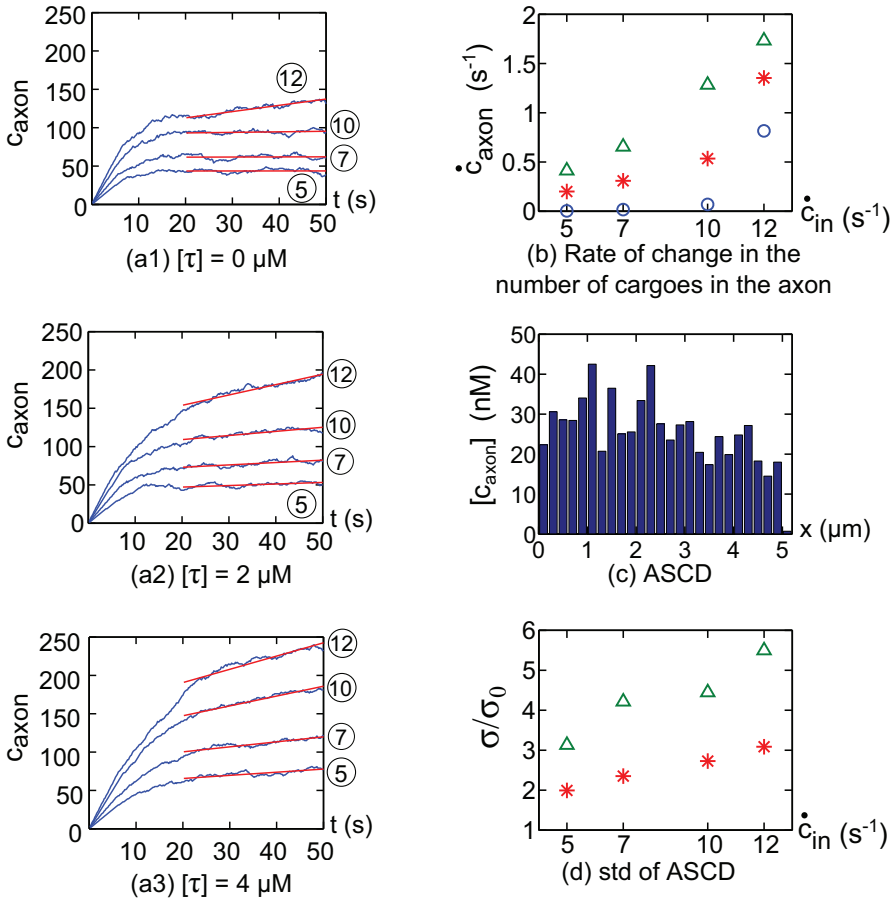

Figure 7.6: Transport of a large number of cargoes. (a) shows c_{axon} over time for $[\tau] = 0$, 2, and 4 μM for (a1) (a3), respectively. The numbers in circles represent $\dot{c}_{\text{in}}$. N_{MT} is 1 for every axon. (b) denotes the rate of c_{axon} between 20 and 50 s. Circles, stars, and triangles denote the rate for $[\tau] = 0$, 2, and 4 μM, respectively. (c) depicts ASCD for $\dot{c}_{\text{in}} = 5\ \text{s}^{-1}$ and $[\tau] = 4\ \mu$M. (d) represents the normalized std.

changes in the normalized std of ASPD (or ASCD) are much larger than the decrease of the velocity. For example, when $N_{\text{MT}} = 2$ and $[\tau] = 2\ \mu$M, the velocity is decreased by 5 % compared to the velocity along a healthy axon ($N_{\text{MT}} = 6$ and $[\tau] = 0\ \mu$M). However, the std of ASPD is increased to 2.8 folds of the value corresponding to a healthy axon. This strong dependency of ASPD on $[\tau]$ and N_{MT} can be used to estimate the condition of MTs in the axon more effectively.

Another advantage of the regional traffic jam is that it can be observed with relatively low precisions or resolutions. One can measure the binding rate, the unbinding rate, or the run length of the kinesin to estimate the condition of MTs. However, a high temporal resolution is required to capture the instants of the binding and unbinding of kinesins. Kinesins can unbind in a short time (order of 0.1 s). In addition, the timescale for the binding is very short (order of 0.01 s) in the absence of tau. Thus, a high temporal resolution (< 0.01 s) is necessary to detect the changes in the binding and unbinding. Also, the run length of kinesins is in the order of 100 nm. Thus, single particle tracking techniques with high precisions ($<$ 100 nm) are needed to detect the changes in the run length. However, it could be challenging to track the position of cargoes along the long axons with this level of high precisions due to noise and pixel size of images. Moreover, those quantities are not proper variables for the diagnosis of neurons because the binding or unbinding rate can be very different depending on the types of neurons, as well as over their state of health. However, ASPD or ASCD can be obtained with relatively low temporal resolution and spatial precision. For example, our model predicts the significant changes in ASPD by tau proteins with the resolution of 0.1 s and the precision of $1\ \mu\mathrm{m}$.

Abnormal axonal transport can take place in the neurons of patients suffering from the early stage of AD. The tau aggregated structures in the cytoplasm of the neurons are regarded as a bio-marker for AD because they are discovered from the neurons of patients in a late stage of AD. However, the results of an *in vivo* experiment performed by Mandelkow et al. [46] suggests that the intracellular transport system can be degraded before tau proteins unbind from MT and aggregate into neurofibrillary tangles. If dysfunctional transport is prior to the formation of the tangles, detecting the behavior of kinesins near tau clusters can be one possible diagnosis strategy for the early AD in the future where imaging technologies can locate particles in the brain.

CHAPTER VIII

Conclusions

8.1 Dissertation Contributions

A new mechanistic model was developed to capture several key components of the physics involved in the motion of kinesin; dynamic motion, chemical kinetics, fractional Gaussian noise in viscoelastic fluids, stochastic binding to the MTs, stochastic unbinding from the MTs, and thermally fluctuating motion of the kinesin free head (which causes backward and/or sideway steps). The verification on the model was also performed using experimental observations. Then, the complex long range axonal transport by kinesins and its degradation by tau proteins were investigated with the new model.

The studies on the effects of fluids on the transport provide new insights on the motion of kinesin when kinesins move in a fluid which has different properties compared to water. First, the dependence of the kinesins motion on the load is modified by the viscosity of the fluid. When single kinesins transport the cargo in a fluid with low viscosity, its force-velocity curve can be divided into two regimes. When the resisting load is not considerable (i.e., less than 4 pN), the changes in the velocity by the load is not significant. If the load is larger (than 4 pN), the velocity decreases noticeably as the load increases. However, this nonlinear relation changes into a linear one when the viscosity of the fluid is considerable. Also, the change in the velocity due to the elasticity which originates from

particles in the fluid (e.g., long polymers) is predicted. The effects of the total friction and the ratio of viscosity and elasticity on the motion of kineisns are studied. As expected, the results show that the velocity reduces as the total friction increases. Also, for a given total friction, the kinesin can move with high speed when the fluid has similar viscosity and elasticity. This latter result is intriguing because cellular fluids have similar ratio of viscosity and elasticity.

The binding, unbinding and backward motion of kinesins allow an effective collective transport. First, the binding of kinesins to MTs occurs in a short time compared to the unbinding. This fast binding process decreases the probability that every kinesin on the cargo unbinds from the MT. Thus, the run length of the cargo increases remarkably over the number of kinesins. Second, when large loads are applied, the leading kinesin behaves like an anchor which increases the chances of the other kinesins to bind to the MT. This mechanism improves the reliability of long transport by reducing the possibility that the cargo drifts away from the MT due to the transient large loads. Third, the thermal fluctuation of unbound kinesins affects the velocity of cargoes. The unbound kinesins can bind in front of the cargo or behind the cargo. Together with the unbinding of kinesins, these stochastic binding processes cause additional movements of the cargo. For assisting loads, the velocity of the cargo transported by several kinesins is larger than the velocity when the cargo is transported with single kinesins. For resisting loads less than 6 pN, the collective transport is slower than the transport performed by single kinesins. Next, when a large resisting load (i.e., larger than 6 pN) acts on the cargo, kinesins tends to work more cooperatively. The motion of leading kinesins is regulated by the dependency of the chemical reaction of kinesins on the force, and by frequent backward steps for large resisting forces. Thus, the lagging kinesins move faster than the leading kinesins. As a consequence, the load acting on the cargo is more fairly distributed over bound kinesins. Thus, this behavior

prevents fast unbinding of leading kinesins, and hence more kinesins can participate in the transport. Therefore, the velocity of the collective transport is larger than the velocity of kinesin itself for large resisting loads.

The dynamics of kinesins which share the same MT with static proteins or with other moving motors were captured by considering two dimensional motions of the kinesin free head. First, it was predicted that both velocity and run length of kinesins are reduced when static obstacles are located on the MT. The movement of kinesins along the axial direction of the MT can be delayed when several obstacles are located in front of the kinesins. Because kinesins determine the direction of the next step stochastically, they have to repeat several side steps until they randomly select a path to bypass the obstacles. Also, the interference between the static obstacles and kinesins increases the probability of the kinesins to unbind from MTs. It is worthy to note that the decrease in the run length is more significant than the change in the velocity. Next, the velocity of kinesins is obtained when other motors walk along the same MTs. If all motors walk in the same direction, the changes in the velocity are negligible until the MT is considerably crowded with motors. When kinesins walk with other types motors (i.e., walking to the minus end of MTs), a noticeable decrease in the velocity is predicted. However, the effect of static obstacles is more prominent than that of motors walking to the opposite direction.

The degradation of the axonal transport by excessive tau proteins was investigated because it is believed to be one possible cause of AD [46–50]. The velocity of the transport does not change noticeably in the absence of a considerable decrease in the number of MTs and a significant amount of tau proteins. This robustness of the axonal transport is beneficial for neurons. However, this robustness makes it difficult to use the velocity as a quantity to detect excessive tau proteins or to estimate the density of MTs in axons before the MTs are significantly damaged. Thus, the regional traffic jams (or delays) near tau

clusters predicted from our model open the door to alternative detection methods. The new statistical metrics introduced in this dissertation reveal that the quantitative change in the traffic jams by the number of MTs or by the concentration of tau proteins is considerable. Also, these metrics can be useful because they can be used to detect traffic jams with a resolution of the order of a micrometer, which is very large considering that the step size of kinesins is only 8 nm.

8.2 Future Research

Directions for future research include experimental validation on the results obtained from the model in long range transport. For example, measurements of the changes in the velocity over the concentration of excessive tau and the size of the cargo could be used for future validations. Also, theoretical and experimental studies of the effect of perturbations (e.g., magnetic forces, electric forces, ultrasonic waves, etc.) on the transport could be performed.

APPENDICES

APPENDIX A

Motion of kinesins in the presence of obstacles

A.1 Stretching of the kinesin structure

The force acting on the free head (i.e., F_x and F_y in Eq. (6.1)) is calculated by considering three different forces; the forces acting on the UDNL (F_{DCNL}), on the DCNL (F_{UDNL}) and the force transferred from the cargo to the neck via the cargo linker (F_{c}). For a given position of the free head, the neck is located on the position these forces are balanced. F_{DCNL} and F_{UDNL} are calculated by using the WLC as

$$F_{\mathrm{NL}} = \frac{k_B T}{\ell_p}\left(\frac{1}{4}\Big(1-\frac{\ell_{\mathrm{NL}}}{\ell_c}\Big)^{-2} + \frac{\ell_{\mathrm{NL}}}{\ell_c} - \frac{1}{4}\right), \qquad \text{(A.1)}$$

$$\text{where } \ell_c = N_{AA}\,\ell_a = (N_{AA,0} + 3.5\,n_{\mathrm{uw}})\,\ell_a,$$

where k_B is Boltzmann constant, and T (=300 K) is the absolute temperature. ℓ_p (=0.6 nm) is the persistence length, and ℓ_a (=0.4 nm) is the contour length between two adjacent AAs. ℓ_c is the contour length of the NLs. N_{AA} denotes the number of AAs in the NLs, and $N_{AA,0}$ is that number when every bond in the neck is intact. $N_{AA,0}$ is 14 for the UDNL and 4 for the DCNL. n_{uw} is the number of unwound turns of the neck.

The procedure begins with the state where every chemical bond between two coils of the neck is connected. Thus, n_{uw} is set as zero. The moment caused by F_{c} on the neck

is negligible because F_{c} acts on the center of the neck. The two coils align along a line which is indicated with the dotted line in Fig. A.1, so that the moments caused by F_{UDNL} and F_{DCNL} are balanced. It is assumed that the bonds of the neck can be disconnected by the force (F_{UW}) which acts along that dotted line. Note that F_{UW} is obtained by summing F_{UDNL}, F_{DCNL}, and F_{c}. If F_{UW} is less than the force required to unwind the first bond of the coiled-coil structure, F_x and F_y are determined by F_{UDNL}. If the calculated F_{UW} is larger than the force to unwind the first bond, the whole steps are performed again with the neck in which the first turn is unwound (i.e., $n_{\mathrm{uw}} = 1$). This procedure is repeated until F_{UW} becomes less than the force required to unwind the remaining turn. The magnitude of force required to disconnect each turn of the neck is obtained from the previous experiment [67].

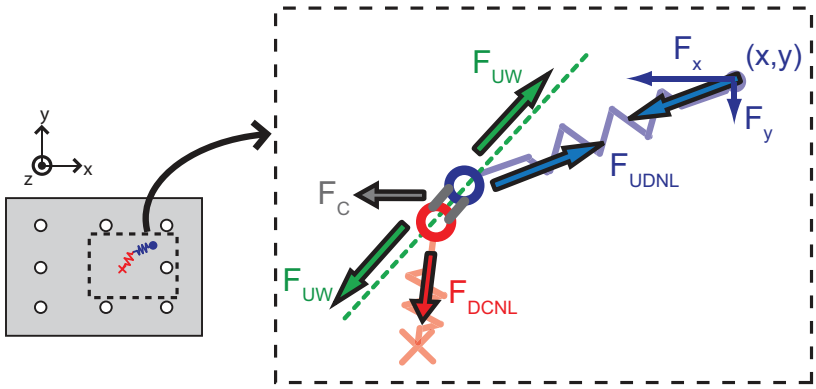

Figure A.1: Forces acting on the neck. Two circles linked by two lines denote the coils of the neck. The neck is connected to two springs corresponding to the DCNL and UDNL.

A.2 The effect of unwinding of the neck and binding with tilted posture

To check the effect of the unwinding of the neck on the diffusion, $P_{b,i}$ is obtained using the model that does not allow the unwinding. The equation used to calculate F_{NL} is the

same with Eq. (A.1) except the value of N_{AA} is fixed as $N_{AA,0}$. The effect of binding with tilted posture is also studied by preventing the binding with tilted posture. The binding probability shown in Tab. A.1 suggests that both the unwinding and binding with a tilted posture are necessary to obtain $P_{b,i}$ measured in the experiment.

Site	Experiment	$\mathrm{U_{on}} + \mathrm{T_{on}}$	$\mathrm{U_{off}} + \mathrm{T_{on}}$	$\mathrm{U_{on}} + \mathrm{T_{off}}$
(4) or (5)	0.0195	0.0193	7×10^{-5}	0.021
(6) or (8)	0.0455	0.0452	1.2×10^{-6}	0.00169
(7)	0.869	0.871	0.99	0.954

Table A.1: Binding probability ($P_{b,i}$) to each site for various models. $\mathrm{U_{on}} + \mathrm{T_{on}}$ indicates the model which allows both the unwinding of the neck and the binding with a tilted posture. $\mathrm{U_{off}} + \mathrm{T_{on}}$ represents the model incapable of unwinding of the neck. $\mathrm{U_{on}} + \mathrm{T_{off}}$ refers to the model in which its head cannot bind with a tilted posture.

A.3 Binding sites occupied by kinesins

The number of binding sites occupied by a single kinesin molecule depends on its chemical state. After the kinesin takes a step, one head has ATP and the other head has no nucleotide. Both heads are strongly bound to the MT because the kinesin head has a strong affinity to the MT when it has ATP or no nucleotide [169]. Thus, two sites are occupied by the kinesin for this state, as shown in Fig. A.2-(a1). Then, ATP in the head is hydrolyzed into adenosine diphosphate and inorganic phosphate. When the inorganic phosphate is released from the head, the head is unbound and diffuses around the other head which is still strongly bound to the MT [70, 71]. For this state, the strongly bound head (i.e., head with no nucleotide) occupy a single site. It is plausible that the site affected

by the unbound head is symmetric about the bound head, as shown in Fig. A.2-(a2). Thus, several possible sets of binding sites affected by the fee head are studied for this state, as shown in Fig. 6.5. Because the unbound head does not remain in one site, the unbound heads of several kinesins can share the same site, as shown in Fig. A.2-(b1). However, the head cannot bind to a site if the site is affected by the unbound head of other kinesins, as shown in Fig. A.2-(b2).

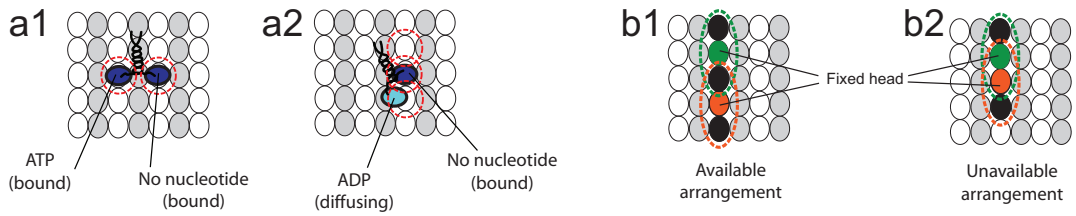

Figure A.2: Binding sites occupied by kinesins. (a1) shows that two sites are occupied by the kinesin when its two heads are strongly bound. The circles with dots represent the sites occupied by the kinesin heads. (a2) depicts the kinesin when one of the heads is not bound and the other head is strongly bound. (b) demonstrates the two examples when occupied sites of two kinesin molecules are overlapped. Both kinesins have one unbound head and one bound head. The black filled circles represent the sites occupied by the diffusing heads.

A.4 The number of unmovable kinesins on the MTs

The data of the previous experiment of Telley et al. [59] is used to determine parameters ($R_{\rm obs}$, $m_{\rm obs}$, and $P_{\rm ub,cnt}$) of our model. In the experiment, they measured the light intensity of MTs as increasing the concentration of fluorescently labeled unmovable kinesins until the intensity saturated. Then, they observed the motion of kinesin on the MTs which have 8 $\%$ light intensity compared to the saturated intensity.

To obtain the number of unmovable kinesins used in the experiment, we randomly distributed the unmovable kinesins until the MT is saturated with the unmovable kinesins.

The behavior of the unbound head, which can share binding sites with other kinesins, is also considered. When the MT is saturated with unmovable kinesins, the molar ratio of the unmovable kinesins and tubulin dimers (ρ) is calculated as 0.4352 for $m_{\rm obs} = 3$, 0.3572 for $m_{\rm obs} = 5$, and 0.1843 for $m_{\rm obs} = 9$. When comparing the velocity of the model to the experimental result, the unmovable kinesins of $\rho = 0.0346\ (= 8\% \times 0.4352)$, $0.0286\ (= 8\% \times 0.3572)$, and $0.0147\ (= 8\% \times 0.1843)$ are used for $m_{\rm obs} = 3$, 5, and 9, respectively.

A.5 Deterministic model

The mean velocity and run length in the presence of static obstacles can be approximated by using the motion of kinesin when the obstacles are ahead of the kinesin (i.e., (6), (7), and (8) in Fig. 6.3-(b3)). The obstacles at those sites have considerable effects on kinesin because the free head mostly diffuses near the forward sites.

The velocity is determined by the average time (T_d) between steps of the kinesin and average moving distance along the x axis per step ($d_{\rm step}$) of the kinesin. $d_{\rm step}$ is equal to $8\frac{N_{\rm fw}}{N_{\rm tot}}$ where $N_{\rm tot}$ and $N_{\rm fw}$ are the average of the total number of steps and the average number of steps to forward sites (i.e. (6), (7), and (8) in Fig. 6.1-(c)), respectively before the kinesin unbinds from the MT. Thus, the velocity is calculated as

$$V = \frac{d_{\rm step}}{T_d} = \frac{8\ N_{\rm fw}}{N_{\rm tot}}\ \frac{1}{T_d}. \tag{A.2}$$

Because $N_{\rm fw}$ is almost the same with $N_{\rm tot}$ in the absence of obstacles, the velocity in the absence of obstacles (V_0) can be calculated as $\frac{8}{T_d}$. T_d is the sum of the time for the stepping motion and the time for the chemical reaction. The effect of the obstacle on the chemical reaction can be assumed as negligible. Also, the time for the stepping motion is very short compared to the time for the chemical reaction. Therefore, the value of T_d in the presence of obstacles is similar to the value in the absence of obstacle. Thus,

the ratio of the velocity in the presence and in the absence of obstacles can be obtained as $\frac{V(\rho)}{V_0} = \frac{1}{N_{\rm tot}(\rho)/N_{\rm fw}(\rho)}$. The denominator can be approximated to the average number of steps required to proceed 8 nm along the x axis. Thus, the ratio of velocities can be obtained as

$$\frac{V(\rho)}{V_0} = \frac{1}{\sum_{i=1}^{q} p_{{\rm obs},i}(\rho)\ n_{\rm step,i} + \left(1 - \sum_{i=1}^{q} p_{{\rm obs},i}(\rho)\right)}, \tag{A.3}$$

where $p_{{\rm obs},i}$ is the probability to encounter obstacles with a specific arrangement. Examples of $p_{{\rm obs},i}$ are shown in Fig. A.3 (a). Note that the terms of i from 1 to $m_{\rm obs}$ correspond to the kinesin confronting a single obstacle, and the terms of i from $m_{\rm obs}+1$ to $2m_{\rm obs}$ are for the kinesin confronting two series of obstacles. Tab. A.2 shows the number of steps ($n_{\rm step,i}$) corresponding to $p_{{\rm obs},i}$. Note that the obstacles of $m_{\rm obs} = 3$, 5, and 9 occupy three binding sites along the y axis, as shown in Fig. 6.5. Thus, the same $n_{\rm step,i}$ is used.

$m_{\rm obs}$	$R_{\rm obs}$	$n_{\rm step,1}$	$n_{\rm step,2}$	$n_{\rm step,3}$
1	4	1.35	-	-
1	5	1.56	-	-
3, 5, or 9	4	2.01	3.04	2.01
3, 5, or 9	5	2.73	3.68	2.73

Table A.2: The parameters of the deterministic model.

The run length along the x axis is $8N_{\rm fw}$ which is equal to $8\frac{N_{\rm fw}}{N_{\rm tot}}N_{\rm tot}$. $N_{\rm tot}$ is the same as the inverse of the unbinding probability per step (i.e., $N_{\rm tot} = \frac{1}{P_{ub}}$) [59]. Thus, the run

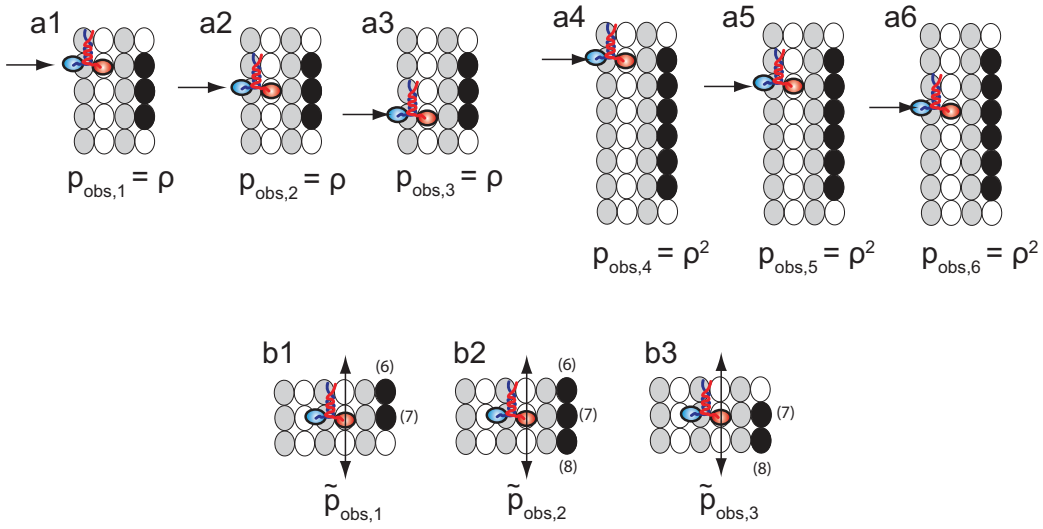

Figure A.3: The kinesin with obstacles of $m_{\rm obs} = 3$. (a) is shown to explain the probability that the kinesin encounter obstacles ($p_{{\rm obs},i}$). (a1)-(a3) show several situations where the kinesin confronts single obstacles. The corresponding probabilities $p_{{\rm obs},1-3}$ are provided below. (a4)-(a6) depict situations where the kinesin encounters two series of obstacles. The corresponding probabilities $p_{{\rm obs},4-6}$ are also provided. (b) is shown to explain the probability that the kinesin interact with obstacles with the specific arrangement ($\widetilde{p}_{{\rm obs},i}$).

length is calculated as

$$RL = 8\frac{N_{\rm fw}}{N_{\rm tot}}N_{\rm tot} = 8\frac{N_{\rm fw}}{N_{\rm tot}}\frac{1}{P_{ub}}, \tag{A.4}$$

Again, $N_{\rm fw}$ is almost the same with $N_{\rm tot}$ in the absence of obstacles. Therefore, the ratio of the run length can be obtained as

$$\begin{aligned}\frac{RL(\rho)}{RL_0} &= \frac{N_{\rm fw}(\rho)}{N_{\rm tot}(\rho)}\frac{P^0_{\rm ub}}{< P_{\rm ub}(\rho) >} \\ &= \frac{V(\rho)}{V_0}\frac{P^0_{\rm ub}}{\sum_{i=1}^{3} p_{ub,i}\,\widetilde{p}_{\rm obs,i} + P^0_{\rm ub}(1-\sum_{i=1}^{3}\widetilde{p}_{\rm obs,i})},\end{aligned} \tag{A.5}$$

where $< P_{\rm ub}(\rho) >$ is the average unbinding probability per step in the presence of the obstacles. Note that $< P_{\rm ub}(\rho) >$ is different from $P_{\rm ub}$ in Eq. (6.2). $P_{\rm ub}$ represents the unbinding probability of when obstacles are near the kinesin. $< P_{\rm ub}(\rho) >$ is the averaged

unbinding probability which considers both the situation when obstacles are located near the kinesin and the other situation when there is no obstacle around the kinesin. $p_{\mathrm{ub},1-3}$ are the unbinding probabilities per step corresponding to $\widetilde{p}_{\mathrm{obs},1-3}$. The value of $p_{\mathrm{ub},1-3}$ can be calculated with Eq. (6.2). $\widetilde{p}_{\mathrm{obs},i}$ is the probability that two or three sites in front of the kinesin are occupied by obstacles, as shown in Fig. A.3-(b). $\widetilde{p}_{\mathrm{obs},i}$ can be calculated as

$$\begin{aligned}
\widetilde{p}_{\mathrm{obs},1} &\simeq \frac{1}{3}\sum_{i=1}^{3} p_{\mathrm{obs},i}\; n_{\mathrm{step},i} + \frac{1}{6}\sum_{i=4}^{9} p_{\mathrm{obs},i}\; n_{\mathrm{step},i}, \\
\widetilde{p}_{\mathrm{obs},2} &\simeq \frac{1}{3}\sum_{i=1}^{3} p_{\mathrm{obs},i}\; n_{\mathrm{step},i} + \frac{2}{3}\sum_{i=4}^{9} p_{\mathrm{obs},i}\; n_{\mathrm{step},i}, \\
\widetilde{p}_{\mathrm{obs},3} &\simeq \widetilde{p}_{\mathrm{obs},1},
\end{aligned} \tag{A.6}$$

where $\sum_{i=1}^{3} p_{\mathrm{obs},i}\; n_{\mathrm{step},i}$ is the probability that the kinesin interacts with single obstacle. Thus, the probability that the binding sites (6) and (7) are occupied by single obstacles can be approximated as $\frac{1}{3}\sum_{i=1}^{3} p_{\mathrm{obs},i}\; n_{\mathrm{step},i}$. With the same method, the probability that the binding sites (6) and (7) are occupied by two series of obstacles is $\frac{1}{6}\sum_{i=4}^{9} p_{\mathrm{obs},i}\; n_{\mathrm{step},i}$.

The consideration on single obstacles is sufficient when fitting the deterministic model to the previous experiment because the density of the obstacles in the experiment is small. If the density of obstacles increases, the kinesin is also likely to confront two series of obstacles. Thus, the effect of single and two series of obstacles are incorporated into the model to calculate the velocity and run length, which are shown in Fig. 6.6. $n_{\mathrm{step},4-6}$ for the unmovable kinesins are obtained as 4.16, 8.43, and 10.1 from the diffusion model. By symmetry, $n_{\mathrm{step},7-9}$ is the same with $n_{\mathrm{step},6-4}$. With these $n_{\mathrm{step},4-9}$, the values of coefficients of Eq. (6.4) and Eq. (6.5) are obtained as $a_1 = 7.04$, $a_2 = 25.29$, $b_1 = 24.28$, and $b_2 = 60.04$ by using Eq. (A.3) and Eq. (A.6).

A.6 Stochastic model

To capture the stochastic motion of kinesins, the diffusion model of chapter VI is integrated with the mechanistic model in chapter IV. The probability of the direction of the step and the increase of the unbinding probability by obstacles are calculated by using the diffusion model. The mechanochemical cycle and the unbinding probability of the kinesin are captured using the model presented in chapter II and IV. These several dynamics of kinesins (state transition in the mechanochemical cycle, unbinding from the MT and direction of step) are stochastic processes. Thus, they are determined by comparing the calculated probabilities with the random number. To perform Monte-Carlo simulation, new random numbers are generated at every step.

The model described in chapter II-V do not consider the side steps. Thus, the parameters are modified with small changes for the studies of chapter VI and VII to include the effect of side steps. Tab. A.3 shows the modified values of parameters.

The stochastic model can be used to obtain exact values of $P_{\mathrm{ub,cnt}}$. In the previous experiments which studied the effect of unmovable kinesins on the walking kinesins, the displacement of kinesin is captured at every 0.1 s, and their spatial resolution is 40 nm. Thus, this time and spatial resolution are applied to the stochastic model when calculating $P_{\mathrm{ub,cnt}}$.

A.7 The motion of kinesin with other motors

The unmovable kinesins stay on the MT with the state when one head is bound and the other head is not bound. This state is same with the state of walking kinesins as they wait for ATP to attach. Thus, the interference between walking kinesins and the unmovable kinesins can be applied to the interaction between walking kinesins. The minus-end directed motors are considered in this model by reversing the direction of steps of the kinesin.

Parameter	Value	Unit
k_{1f}	2.83	$\mu\mathrm{M}^{-1}\mathrm{s}^{-1}$
$k_{1b,0}$	26.5	s^{-1}
k_{2f}	108.7	s^{-1}
Φ_c	1.295	nm
κ	4.837	$\mathrm{pN/nm}$
$k_{D0,0}$	0.0285	s^{-1}
$P_{D1,0}$	0.00934	probability
d_0	0.043	nm
d_1	0.851	nm

Table A.3: The values of parameters of the mechanistic model.

APPENDIX B

Motion of kinesins in the presence of tau

B.1 Binding rate of kinesins on MT

The value of the parameter in regard to binding ($\dot{p}_{\mathrm{reb}}$) is obtained by comparing the binding rate calculated from the model and previous experimental data in the absence of tau proteins. Gilbert et al. [76] mixed free kinesins and MTs to measure the concentration of kinesins bound to the MTs over time. Then, they calculated the binding rate of kinesins for various concentrations of tubulins. To calculate binding rate from the model, one MT is located at the center of the cylinders. The volume of the cylinder is determined so that the concentration of the tubulins in the cylinder is the same with the concentration used in the experiment. Then, the average binding rate is obtained by considering the binding rates of the kinesins spreading in the cylinders. The binding rate calculated from the model is similar to the measured values in the experiment for various concentrations of tubulins for $\dot{p}_{\mathrm{reb}} = 7.1 \times 10^5\ \mathrm{s}^{-1}$, as shown in Fig. B.1.

B.2 Binding of tau proteins on MT

The probability of tau to bind to the MT is determined with the single molecule kinetics as

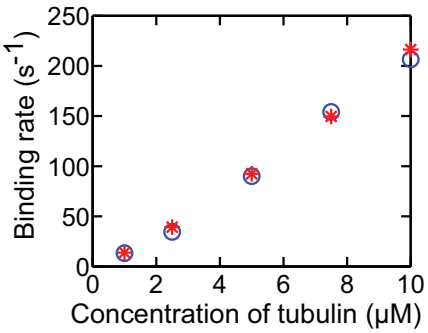

Figure B.1: Binding rate of kinesins to MTs. The circles represent the experimentally observed binding rate. The rate calculated from the model is denoted with asterisks.

$$
\begin{aligned}
P_\phi &\overset{k_1^+[\mathrm{TUB}_1]}{\underset{k_1^-}{\rightleftharpoons}} P_{\mathrm{MT}+\tau,1}, \\
P_\phi &\overset{k_2^+[\mathrm{TUB}_2]}{\underset{k_2^-}{\rightleftharpoons}} P_{\mathrm{MT}+\tau,2}, \\
P_\phi &\overset{k_3^+[\mathrm{TUB}_3]}{\underset{k_3^-}{\rightleftharpoons}} P_{\mathrm{MT}+\tau,3},
\end{aligned}
\tag{B.1}
$$

where P_ϕ is the probability that the tau protein is unbound. $P_{\mathrm{MT}+\tau,1-3}$ are the probabilities that the tau protein binds to tubulins TUB_{1-3}. $[\mathrm{TUB}_{1-3}]$ are the concentrations of TUB_{1-3}. k_{1-3}^+ are the binding rate constants, and k_{1-3}^+ are the unbinding rate constants. Then, the probabilities at equilibrium can be calculated with the following equations.

$$
\begin{aligned}
\frac{d}{dt}P_{\mathrm{MT}+\tau,1} &= k_1^+[\mathrm{TUB}_1]P_\phi - k_1^- P_{\mathrm{MT}+\tau,1} = 0, \\
\frac{d}{dt}P_{\mathrm{MT}+\tau,2} &= k_2^+[\mathrm{TUB}_2]P_\phi - k_2^- P_{\mathrm{MT}+\tau,2} = 0, \\
\frac{d}{dt}P_{\mathrm{MT}+\tau,3} &= k_3^+[\mathrm{TUB}_3]P_\phi - k_3^- P_{\mathrm{MT}+\tau,3} = 0.
\end{aligned}
\tag{B.2}
$$

By defining the ratio of the binding rate constant and unbinding rate constant as affin-

ity (K_a), the probabilities can be obtained by solving the following equations.

$$\begin{aligned} P_{\mathrm{MT}+\tau,1} &= K_{a,1}[\mathrm{TUB}_1]P_\phi, \\ P_{\mathrm{MT}+\tau,2} &= K_{a,2}[\mathrm{TUB}_2]P_\phi, \\ P_{\mathrm{MT}+\tau,3} &= K_{a,3}[\mathrm{TUB}_3]P_\phi, \\ P_\phi + P_{\mathrm{MT}+\tau,1} + P_{\mathrm{MT}+\tau,2} + P_{\mathrm{MT}+\tau,3} &= 1. \end{aligned} \tag{B.3}$$

The following procedure is used to determine if a tau molecule binds to MTs and to determine the location of the binding; (1) $[\mathrm{TUB}_1]$ is the same as the concentration of tubulin dimers of the MTs. $[\mathrm{TUB}_2]$ and $[\mathrm{TUB}_3]$ are zeros. (2) P_ϕ and $P_{\mathrm{MT}+\tau,1-3}$ are calculated by using Eq. (B.3). (3) A random number ($r_{\tau,b}$) between 0 and 1 is generated. (4) If $r_{\tau,b}$ is less than P_ϕ, the tau molecule fails to bind to the MT. If $P_\phi \leq r_{\tau,b} < P_\phi + P_{\mathrm{MT}+\tau,1}$, the tau molecule is determined to bind to TUB_1. If $P_\phi + P_{\mathrm{MT}+\tau,1} \leq r_{\tau,b} < P_\phi + P_{\mathrm{MT}+\tau,1} + P_{\mathrm{MT}+\tau,2}$, the tau molecule is determined to bind to TUB_2. Otherwise, the tau binds to TUB_3. (5) When it is determined that the tau protein is bound to the MTs, another random number is generated to determine the binding location among the tubulins of the selected type. (6) The new values of $[\mathrm{TUB}_{1-3}]$ are calculated based on the binding of the tau protein. The calculations from (2) to (6) are repeated again for every tau molecule with different random numbers.

B.3 Parameters

The parameters ($K_{a,1-3}$, $N_{\max}$, and $P_{\mathrm{ub,cnt}}$) are obtained using the previous experiments [58, 69] regarding the binding of tau proteins on MTs and several effects of tau proteins on the binding rate of unbound kinesins, and the run length of kinesins.

Dixit et al. [58] used a very small concentration (50 nM) of dimer tubulins compared to their concentration in cells ($\simeq 20\ \mu\mathrm{M}$). The binding rate of tau proteins to MTs is low for

the small concentration of tubulins. To compensate this slowed reaction rate, they lowered the ionic strength in the assay. They reported that almost every tau in the assay binds to the MTs when m_τ is small. Thus, it is difficult to determine the value of $K_{a,1}$ precisely with their results. In the model, a large number (1,000 nM^{-1}) is used for $K_{a,1}$. Then, the number of bound of tau molecules and the binding rate of kinesins are calculated with this model for various $K_{a,2}$, $K_{a,3}$, and $N_{\max}$. The lower and upper bounds are as following;$10^{-3} \leq K_{a,2} \leq 1$ nM^{-1}, $10^{-1} \leq K_{a,3} \leq 100$ nM^{-1}, $5 \leq N_{\max} \leq 20$. When $K_{a,2} = 7 \times 10^{-3}$ nM^{-1}, $K_{a,3} \geq 2$ nM^{-1}, and $N_{\max} = 12$, the binding of tau and binding rate of unbound kinesins have similar values to the experimental results obtained by Dixit et al. [58].

The run length of kinesins in the presence of tau proteins [58] is used to obtain the value of the parameter regarding the unbinding probability ($P_{\mathrm{ub,cnt}}$). $P_{\mathrm{ub,cnt}}$ is the probability of the kinesin to unbind from the MT when the kinesin contacts the tau clusters. When m_τ is 0.2 and 2, the run length of kinesins is decreased to 87 and 17 $\%$ of the run length in the absence of tau proteins. When $P_{\mathrm{ub,cnt}} = 3.2$ nm/ms, the model predicts similar run lengths, as shown in Fig. B.2-(d).

The values of $K_{a,1-3}$ obtained from the results of Dixit et al. [58] can be different from the values in the cell because the used concentration of tubulins and ionic strength are different from those values of cells. Thus, the values of $K_{a,1-3}$ are obtained again by using the experimental data of Ackmann et al. [69] because the concentration of tubulins and ionic strength of their experiments are similar to cells. $K_{a,1} = 3$ $\mu\mathrm{M}^{-1}$, $K_{a,2} = 3 \times 10^{-3}$ $\mu\mathrm{M}^{-1}$, and $K_{a,3} \geq 10$ $\mu\mathrm{M}^{-1}$ give similar results to the experimental results, as shown in Fig. B.2-(a) and (b). If $K_{a,3} \geq 10$ $\mu\mathrm{M}^{-1}$, the effects of $K_{a,3}$ on the characteristics of tau clusters are negligible as shown in Fig. B.2-(c). Thus, $K_{a,3}$ of 10 $\mu\mathrm{M}^{-1}$ is used in chapter VII.

B.4 Effects of $[\tau]$ and N_{MT} on the motion of kinesin

The binding rate and unbinding rate of kinesins depend on $[\tau]$ and N_{MT} of the axon. When N_{MT} is large and $[\tau]$ is small, the kinesin can bind again to one of the MTs in a short time, as shown in Fig. B.3-(a). As $[\tau]$ increase, more tau clusters are developed on the MTs. Then, the unbinding occurs more frequently, as shown in Fig. B.3-(b). However, the kinesin in this axon can bind to one of MTs shortly because the axon has two MTs. If the axon has a single MT, the kinesins need more time to bind again to the MT, as shown in Fig. B.3-(c). Because this axon contains less tau proteins, the kinesin in this axon is less likely to unbind from the MT compared to the axon in Fig. B.3-(b). As a result, kinesins spend similar time on the MTs if the ratio of $[\tau]$ and N_{MT} is the same. This is the reason the transport velocity can be determined by m_τ.

B.5 Tubulins covered by bound cargoes

The kinesin of the unbound cargo are assumed not to bind some tubulins because of the interference between other bound cargoes and the unbound cargoes. The number of tubulins inaccessible to unbound kinesins (by a single bound cargo) depends on the size of the cargo. For the cargoes used in chapter VII ($r_c = 25$ nm), 105 tubulins are not available for the unbound kinesins, as shown in Fig. B.4.

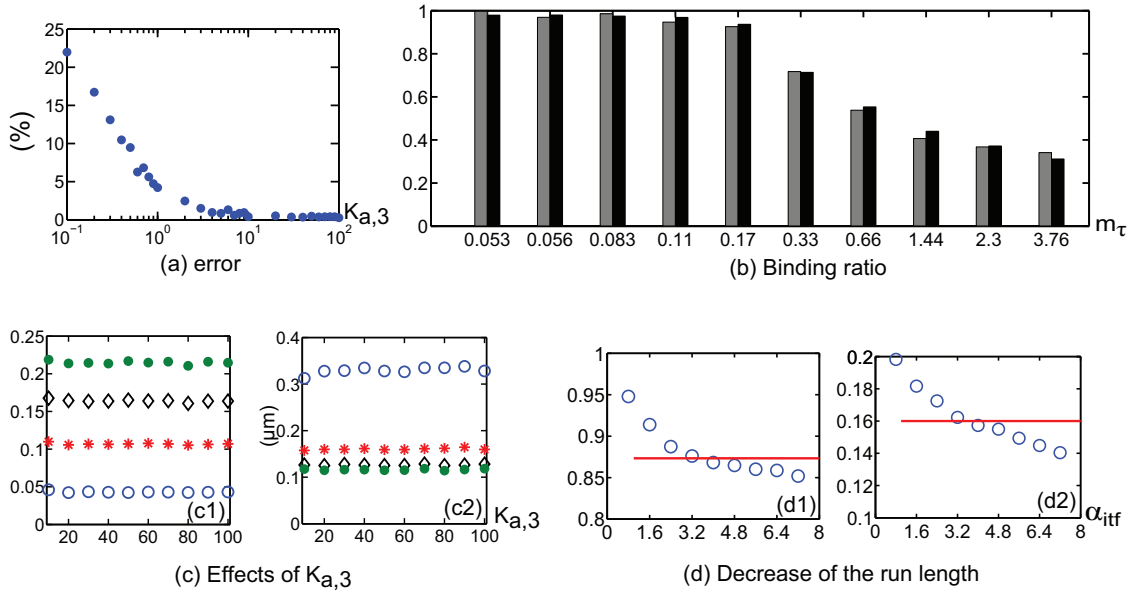

Figure B.2: Obtaining of the values of the parameters (a) depicts the sum of the errors (i.e., difference between the model and the experiments regarding the binding ratio of tau proteins (=bound tau proteins/(bound tau proteins+unbound tau proteins)) and the difference on binding rate of kinesins) over $K_{a,3}$. The values of $K_{a,1}$ and $K_{a,2}$ are fixed as 3 $\mu\mathrm{M}^{-1}$ and 3×10^{-3} $\mu\mathrm{M}^{-1}$. (b) shows the binding ratio of tau proteins over various m_τ for the obtained parameters. The gray bars denote the ratio measured from the experiment, and the black bars represent the ratio obtained from the model. (c1) shows the ratio of tubulins occupied by two or more tau proteins and all tubulins over $K_{a,3}$. The hollow circles, asterisks, diamonds, and filled circles denote the ratio of $m_\tau = 0.5$, 1, 1.5, and 2, respectively. (c2) is the average distance between tau clusters. (d) depicts the ratio of the run length in the presence of tau and the run length in the absence of tau proteins. The circle indicates the run length ratio obtained from the model. The line represents the experimentally observed ratio. (d1) depicts the ratio of the run length for $m_\tau = 0.2$ and the run length in the absence of tau proteins over $P_{\mathrm{ub,cnt}}$. (d2) shows the ratio for 2 $\mu\mathrm{M}$.

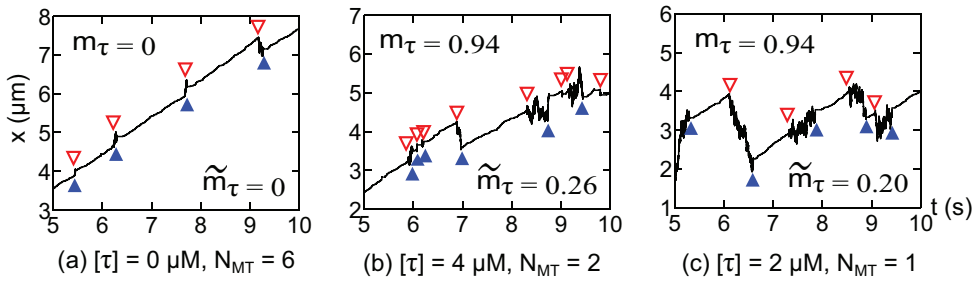

Figure B.3: Motion of the cargo. (a) depicts the transport of one cargo for $[\tau] = 0\ \mu\mathrm{M}$ and $N_{\mathrm{MT}} = 6$. (b) shows the transport for $[\tau] = 4\ \mu\mathrm{M}$ and $N_{\mathrm{MT}} = 1$. (c) depicts the transport for $[\tau] = 2\ \mu\mathrm{M}$ and $N_{\mathrm{MT}} = 1$. The hollow and filled triangles indicate the unbinding and binding, respectively. Note that m_τ of (b) and (c) are equal.

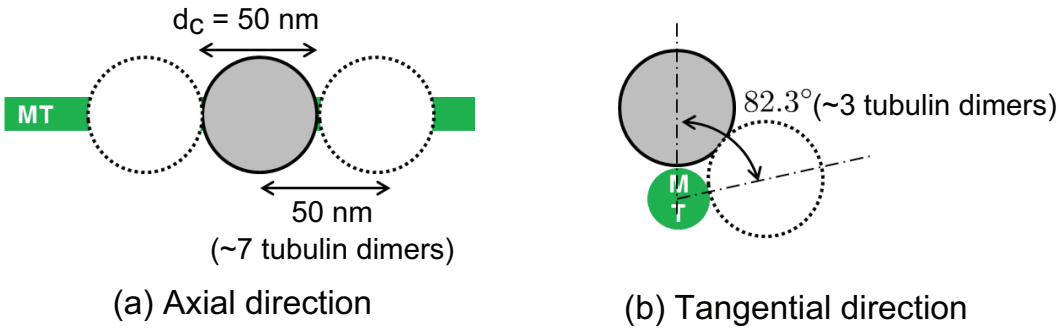

Figure B.4: Tubulins coverd by cargoes. (a) 7 tubulin dimers located in front of the bound cargo (depicted with the gray circle) are not available to the unbound kinesins. Likewise, 7 tubulin dimers behind the cargo are inaccessible to the unbound kinesins. (b) 3 tubulin dimers located right of the cargo and 3 tubulin dimers located left of the cargo are inaccessible to unbound kinesins. Thus, unbound kinesins cannot bind to these 105 ($= (7\times2+1)\times(3\times2+1)$) tubulins around the bound cargo.

BIBLIOGRAPHY

BIBLIOGRAPHY

[1] C.V. Sindelar and K.H. Downing. An atomic-level mechanism for activation of the kinesin molecular motors. *Proceedings of the National Academy of Sciences, USA*, 107(9):4111–4116, 2010.

[2] J. Beeg, S. Klumpp, R. Dimova, R.S. Gracia, E. Unger, and R. Lipowsky. Transport of beads by several kinesin motors. *Biophysical Journal*, 94(2):532–541, 2008.

[3] S. Camalet, F. Jülicher, and J. Prost. Self-organized beating and swimming of internally driven filaments. *Physical Review Letter*, 82(7):1590–1593, 1999.

[4] K. Grosh, J. Zheng, Y. Zou, E. Boer, and A.L. Nuttall. High-frequency electromotile responses in the cochlea. *Journal of the Acoustical Society of America*, 115:2178–2184, 2004.

[5] E. Mandelkow and E.M. Mandelkow. Kinesin motors and disease. *Trends Cell Biology*, 12(12):585–591, 2002.

[6] M. Schliwa and G. Woehlke. Molecular motors. *Nature*, 422(6933):759–765, 2003.

[7] A. Brown. Axonal transport of membranous and nonmembranous cargoes a unified perspective. *Journal of Cell Biology*, 160(6):817–821, 2003.

[8] N. Hirokawa, Y. Noda, Y. Tanaka, and S. Niwa. Kinesin superfamily motor proteins and intracellular transport. *Nature Reviews Molecular Cell Biology*, 10(10):682–696, 2009.

[9] N. Hirokawa and Y. Noda. Intracellular transport and kinesin superfamily proteins, kifs: structure, function, and dynamics. *Physiological Reviews*, 88(3):1089–1118, 2008.

[10] N. Hirokawa. Kinesin and dynein superfamily proteins and the mechanism of organelle transport. *Science*, 279(5350):519–526, 1998.

[11] M.L. Kutys, J. Fricks, and W.O. Hancock. Monte carlo analysis of neck linker extension in kinesin molecular motors. *PLoS Computational Biology*, 6(11):e1000980, 2010.

[12] C. Hyeon and J.N. Onuchic. Internal strain regulates the nucleotide binding site of the kinesin leading head. *Proceedings of the National Academy of Sciences, USA*, 104(7):2175–2180, 2007.

[13] H. Morii, T. Takenawa, F. Arisaka, and T. Shimizu. Identification of kinesin neck region as a stable α-helical coiled coil and its thermodynamic characterization. *Biochemistry*, 36(7):1933–1942, 1997.

[14] M. Thormählen, A. Marx, S. Sack, and E. Mandelkow. The coiled-coil helix in the neck of kinesin. *Journal of Structural Biology*, 122(1):30–41, 1998.

[15] A. Yildiz, M. Tomishige, R.D. Vale, and P.R. Selvin. Kinesin walks hand-over-hand. *Science*, 303(5658):676–678, 2004.

[16] C.L. Asbury, A.N. Fehr, and S.M. Block. Kinesin moves by an asymmetric hand-over-hand mechanism. *Science*, 302(5653):2130–2134, 2003.

[17] D.L. Coy, M. Wagenbach, and J. Howard. Kinesin takes one 8-nm step for each atp that it hydrolyzes. *Journal of Biological Chemistry*, 274(6):3667–3671, 1999.

[18] M. Nishiyama, E. Muto, Y. Inoue, T. Yanagida, and H. Higuchi. Substeps within the 8-nm step of the atpase cycle of single kinesin molecules. *Nature Cell Biology*, 3(4):425–428, 2001.

[19] H. Higuchi, E. Muto, Y. Inoue, and T. Yanagida. Kinetics of force generation by single kinesin molecules activated by laser photolysis of caged atp. *Proceedings of the National Academy of Sciences, USA*, 94(9):4395–4400, 1997.

[20] I. Crevel, N. Carter, M. Schliwa, and R. Cross. Coupled chemical and mechanical reaction steps in a processive neurospora kinesin. *EMBO Journal*, 18(21):5863–5872, 1999.

[21] C. Kural, H. Balci, and P.R. Selvin. Molecular motors one at a time: Fiona to the rescue. *Journal of Physics: Condensed Matter*, 17(47):S3979, 2005.

[22] M.J. Schnitzer and S.M. Block. Kinesin hydrolyses one atp per 8-nm step. *Nature*, 388(6640):386–390, 1997.

[23] S.P. Gilbert, M.L. Moyer, and K.A. Johnson. Alternating site mechanism of the kinesin atpase. *Biochemistry*, 37(3):792–799, 1998.

[24] S.M. Block, C.L. Asbury, J.W. Shaevitz, and M.J. Lang. Probing the kinesin reaction cycle with a 2d optical force clamp. *Proceedings of the National Academy of Sciences, USA*, 100(5):2351, 2003.

[25] M.J. Schnitzer, K. Visscher, and S.M. Block. Force production by single kinesin motors. *Nature Cell Biology*, 2(10):718–723, 2000.

[26] A.N. Fehr, B. Gutiérrez-Medina, C.L. Asbury, and S.M. Block. On the origin of kinesin limping. *Biophysical Journal*, 97(6):1663–1670, 2009.

[27] N.J. Carter and R.A. Cross. Mechanics of the kinesin step. *Nature*, 435(7040):308–312, 2005.

[28] K. Visscher, M.J. Schnitzer, and S.M. Block. Single kinesin molecules studied with a molecular force clamp. *Nature*, 400(6740):184–189, 1999.

[29] M. Nishiyama, H. Higuchi, and T. Yanagida. Chemomechanical coupling of the forward and backward steps of single kinesin molecules. *Nature Cell Biology*, 4(10):790–797, 2002.

[30] S.M. Block, L.S.B. Goldstein, and B.J. Schnapp. Bead movement by single kinesin molecules studied with optical tweezers. *Nature*, 348(22):348–352, 1990.

[31] R.F. Fox and M.H. Choi. Rectified brownian motion and kinesin motion along microtubules. *Physical Review E*, 63(5):051901, 2001.

[32] C.S. Peskin and G. Oster. Coordinated hydrolysis explains the mechanical behavior of kinesin. *Biophysical Journal*, 68(4):202S–211S, 1995.

[33] R.D. Astumian. Thermodynamics and kinetics of a brownian motor. *Science*, 276(5314):917–922, 1997.

[34] M. Bier. Brownian ratchets in physics and biology. *Contemporary Physics*, 38(6):371–379, 1997.

[35] F. julicher and J. Prost. Spontaneous oscillations of collective molecular motors. *Physical Review Letter*, 78(23):4510–4513, 1997.

[36] K.B. Zeldovich, J.F. Joanny, and J. Prost. Motor proteins transporting cargos. *European Physcial Journal E*, 17(2):155–163, 2005.

[37] M.E. Fisher and A.B. Kolomeisky. Simple mechanochemistry describes the dynamics of kinesin molecules. *Proceedings of the National Academy of Sciences, USA*, 98(14):7748–7753, 2001.

[38] R. Kanada and K. Sasaki. Theoretical model for motility and processivity of two-headed molecular motors. *Physical Review E*, 67(6):061917, 2003.

[39] E.B. Stukalin and A.B. Kolomeisky. Dynamic transitions in coupled motor proteins. *Physical Review E*, 73(3):031922, 2006.

[40] A.G. Hendricks, B.I. Epureanu, and E. Meyhöfer. Mechanistic mathematical model of kinesin under time and space fluctuating loads. *Nonlinear Dynamics*, 53(4):303–320, 2008.

[41] J Howard. *Mechanics of Motor Proteins and the Cytoskeleton.* Sinauer Associates, Sunderland, Massachusetts, 2001.

[42] S. Klumpp and R. Lipowsky. Cooperative cargo transport by several molecular motors. *Proceedings of the National Academy of Sciences, USA*, 102(48):17284–17289, 2005.

[43] C. Leduc, K. Padberg-Gehle, V. Varga, D. Helbing, S. Diez, and J. Howard. Molecular crowding creates traffic jams of kinesin motors on microtubules. *Proceedings of the National Academy of Sciences, USA*, 109(16):6100–6105, 2012.

[44] Y. Zhang. Microtubule length dependence of motor traffic in cells. *European Physical Journal E*, 35:101, 2012.

[45] T.L. Blasius, N. Reed, B.M. Slepchenko, and K.J. Verhey. Recycling of kinesin-1 motors by diffusion after transport. *PloS One*, 8(9):e76081, 2013.

[46] E.M. Mandelkow, K. Stamer, R. Vogel, E. Thies, and E. Mandelkow. Clogging of axons by tau, inhibition of axonal traffic and starvation of synapses. *Neurobiology of Aging*, 24(8):1079–1085, 2003.

[47] W. Stoothoff, P.B. Jones, T.L. Spires-Jones, D. Joyner, E. Chhabra, and et al. Differential effect of three-repeat and four-repeat tau on mitochondrial axonal transport. *Journal of Neurochemistry*, 111(2):417–427, 2009.

[48] A. Ebneth, R. Godemann, K. Stamer, S. Illenberger, B. Trinczek, E.M. Mandelkow, and E. Mandelkow. Overexpression of tau protein inhibits kinesin-dependent trafficking of vesicles, mitochondria, and endoplasmic reticulum: implications for alzheimer's disease. *Journal of Cell Biology*, 143(3):777–794, 1998.

[49] K. Stamer, R. Vogel, E. Thies, E. Mandelkow, and E.M. Mandelkow. Tau blocks traffic of organelles, neurofilaments, and app vesicles in neurons and enhances oxidative stress. *Journal of Cell Biology*, 156(6):1051–1063, 2002.

[50] B. Trinczek, A. Ebneth, E.M. Mandelkow, and E. Mandelkow. Tau regulates the attachment/detachment but not the speed of motors in microtubule-dependent transport of single vesicles and organelles. *Journal of Cell Science*, 112(14):2355–2367, 1999.

[51] A.G. Hendricks, B.I. Epureanu, and E. Meyhöfer. Collective dynamics of kinesin. *Physical Review E*, 79(3):031929, 2009.

[52] C. Kural, H. Kim, S. Syed, G. Goshima, V.I. Gelfand, and P.R. Selvin. Kinesin and dynein move a peroxisome in vivo: a tug-of-war or coordinated movement? *Science*, 308(5727):1469–1472, 2005.

[53] A. Ashkin, K. Schütze, J.M. Dziedzic, U. Euteneuer, and M. Schliwa. Force generation of organelle transport measured in vivo by an infrared laser trap. *Nature*, 1990.

[54] G.F. Reis, G. Yang, L. Szpankowski, C. Weaver, S.B. Shah, J.T. Robinson, T.S. Hays, G. Danuser, and L.S.B. Goldstein. Molecular motor function in axonal transport in vivo probed by genetic and computational analysis in drosophila. *Molecular Biology of the Cell*, 23(9):1700–1714, 2012.

[55] S. Verbrugge, S.M.J.L. Van den Wildenberg, and E.J.G. Peterman. Novel ways to determine kinesin-1's run length and randomness using fluorescence microscopy. *Biophysical Journal*, 97(8):2287–2294, 2009.

[56] R.D. Vale, T. Funatsu, D.W. Pierce, L. Romberg, Y. Harada, and T. Yanagida. Direct observation of single kinesin molecules moving along microtubules. *Nature*, 380(6573):451, 1996.

[57] T. Korten and S. Diez. Setting up roadblocks for kinesin-1: mechanism for the selective speed control of cargo carrying microtubules. *Lab on a Chip*, 8(9):1441–1447, 2008.

[58] R. Dixit, J.L. Ross, Y.E. Goldman, and E.L.F. Holzbaur. Differential regulation of dynein and kinesin motor proteins by tau. *Science*, 319(5866):1086–1089, 2008.

[59] I.A. Telley, P. Bieling, and T. Surrey. Obstacles on the microtubule reduce the processivity of kinesin-1 in a minimal in vitro system and in cell extract. *Biophysical Journal*, 96(8):3341–3353, 2009.

[60] K. Dreblow, N. Kalchishkova, and K.J. Böhm. Kinesin bypassing blockages on microtubule rails. *Biophysical Review Letter*, 4(01n02):139–151, 2009.

[61] A. Seitz and T. Surrey. Processive movement of single kinesins on crowded microtubules visualized using quantum dots. *EMBO J*, 25(2):267–277, 2006.

[62] W.R. Schief and J. Howard. Conformational changes during kinesin motility. *Current Opinion in Cell Biology*, 13(1):19–28, 2001.

[63] S. Rice, A.W. Lin, D. Safer, C.L. Hart, N. Naber, B.O. Carragher, S.M. Cain, E. Pechatnikova, E.M. Wilson-Kubalek, M. Whittaker, and et al. A structural change in the kinesin motor protein that drives motility. *Nature*, 402(6763):778–784, 1999.

[64] M. Tomishige, N. Stuurman, and R.D. Vale. Single-molecule observations of neck linker conformational changes in the kinesin motor protein. *Nature Structural & Molecular Biology*, 13(10):887–894, 2006.

[65] D. Cai, A.D. Hoppe, J.A. Swanson, and K.J. Verhey. Kinesin-1 structural organization and conformational changes revealed by fret stoichiometry in live cells. *The Journal of Cell Biology*, 176(1):51–63, 2007.

[66] V. Hariharan and W.O. Hancock. Insights into the mechanical properties of the kinesin neck linker domain from sequence analysis and molecular dynamics simulations. *Cellular and Molecular Bioengeering*, 2(2):177–189, 2009.

[67] T. Bornschlögl, G. Woehlke, and M. Rief. Single molecule mechanics of the kinesin neck. *Proceedings of the National Academy of Sciences, USA*, 106(17):6992–6997, 2009.

[68] A. Yildiz, M. Tomishige, A. Gennerich, and R.D. Vale. Intramolecular strain coordinates kinesin stepping behavior along microtubules. *Cell*, 134(6):1030–1041, 2008.

[69] M. Ackmann, H. Wiech, and E Mandelkow. Nonsaturable binding indicates clustering of tau on the microtubule surface in a paired helical filament-like conformation. *Journal of Biological Chemistry*, 275(39):30335–30343, 2000.

[70] A.B. Asenjo and H. Sosa. A mobile kinesin-head intermediate during the atp-waiting state. *Proceedings of the National Academy of Sciences, USA*, 106(14):5657–5662, 2009.

[71] N.R. Guydosh and S.M. Block. Direct observation of the binding state of the kinesin head to the microtubule. *Nature*, 461(7260):125–128, 2009.

[72] R. Holyst, A. Bielejewska, and J. Szymański et al. Scaling form of viscosity at all length-scales in poly (ethylene glycol) solutions studied by fluorescence correlation spectroscopy and capillary electrophoresis. *Physical Chemistry Chemical Physics*, 11(40):9025–9032, 2009.

[73] J. Szymanski, A. Patkowski, A. Wilk, P. Garstecki, and R. Holyst. Diffusion and viscosity in a crowded environment: from nano-to macroscale. *Journal of Physical Chemistry B*, 110(51):25593–25597, 2006.

[74] A. Gennerich and D. Schild. Finite-particle tracking reveals submicroscopic-size changes of mitochondria during transport in mitral cell dendrites. *Physical Biology*, 3:45, 2006.

[75] S.C. Kou, B.J. Cherayil, W. Min, P. Brian, and X.S. Xie. Single-molecule michaelis-menten equations. *Journal of Physical Chemistry B*, 109(41):19068–19081, 2005.

[76] S.P. Gilbert, M.R. Webb, M. Brune, and K.A. Johnson. Pathway of processive atp hydrolysis by kinesin. *Nature*, 373(6516):671, 1995.

[77] C.M. Coppin, J.T. Finer, J.A. Spudich, and R.D. Vale. Detection of sub-8-nm movements of kinesin by high-resolution optical-trap microscopy. *Proceedings of the National Academy of Sciences, USA*, 93(5):1913, 1996.

[78] G. Holzwarth, K. Bonin, and D.B. Hill. Forces required of kinesin during processive transport through cytoplasm. *Biophys Journal*, 82(4):1784–1790, 2002.

[79] J. Gagliano, M. Walb, B. Blaker, J.C. Macosko, and G. Holzwarth. Kinesin velocity increases with the number of motors pulling against viscoelastic drag. *European Biophysical Journal*, 39(5):801–813, 2010.

[80] D.B. Hill, M.J. Plaza, K. Bonin, and G. Holzwarth. Fast vesicle transport in pc12 neurites: velocities and forces. *European Biophysical Journal*, 33(7):623–632, 2004.

[81] Y. Shtridelman, G.M. Holzwarth, and C.T. Bauer et al. In vivo multimotor force-velocity curves by tracking and sizing sub-diffraction limited vesicles. *Cellular and Molecular Bioengeering*, 2(2):190–199, 2009.

[82] M.T. Arigo and G.H. McKinley. The effects of viscoelasticity on the transient motion of a sphere in a shear-thinning fluid. *Journal of Rheology*, 41:103–128, 1997.

[83] H. Frohlich and R. Sack. Theory of the rheological properties of dispersions. *Proceedings of the Royal Society of London. Series A. Mathematical and Physical Sciences*, 185(1003):415–430, 1946.

[84] M.J. King and N.D. Waters. The unsteady motion of a sphere in an elastico-viscous liquid. *Journal of Physics D: Applied Physics*, 5:141–150, 1972.

[85] J.G. Oldroyd. On the formulation of rheological equations of state. *Proceedings of the Royal Society of London. Series A. Mathematical and Physical Sciences*, 200(1063):523–541, 1950.

[86] R.H. Thomas and K. Walters. The unsteady motion of a sphere in an elastico-viscous liquid. *Rheology Acta*, 5(1):23–27, 1966.

[87] S.C. Kou and X.S. Xie. Generalized langevin equation with fractional gaussian noise: subdiffusion within a single protein molecule. *Physical Review Letter*, 93(18):180603, 2004.

[88] S.C. Lim and S.V. Muniandy. Self-similar gaussian processes for modeling anomalous diffusion. *Physical Review E*, 66(2):021114, 2002.

[89] T.G. Mason, K. Ganesan, J.H. Van Zanten, D. Wirtz, and S.C. Kuo. Particle tracking microrheology of complex fluids. *Physical Review Letter*, 79(17):3282–3285, 1997.

[90] H. Qian. *Fractional Brownian Motion and Fractional Gaussian Noise*. Springer, 2003.

[91] R. Zwanzig. *Nonequilibrium Statistical Mechanics*. Oxford University Press, USA, 2001.

[92] S. Yamada, D. Wirtz, and S.C. Kuo. Mechanics of living cells measured by laser tracking microrheology. *Biophysical Journal*, 78(4):1736–1747, 2000.

[93] T.A. Waigh. Microrheology of complex fluids. *Reports on Progress in Physics*, 685-742:685–, 2005.

[94] T.G. Mason. Estimating the viscoelastic moduli of complex fluids using the generalized stokes–einstein equation. *Rheologica Acta*, 39(4):371–378, 2000.

[95] T.G. Mason and D.A. Weitz. Optical measurements of frequency-dependent linear viscoelastic moduli of complex fluids. *Physical Review Letter*, 74(7):1250–1253, 1995.

[96] L. Starrs and P. Bartlett. One-and two-point micro-rheology of viscoelastic media. *Journal of Physics: Condensed Matter*, 15:S251, 2003.

[97] Y. Shtridelman, T. Cahyuti, B. Townsend, D. DeWitt, and J.C. Macosko. Force-velocity curves of motor proteins cooperating in vivo. *Cell Biochemistry and Biophysics*, 52(1):19–29, 2008.

[98] H. Tauchi and T. Sato. Age changes in size and number of mitochondria of human hepatic cells. *Journal of Gerontology*, 23(4):454–461, 1968.

[99] K.S. Thorn, J.A. Ubersax, and R.D. Vale. Engineering the processive run length of the kinesin motor. *Journal of Cell Biology*, 151(5):1093–1100, 2000.

[100] L.S.B. Goldstein. Kinesin molecular motors: transport pathways, receptors, and human disease. *Proceedings of the National Academy of Sciences, USA*, 98(13):6999, 2001.

[101] C. Kaether, P. Skehel, and C.G. Dotti. Axonal membrane proteins are transported in distinct carriers: a two-color video microscopy study in cultured hippocampal neurons. *Molecular Biology of the Cell*, 11(4):1213–1224, 2000.

[102] D. Wirtz. Particle-tracking microrheology of living cells: principles and applications. *Annual Review of Biophysics*, 38:301–326, 2009.

[103] S. Uemura, K. Kawaguchi, J. Yajima, M. Edamatsu, Y.Y. Toyoshima, and S. Ishiwata. Kinesin–microtubule binding depends on both nucleotide state and loading direction. *Proceedings of the National Academy of Sciences, USA*, 99(9):5977–5981, 2002.

[104] S. Uemura and S. Ishiwata et al. Loading direction regulates the affinity of adp for kinesin. *Nature Structural and Molecular Biology*, 10(4):308–311, 2003.

[105] W. Nam and B.I. Epureanu. Metrics for characterizing collective transport by multiple dimeric kinesins. *Physical Review E*, 86(5):051916, 2012.

[106] Wang Z and M. Li. Force-velocity relations for multiple-molecular-motor transport. *Physical Review E*, 80(4):041923, 2009.

[107] C. Gergely, J.C. Voegel, P. Schaaf, B. Senger, M. Maaloum, J.K.H. Hörber, and J. Hemmerle. Unbinding process of adsorbed proteins under external stress studied by atomic force microscopy spectroscopy. *Proceedings of the National Academy of Sciences, USA*, 97(20):10802–10807, 2000.

[108] C. Leduc, O. Campàs, K.B. Zeldovich, A. Roux, P. Jolimaitre, L. Bourel-Bonnet, B. Goud, J.F. Joanny, P. Bassereau, and J. Prost. Cooperative extraction of membrane nanotubes by molecular motors. *Proceedings of the National Academy of Sciences, USA*, 101(49):17096–17101, 2004.

[109] O. Campàs, C. Leduc, P. Bassereau, J. Casademunt, J.F. Joanny, and J. Prost. Coordination of kinesin motors pulling on fluid membranes. *Biophysical Journal*, 94(12):5009–5017, 2008.

[110] X. Yao and Y. Zheng. A stochastic model for kinesin bidirectional stepping. *Journal of Chemical Physics*, 140(8):084102, 2014.

[111] K. Svoboda and S.M. Block. Force and velocity measured for single kinesin molecules. *Cell*, 77(5):773–784, 1994.

[112] M.T. Valentine, P.M. Fordyce, T.C. Krzysiak, S.P. Gilbert, and S.M. Block. Individual dimers of the mitotic kinesin motor eg5 step processively and support substantial loads in vitro. *Nature Cell Biology*, 8(5):470–476, 2006.

[113] I. Dujovne, M. van den Heuvel, Y. Shen, M. de Graaff, and C. Dekker. Velocity modulation of microtubules in electric fields. *Nano Letters*, 8(12):4217–4220, 2008.

[114] J. Chen, Y. Kanai, N.J. Cowan, and N. Hirokawa. Projection domains of map2 and tau determine spacings between microtubules in dendrites and axons. *Nature*, 360(6405):674–677, 1992.

[115] S. Gunawardena and L.S.B. Goldstein. Cargo-carrying motor vehicles on the neuronal highway: Transport pathways and neurodegenerative disease. *Journal of Neurobiology*, 58(2):258–271, 2004.

[116] S.P. Gross, M. Tuma, S.W. Deacon, A.S. Serpinskaya, A.R. Reilein, and V.I. Gelfand. Interactions and regulation of molecular motors in xenopus melanophores. *Journal of Cell Biology*, 156(5):855, 2002.

[117] G.T. Shubeita, S.L. Tran, J. Xu, M. Vershinin, S. Cermelli, S.L. Cotton, M.A. Welte, and S.P. Gross. Consequences of motor copy number on the intracellular transport of kinesin-1-driven lipid droplets. *Cell*, 135(6):1098–1107, 2008.

[118] V. Levi, A.S. Serpinskaya, E. Gratton, and V. Gelfand. Organelle transport along microtubules in xenopus melanophores: evidence for cooperation between multiple motors. *Biophysical Journal*, 90(1):318–327, 2006.

[119] S. Leibler and D.A. Huse. Porters versus rowers: a unified stochastic model of motor proteins. *Journal of Cell Biology*, 121(6):1357–1368, 1993.

[120] F. Jülicher, A. Ajdari, and J. Prost. Modeling molecular motors. *Reviews of Modern Physics*, 69(4):1269–1281, 1997.

[121] F. Berger, C. Keller, S. Klumpp, and R. Lipowsky. Distinct transport regimes for two elastically coupled molecular motors. *Physical Review Letters*, 108(20):208101, 2012.

[122] S. Bouzat and F. Falo. The influence of direct motor–motor interaction in models for cargo transport by a single team of motors. *Physical Biology*, 7:046009, 2010.

[123] Y. Zhang. Cargo transport by several motors. *Physical Review E*, 83(1):011909, 2011.

[124] J.G. Orlandi, C. Blanch-Mercader, J. Brugués, and J. Casademunt. Cooperativity of self-organized brownian motors pulling on soft cargoes. *Physical Review E*, 82(6):061903, 2010.

[125] A.G. Hendricks, B.I. Epureanu, and E. Meyhöfer. Cooperativity of multiple kinesin-1 motors mechanically coupled through a shared load. *Physica D*, 238(6):677–686, 2009.

[126] P.J. Atzberger and C.S. Peskin. A Brownian dynamics model of kinesin in three dimensions incorporating the force-extension profile of the coiled-coil cargo tether. *Bulletin of Mathematical Biology*, 68(1):131–160, 2006.

[127] L. Romberg and R.D. Vale et al. Chemomechanical cycle of kinesin differs from that of myosin. *Nature*, 361(6408):168–170, 1993.

[128] E. Mandelkow and K.A. Johnson. The structural and mechanochemical cycle of kinesin. *Trends Biochemical Sciences*, 23(11):429–433, 1998.

[129] R.A. Cross, I. Crevel, N.J. Carter, M.C. Alonso, K. Hirose, and L.A. Amos. The conformational cycle of kinesin. *Philosophical Transactions Royal Society B*, 355(1396):459–464, 2000.

[130] W.O. Hancock and J. Howard. Kinesins processivity results from mechanical and chemical coordination between the atp hydrolysis cycles of the two motor domains. *Proceedings of the National Academy of Sciences, USA*, 96(23):13147–13152, 1999.

[131] D.D. Hackney. Evidence for alternating head catalysis by kinesin during microtubule-stimulated atp hydrolysis. *Proceedings of the National Academy of Sciences, USA*, 91(15):6865–6869, 1994.

[132] K. Svoboda, P.P. Mitra, and S.M. Block. Fluctuation analysis of motor protein movement and single enzyme kinetics. *Proceedings of the National Academy of Sciences, USA*, 91(25):11782–11786, 1994.

[133] Y. Taniguchi, M. Nishiyama, Y. Ishii, and T. Yanagida. Entropy rectifies the brownian steps of kinesin. *Nature Chemical Biology*, 1(6):342–347, 2005.

[134] A.B. Kolomeisky, E.B. Stukalin, and A.A. Popov. Understanding mechanochemical coupling in kinesins using first-passage-time processes. *Physical Review E*, 71(3):031902, 2005.

[135] R.D. Astumian and M. Bier. Fluctuation driven ratchets: molecular motors. *Physical Review Letter*, 72(11):1766, 1994.

[136] M. Bier and F.J. Cao. How occasional backstepping can speed up a processive motor protein. *Biosystems*, 103(3):355–359, 2011.

[137] W. Nam and B.I. Epureanu. The effects of viscoelastic fluid on kinesin transport. *Journal of Physics: Condensed Matter*, 24(37):375103, 2012.

[138] K. Dreblow, N. Kalchishkova, and K.J. Böhm. Kinesin passing permanent blockages along its protofilament track. *Biochemical Biophysical Research Communications*, 395(4):490–495, 2010.

[139] J.F. Marko and E.D. Siggia. Stretching dna. *Macromolecules*, 28(26):8759–8770, 1995.

[140] A. Zhang and D. Thirumalai. Dissecting the kinematics of the kinesin step. *Structure*, 20(4):628–640, 2012.

[141] F.J. Kull, E.P. Sablin, R. Lau, R.J. Fletterick, and R.D. Vale. Crystal structure of the kinesin motor domain reveals a structural similarity to myosin. *Nature*, 380(6574):550, 1996.

[142] E. Swanson, D.C. Teller, and C. Haen. The low reynolds number translational friction of ellipsoids, cylinders, dumbbells, and hollow spherical caps. numerical testing of the validity of the modified oseen tensor in computing the friction of objects modeled as beads on a shell. *Journal of Chemical Physics*, 68(11):5097–5102, 1978.

[143] W. Hwang, M.J. Lang, and M. Karplus. Force generation in kinesin hinges on cover-neck bundle formation. *Structure*, 16(1):62–71, 2008.

[144] J.M. Mason and K.M. Arndt. Coiled coil domains: stability, specificity, and biological implications. *ChemBioChem*, 5(2):170–176, 2004.

[145] F. Kozielski, S. Sack, A. Marx, M. Thormählen, E. Schönbrunn, V. Biou, A. Thompson, E.M. Mandelkow, and E. Mandelkow. The crystal structure of dimeric kinesin and implications for microtubule-dependent motility. *Cell*, 91(7):985–994, 1997.

[146] L. Murmanis. Particles and microtubules in vascular cells of pinus strobus l. during cell wall formation. *New phytologist*, 70(6):1089–1093, 1971.

[147] C. Davis and K. Gull. Protofilament number in microtubules in cells of two parasitic nematodes. *Journal of Parasitology*, pages 1094–1099, 1983.

[148] A. Seitz, H. Kojima, K. Oiwa, E.M. Mandelkow, Y.H. Song, and E. Mandelkow. Single-molecule investigation of the interference between kinesin, tau and map2c. *EMBO J*, 21(18):4896–4905, 2002.

[149] D.P. McVicker, L.R. Chrin, and C.L. Berger. The nucleotide-binding state of microtubules modulates kinesin processivity and the ability of tau to inhibit kinesin-mediated transport. *Journal of Biological Chemistry*, 286(50):42873–42880, 2011.

[150] M. Vershinin, B.C. Carter, D.S. Razafsky, S.J. King, and S.P. Gross. Multiple-motor based transport and its regulation by tau. *Proceedings of the National Academy of Sciences, USA*, 104(1):87–92, 2007.

[151] L.A. Amos. Microtubule structure and its stabilisation. *Organic & Biomolecular Chemistry*, 2(15):2153–2160, 2004.

[152] S. Kar, J. Fan, M.J. Smith, M. Goedert, and L.A. Amos. Repeat motifs of tau bind to the insides of microtubules in the absence of taxol. *The EMBO journal*, 22(1):70–77, 2003.

[153] J. Xu, S.J. King, M. Lapierre-Landry, and B. Nemec. Interplay between velocity and travel distance of kinesin-based transport in the presence of tau. *Biophysical Journal*, 105(10):L23–L25, 2013.

[154] J. Kerssemakers, J. Howard, H. Hess, and S. Diez. The distance that kinesin-1 holds its cargo from the microtubule surface measured by fluorescence interference contrast microscopy. *Proceedings of the National Academy of Sciences*, 103(43):15812–15817, 2006.

[155] G.S. Bloom, M.C. Wagner, K.K. Pfister, and S.T. Brady. Native structure and physical properties of bovine brain kinesin and identification of the atp-binding subunit polypeptide. *Biochemistry*, 27(9):3409–3416, 1988.

[156] N. Hirokawa, Y. Shiomura, and S. Okabe. Tau proteins: the molecular structure and mode of binding on microtubules. *The Journal of cell biology*, 107(4):1449–1459, 1988.

[157] A. Peck, M.E. Sargin, N.E. LaPointe, K. Rose, and et al. Tau isoform-specific modulation of kinesin-driven microtubule gliding rates and trajectories as determined with tau-stabilized microtubules. *Cytoskeleton*, 68(1):44–55, 2011.

[158] B.L. Goode, M. Chau, P.E. Denis, and S.C. Feinstein. Structural and functional differences between 3-repeat and 4-repeat tau isoforms implications for normal tau function and the onset of neurodegenerative disease. *Journal of Biological Chemistry*, 275(49):38182–38189, 2000.

[159] E.M. Mandelkow, J. Biernat, G. Drewes, N. Gustke, B. Trinczek, and E. Mandelkow. Tau domains, phosphorylation, and interactions with microtubules. *Neurobiology of Aging*, 16(3):355–362, 1995.

[160] U. Preuss, J. Biernat, E.M. Mandelkow, and E. Mandelkow. The jaws model of tau-microtubule interaction examined in cho cells. *Journal of Cell Science*, 110(6):789–800, 1997.

[161] R.A. Santarella, G. Skiniotis, K.N. Goldie, P. Tittmann, , and et al. Surface-decoration of microtubules by human tau. *Journal of Molecular Biology*, 339(3):539–553, 2004.

[162] S. Konzack, E. Thies, A. Marx, E.M. Mandelkow, and E. Mandelkow. Swimming against the tide: mobility of the microtubule-associated protein tau in neurons. *Journal of Neuroscience*, 27(37):9916–9927, 2007.

[163] P. Friedhoff, M. Von Bergen, E.M. Mandelkow, P. Davies, and E. Mandelkow. A nucleated assembly mechanism of alzheimer paired helical filaments. *Proceedings of the National Academy of Sciences*, 95(26):15712–15717, 1998.

[164] K. Luby-Phelps. Cytoarchitecture and physical properties of cytoplasm: volume, viscosity, diffusion, intracellular surface area. *International Review of Cytology*, 192:189–221, 1999.

[165] S. Popov and M.M. Poo. Diffusional transport of macromolecules in developing nerve processes. *Journal of Neuroscience*, 12(1):77–85, 1992.

[166] D. Barazanyl, P.J. Basser, and Y. Assaf. In vivo measurement of axon diameter distribution in the corpus callosum of rat brain. *Brain*, 132(5):1210–1220, 2009.

[167] A.D. Cash, G. Aliev, S.L. Siedlak, A. Nunomura, H. Fujiokai, X. Zhu, and A.K. Raina et al. Microtubule reduction in alzheimer's disease and aging is independent of τ filament formation. *The American journal of pathology*, 162(5):1623–1627, 2003.

[168] C.T. Nguyen, F. Desgranges, G. Roy, N. Galanis, T. Mare, S. Boucher, and H. Angue Mintsa. Temperature and particle-size dependent viscosity data for water-based nanofluids–hysteresis phenomenon. *International Journal of Heat and Fluid Flow*, 28(6):1492–1506, 2007.

[169] I.M.T.C. Crevel, A. Lockhart, and R.A. Cross. Weak and strong states of kinesin and ncd. *Journal of Molecular Biology*, 257(1):66–76, 1996.